Embedded analytical-numerical simulation of fault reactivation in heterogeneous subsurface formations

Inspired by the issue of induced seismicity in the Groningen field

Shokrollahzadeh Behbahani, S.

DOI
10.4233/uuid:61b51947-e93a-46d2-bffe-2fa2f929329d

Publication date
2024

Document Version
Final published version

Citation (APA)
Shokrollahzadeh Behbahani, S. (2024). *Embedded analytical-numerical simulation of fault reactivation in heterogeneous subsurface formations: Inspired by the issue of induced seismicity in the Groningen field*. [Dissertation (TU Delft), Delft University of Technology]. https://doi.org/10.4233/uuid:61b51947-e93a-46d2-bffe-2fa2f929329d

Embedded Analytical-Numerical Simulation of Fault Reactivation in Heterogeneous Subsurface Formations

Inspired by the issue of induced seismicity in the Groningen field

EMBEDDED ANALYTICAL-NUMERICAL SIMULATION OF FAULT REACTIVATION IN HETEROGENEOUS SUBSURFACE FORMATIONS

INSPIRED BY THE ISSUE OF INDUCED SEISMICITY IN THE GRONINGEN FIELD

Dissertation

for the purpose of obtaining the degree of doctor
at Delft University of Technology
by the authority of the Rector Magnificus, prof. dr. ir. T.H.J.J. van der Hagen,
chair of the Board for Doctorates
to be defended publicly on
Wednesday 19 June 2024 at 17:30 o'clock

by

Sara SHOKROLLAHZADEH BEHBAHANI

Master of Science in Petroleum Engineering - Hydrocarbon Reservoirs,
Amirkabir University of Technology, Iran.
born in Ahvaz, Iran

This dissertation has been approved by the promotors.

Composition of the doctoral committee:

Rector Magnificus,	chairperson
Prof. dr. H. Hajibeygi,	Delft University of Technology, promotor
Prof. dr. ir. J. D. Jansen,	Delft University of Technology, promotor
Dr. D. V. Voskov,	Delft University of Technology, copromotor

Independent members:

Prof.dr.ir. L.J. Sluys,	Delft University of Technology
Prof.dr.ir. C. Vuik,	Delft University of Technology
Dr. A.G. Muntendam-Bos,	Delft University of Technology
Prof. dr. P. Jenny,	ETH Zurich, Switzerland

Reserve member:

Prof.dr.ir. C.P.A. Wapenaar,	Delft University of Technology

Keywords: Induced seismicity, Fault reactivation, Poroelastic media, Embedded-Numerical, semi-analytical, hybrid simulation.

Printed by: Gildeprint

Cover by: Sara Shokrollahzadeh Behbahani

ISBN 000-00-0000-000-0

An electronic copy of this dissertation is available at
https://repository.tudelft.nl/.

CONTENTS

List of Figures

List of Tables

SUMMARY

Induced seismicity refers to seismic events (earthquakes) triggered by human activities. Such events, even when characterized by relatively modest magnitudes, have the potential to jeopardize the safety of individuals, the surrounding environment, and infrastructure.

Production from hydrocarbon reservoirs can alter the in-situ stress state, leading to induced seismicity. This is reported in the Groningen field, where substantial gas production caused fault reactivation and subsequent earthquakes. Understanding events in the deep subsurface is crucial to proactively mitigate future seismic occurrences.

To understand the causes of induced seismicity, the underlying physics are examined and defined in terms of relevant governing equations and models. This reveals the interconnected nature of fluid depletion, rock deformation, and fault slip. The goal of this study is to develop simulation techniques to solve these equations.

Towards this end, firstly, a finite volume embedded-numerical simulation method, called the Smoothed Enhanced Finite Volume method (sEFVM), is developed. This method is revealed to be computationally efficient for reservoir-scale modeling of heavily faulted systems and performed well in comparison to known solutions and other simulators.

However, in settings where analytical solutions indicated noncontinuous shear stress profiles, sEFVM accuracy suffers. Recognizing this limitation, a semi-analytical approach is developed, extending analytical expressions to be solved over the sEFVM mesh. This extension allows for more accurate solutions, accommodating complex reservoir and fault geometries. The semi-analytical method is successfully used to estimate the onset of fault nucleation and the magnitude of the seismic moment resulting from depletion.

The semi-analytical approach is limited to simulating fault slip up to the point of nucleation. To overcome this constraint, a hybrid method is developed. With appropriate assumptions regarding the post-nucleation state and the use of sEFVM to numerically calculate post-nucleation stresses, the hybrid method can effectively model multi-fault systems in the seismic stage assuming quasi-static behavior.

In summary, this research contributes by presenting novel computational frameworks for studying fault reactivation in faulted poroelastic media, offering insights into the complex interactions of the physics at play. The proposed embedded-numerical, semi-analytical, and hybrid methods pave the way for further advancements in the field.

SAMENVATTING

Geïnduceerde seismiciteit verwijst naar seismische gebeurtenissen (aardbevingen) veroorzaakt door menselijke activiteiten. Dergelijke gebeurtenissen, zelfs wanneer gekenmerkt door relatief bescheiden magnitudes, hebben het potentieel om de veiligheid van individuen, de omgeving en infrastructuur in gevaar te brengen.

Productie uit koolwaterstofreservoirs kan de in-situ spanningstoestand veranderen, resulterend in geïnduceerde seismiciteit. Dit wordt gemeld in het Groningen-veld, waar aanzienlijke gasproductie breukreactivatie en daaropvolgende aardbevingen veroorzaakte. Het begrijpen van gebeurtenissen in de diepe ondergrond is cruciaal om toekomstige seismische gebeurtenissen proactief te beheersen.

Om de oorzaken van geïnduceerde seismiciteit te begrijpen, wordt de onderliggende natuurkunde onderzocht en gedefinieerd in termen van relevante vergelijkingen en modellen. Dit onthult de onderling verbonden aard van gasproduktie, deformatie van gesteente en breukverschuiving. Het doel van deze studie is het ontwikkelen van simulatietechnieken om deze vergelijkingen op te lossen.

Om dit te bereiken, wordt allereerst een numerieke simulatiemethode met ingebedde eindige volumes ontwikkeld, genaamd de Smoothed Enhanced Finite Volume-methode (sEFVM). Deze methode blijkt rekenkundig efficiënt te zijn voor het modelleren van reservoirs op grote schaal met veel breuken en presteerde goed in vergelijking met bekende oplossingen en andere simulatoren.

Echter, in situaties waar analytische oplossingen niet-continue schuifspanningsprofielen aangaven, lijdt de nauwkeurigheid van sEFVM. Daarom wordt een semi-analytische benadering ontwikkeld, waarbij analytische uitdrukkingen worden uitgebreid om te worden opgelost over het sEFVM-rooster. Deze uitbreiding maakt nauwkeuriger oplossingen mogelijk, aangepast aan complexe geometrieën van reservoirs en breuken. De semi-analytische methode wordt met succes gebruikt om het begin van breuknucleatie en de omvang van het seismische moment als gevolg van gasproduktie te schatten.

De semi-analytische benadering is beperkt tot het simuleren van breukverschuiving tot het punt van nucleatie. Om deze beperking te overwinnen, wordt een hybride methode ontwikkeld. Met geschikte aannames over de postnucleatie-toestand en het gebruik van sEFVM om postnucleatie-spanningen numeriek te berekenen, kan de hybride methode effectief meerfoutssystemen modelleren in het seismische stadium, onder aanname van quasi-statische condities.

Samengevat draagt dit onderzoek bij door nieuwe rekenkundige kaders te presenteren voor het bestuderen van breukreactivatie in verbreukte poro-elastische media, en biedt inzichten in de complexe interacties van de natuurkunde die in het spel zijn. De voorgestelde ingebedde numerieke, semi-analytische en hybride methoden banen de weg voor verdere vooruitgang op dit gebied.

PREFACE

Thank you to the people who made it possible:

I thank my supervisors Hadi, Denis and Jan Dirk, who changed my logical thinking, scientific writing and self presentation for the better. My admiration for their professionalism and scientific discipline served as a role model to me for improvement. They were generous with their patience and encouragement in my weaker moments and inspirational and supportive all throughout.

I thank my parents and sisters without whom I'd not have been able to do this. Literally, their support, mentally and physically, is what made this milestone possible.

Last but not least Elia, my son who was born within months of my PhD. Since I learnt that he was to enter my world, I was doubly inspired to strive for the better, every second of every minute of every day. Many times, I felt I didn't have it in me. Then there he was, and instantly I could swim oceans and move mountains. He gave me insights to who I am, where I lack and where I'm plenty, my limits and my strengths. I took care of him to grow, but he has been the reason for my growth.

Sara Shokrollahzadeh Behbahani
Delft, December 2023

1

INTRODUCTION

Induced seismicity can result in significant detrimental consequences. In the Groningen field, despite production cutbacks since 2013, the problem of induced seismicity has persisted and is expected to continue well past the full-field shutdown. This signifies the importance of scientific research to understand the causal mechanisms behind induced earthquakes. Simulation techniques in the field of geomechanics are a focal point of research with a relevant application in the study of induced seismicity.

This chapter draws attention to the importance of induced seismicity and provides relevant background information regarding the Groningen field. This is followed by a literature review on numerical, analytical, and semi-analytical methods that have been used in the field of computational geomechanics. A summary of the scope and limitations of the methods highlights the contribution of the current study. The chapter concludes by offering a roadmap to the content covered in the following chapters.

1.1. INDUCED SEISMICITY AND ITS IMPACT

Induced seismic events are earthquakes caused by human activity that alter subsurface stresses. Prior to any human intervention, faults are subject to an initial stress state resulting from the depositional environment of the reservoir and tectonic movements in the earth's crust. After fluid production or injection, stress will alter due to changes in reservoir pore pressure. This change in stress can potentially cause a re-activation of faults. This would result in the movement of the fault, in the tangential direction along the fault plane. The measure of this movement (also known as the slip) is important in the study of induced seismicity as it can be used to estimate when an earthquake is expected, and what magnitude it may have.

The concept behind induced seismicity is well established. It has been shown that hydrocarbon gas production correlates with induced tremors, especially in depleting gas fields. The Groningen field in the Netherlands is a well known example for induced seismicity [1].

The induced tremors in the Groningen field have remained small on the Richter scale, but they pose risks that prevent further utilization of subsurface capacity for

energy and climate relevant projects. These events carry significant detrimental consequences. Induced earthquakes are a subject of increasing concern due to their potential adverse impacts on both human societies and the environment. They have been linked to structural damages in buildings, bridges, and other critical infrastructure. The ground shaking and vibrations can compromise the integrity of structures, leading to safety hazards and economic losses. This can pose immediate threats to public safety. The unpredictability of induced earthquakes can catch communities off guard, potentially causing panic and injury [2]. Prolonged exposure to low-level seismicity has been associated with psychological stress and anxiety among residents living in affected regions [3]. Induced seismicity can disrupt economic activities in the affected regions. Property devaluation, decreased tourism, and increased insurance costs are potential consequences that can strain local economies and livelihoods [4]. The perception of risk can erode public trust in industries that trigger such events. Public skepticism and concerns about the transparency of operations can hinder the social license to operate for industries involved in activities linked to seismicity [5]. The negative impacts of induced seismicity have prompted debates about regulatory measures and legal frameworks [6].

Gas production from the Groningen field has been throttled back since 2013 and will come to a full shut-down by mid-2024 to curtail future events [7]. But field shut-down does not necessarily guarantee the immediate prevention of future seismic events. In fact, the underground stress stabilization occurs through a slow time-dependent process of pressure equilibration, during which fault activation (perhaps with lower magnitudes) can potentially take place. For the case of the Groningen, they are expected to continue, but gradually diminish. This prediction is shown in Figure 1.1 [8]. This figure also shows that induced seismic events will continue to remain an important topic in the coming decades. This situation emphasises a need to look beyond field shut-down and to develop robust strategies to minimize future risks.

1.2. THE GRONINGEN FIELD SEISMICITY: FROM DISCOVERY TO SHUT DOWN

The Groningen field was discovered in 1959. Interestingly, its enormous gas reserve was recognized a year later in 1960 with an initial estimate of 60 billion cubic meters (bcm). This appraisal underwent several revisions over time. By early 1962, the estimated gas reserve was adjusted to 150 bcm, which further increased to 470 bcm by the end of that year. Subsequent re-evaluations were made, with the estimate reaching 1100 bcm in 1963, 1900 bcm in 1967, 2409 bcm in 1987, and finally 2750 bcm in 1993. The more recent calculation is approximating 2900 bcm of initial gas in place[9].

The Groningen gas field is one of the largest natural gas fields in Europe and one of the most important in the world. Gas from the Groningen field has played a crucial role in the Dutch and European energy mix, contributing to energy security and independence. This gas has been the primary source of energy for the

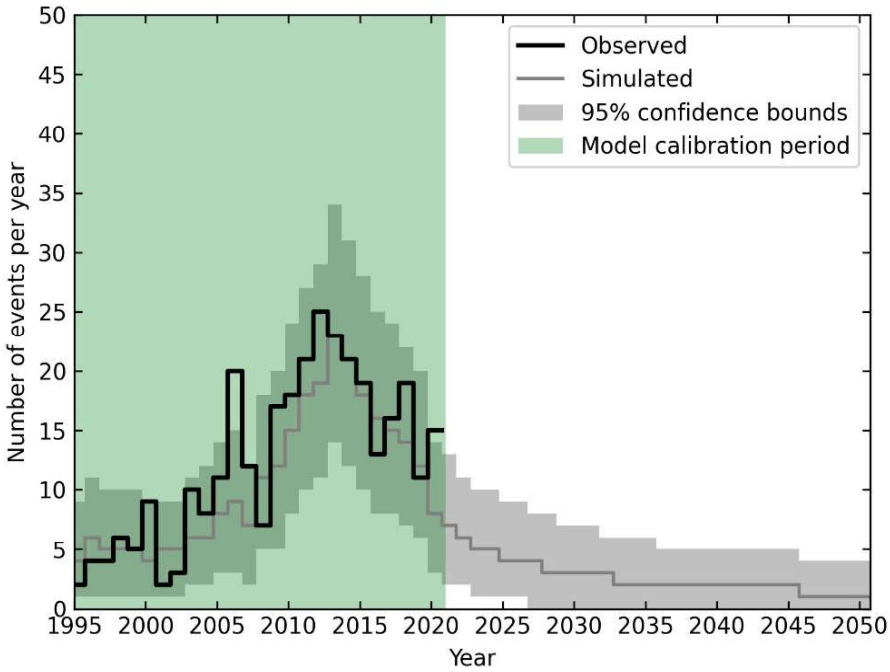

Figure 1.1.: A forecast of the number of earthquakes in the Groningen gas field following field shut-down [8].

populations of the Netherlands and is used by neighboring countries [10].

The composition of the Groningen gas, like natural gas reservoirs in general, primarily consists of methane gas (CH_4). However, it has a high nitrogen (N_2) content of roughly 14%. This makes the gas low-calorific. A low-calorific gas provides a lower amount of energy compared to when less N_2 is present. The low-calorific gas from the Groningen field has become the standard for the consumers in the Netherlands. For example, the gas stoves in Dutch households were designed for a low-calorific gas [11].

As of 2015, approximately 75% of the Groningen gas has been extracted. This occurred over a remarkable 55-year period of gas production. Before production, the Northern Netherlands (where the Groningen field is located) had no records of natural earthquakes, and the region was considered tectonically stable. However, with increased gas production from the Groningen field, more earthquakes were identified, and these events registered larger magnitudes on the Richter scale [12].

The Groningen gas field has been the focus of numerous scientific studies aimed at improved understanding of induced seismicity within the field. These investigations reveal that the change in the stress state has impacted faults, resulting in their reactivation. Such fault reactivation is identified as a potential cause of induced earthquakes [13].

To address the issue of induced seismic events in Groningen, the Dutch government

implemented measures to reduce gas production. In 2018, it was decided to cease production by 2030. This deadline was moved forward to 2023. There has since been a decline in annual production. The production was scaled down from an unusually high 54 bcm per year in 2013 to 4.5 bcm per year in 2022. Present international circumstances have prompted a new policy where gas production is partly continued at a "minimum flow" rate of 2.8 bcm per year [14]. It is expected that with the reduction, and eventual end to gas production from the field, the induced seismic events also stop. This was shown in Figure 1.1.

As technological advancements continue to push the boundaries of subsurface extraction and/or storage, it is essential to perform rigorous scientific research with the hopes of mitigating induced seismic events in the future. To achieve this goal, it is necessary to understand the mechanisms that lead to such unfavorable situations via various research techniques, such as simulation. The subsequent section outlines some of the computational approaches employed in studying and simulating faulted poroelastic media.

1.3. COMPUTATIONAL METHODS FOR SIMULATION OF FAULTED RESERVOIRS

Computational geomechanics has been a focal point of research in the past decade, due to its vast applications. It plays a critical role in production optimisation and safety assessments [15, 16]. Examples can be found, e.g., in studies related to hydraulic fracking [17], quantification of surface subsidence [18], geothermal energy extraction [19], CO_2 sequestration [20], hydrogen energy storage [21, 22], and, importantly, induced seismicity [23].

Numerical models for induced seismicity have evolved over the years. Earliest proposed models for geo-systems proposed loosely coupled flow dynamics and mechanics [24, 25]. Later, iterative or sequentially coupled [26] and fully coupled methods [27] emerged. These incorporate the effects of geomechanical deformation on flow parameters (such as permeability and porosity) and vice versa (e.g., the effect of pressure on fault stability). Fully-coupled approaches add to the computational costs, but extend the simulation stability compared with their loosely-coupled predecessors [26].

Modeling efforts for mechanical deformation originally relied on linear elastic deformation. Contributions from viscoplasticity, elastoplasticity and creep were later recognized and included [28, 29]. Thermo-poroelasticity models are used when non-isothermal fluid flow is considered in deformable media. [30, 31].

Fault stability was initially modeled based on a simple Coulomb failure criterion [32]. This model correlates the normal stress on the fault with a maximum threshold, beyond which the fault slips. More realistic quasi-static and dynamic friction models were later developed by incorporating more complex physics of fault re-activation. These include slip weakening or strengthening models [33, 34], rate and state models [35–37] and more recently the CNS model [38–40]. Dynamic frictional fault slip models are used to capture more complex behavior. In these models, parameters such as energy dissipation rate, damage potential, slip velocity,

slip duration and thermal weakening effects are considered [41]. These models do well in characterising laboratory friction experiments, but challenges still remain in scaling up the results to make them relevant for real-field natural fault systems [42].

The choice of the numerical discretization approach for the faulted poroelastic system, be it finite volumes (FVM) [43, 44], elements (FEM), or differences (FDM) [44, 45], is not an obvious one [46]. Given that each offer problem-specific advantages, all have been adapted individually, or in combination with each other for flow and mechanics. The FDM has been the earliest discretization scheme, due to its simplicity and convenience for structured grids. One motivation behind the development of newer integral-based discretization techniques (FVM and FEM) is the limitation of the FDM in handling complex geometries especially in multiple dimensions [47]. The FEM was originally developed for static stress analysis but expanded well beyond its scope. It remains the most widely used method in computational mechanics. This is in part due to its versatility in handling highly heterogeneous, geometrically intricate domains with irregular boundaries [48]. However the FEM requires more modeling effort in comparison with the FDM and the FVM. Also, it is the second best option for flow modeling after the FVM. This is because the FVM is locally conservative at the discrete level [49]. The FVM has the combined advantage of the FDM in being relatively simple to implement, and the FEM in having flexibility towards complex geometries.

Another method commonly used for fault simulation is the (spectral) boundary element method (BEM). In this method, the fault geometry is discretized into boundary elements and often Green's functions are used to solve for stress and displacement on the fault [50–52].

Initially, the computational mesh used for capturing the geological domain was always a structured mesh, imposed on the heterogeneous geological field. Later unstructured meshes were also utilized to capture discontinuities (e.g. faults and fractures) by confining them at grid interfaces. However, for complex geometries, this representation often becomes overly detailed making subsequent calculations impractical [53–56].

Embedded methods use appropriate relationships to link the fault network to the matrix with minimal mesh complexities [57–60]. The embedded framework has been used with both the FEM (e.g. XFEM [61–63]) and FVM with sequentially-coupled [64, 65] and fully-coupled [66] flow-mechanics simulations. A benchmark study was performed to compare the quality of the embedded-structured and conforming-unstructured mesh approaches for single-phase flow in porous media [67].

The embedded FVM (EFVM) was successfully used for determining pressure and displacements in a faulted system under pore pressure variations. Flow and mechanics were loosely coupled using a sequential coupling approach based on a fixed-stress scheme [64, 65]. Later, the computational efficiency and condition number of the EFVM was compared to the XFEM [68]. This showed the EFVM is much faster in terms of CPU time, but has a higher condition number. There are two reasons for this. First, for each direction, there is one additional unknown per cell in the EFVM, whereas there are at least four in the XFEM. Second, the EFVM

integrals are found analytically, while the XFEM uses numerical integration.

Despite the recent progress in the EFVM, major challenges remain for reliable simulation of fault reactivation in the context of induced seismicity. First of these is the incorporation of fault slip as a fully-implicit fully-coupled process with direct functionality of pore pressure and deformation. This plays an essential role when the geologic setting exhibits a strong physical association of mechanics with flow, such as in the case of production from faulted gas reservoirs [69]. A weak or sequential coupling may potentially result in conditionally stable results for multi-physics problems [26] or becomes more expensive in terms of CPU performance [70].

Second is the accurate calculation of the stresses affecting faults. These stresses are fundamental in identifying the stick-slip situation and quantifying the correct value of slip. But an element of nonlinearity arises due to the inter-dependence of slip on post-processed stresses. This requires iterations to ensure the estimated fault slip remains in agreement with the most recent stress field. Third is the occurrence of oscillations in the stress and slip profiles of the faults. This is observed in previous EFVM results [64, 65]. These oscillations arise due to the embedded nature of the EFVM, primarily when faults are misaligned with the matrix mesh. While the embedded framework is quite convenient for heavily-faulted systems [71], these oscillations pose a substantial hindrance to the monotonicity and stability of the implicit EFVM.

There are studies which have specifically focused on the simulation of depletion and injection-induced seismicity in the Netherlands. The Royal Netherlands Meteorological Institute (KNMI) documented the first seismic event in the Netherlands in 1986. Since that time, seismic activity has been documented in over 30 Dutch gas fields, most notably, the Groningen field [72].

In 1994, Roest and Kuilman looked at the relationship between gas production and tremors in the Netherlands and performed a geomechanical analysis of the reported seismic events in Eleveld gas reservoir [73]. They looked at the effect of the geometry of the reservoir on induced seismicity and found that fault throw has prominent effect on fault slip.

In 2003, Mulders used 3D geomechanical modeling to analyze the effects of factors such as reservoir compartmentalization, rock stiffness (Young's modulus and Poisson's ratio), stress field orientation, initial state of stress, the influence of the surrounding rock properties and reservoir and fault geometry to assess seismic energy release in the development of gas fields [74].

In 2014, van Wees et. al. reported on the influencing factors affecting induced seismicity based on gathered data from over 190 gas fields in the Netherlands where only 15 of them experienced seismicity. They reported that major seismic activity is more probable in pre-existing faults as a result of compaction. Their findings indicate that faults in these fields are initially far from critically stressed. These faults typically do not become active before the gas reservoirs reach around 28 percent of depletion of the initial gas in place [75].

In 2015, van den Bogert performed a sensitivity analysis to delve deeper into the issue of induced seismicity in the Groningen gas field. A finite-element based numerical solver was used in this study. The parameters considered included

reservoir offset, in-situ stresses, fault friction behavior, fault orientation, reservoir thickness and elastic properties of the system [76]. In 2018, Van den Bogert complemented the earlier 2015 report, with a focus on residual friction coefficient, reservoir offset, reservoir thickness and the slope of the slip weakening relationship. Their simulations captured the point of nucleation and the seismic growth of the rupture in the seismic stage [77]. Similar numerical simulations were also conducted by Buijze et. al. in 2015, and later in 2017 [72, 78].

Besides the numerical methods reviewed so far, another branch of simulation techniques were developed for the study of induced seismicity: analytical and semi-analytical methods. These methods offer multiple advantages. They are usually based on fewer parameters than numerical models. This allows for easier interpretation of the simulation results [79]. When it comes to resolving the issues with estimation of stresses (such as stress peaks in a reservoir with a fault throw), analytical and semi-analytical methods hold a clear advantage in their accuracy [80]. Furthermore, they are generally computationally simpler and much faster than numerical methods [81]. However, they can be limited in that it is not as straightforward to include complexities in these models. These complexities include some of the important real-field parameters such as geological heterogeneities and geo-model geometry.

Analytical and semi-analytical methods used for modeling fault slip are based on fracture mechanics and dislocation theory. Dislocation theory was originally used in the study of material properties and deformation [82]. It was later extended to earth sciences. In geophysics, dislocation theory is used to model the movement along fault planes, the patterns of stress distribution, and the factors influencing earthquake generation and propagation. This is because a fault plane that has experienced slip due to applied stresses, can be considered as an array of dislocations in itself. Here, slip is defined where the fault surfaces have shifted over a confined region [83]. The elastic fields of dislocations in isotropic media have been studied as far back as the beginning of the $20th$ century [84].

Earlier analytical and semi-analytical studies of stresses in the deep subsurface focus on the issue of depletion-induced subsidence. This concern was predominantly reported by the oil and gas industry. In 1966, Geertsma looked at subsidence as a results of production-induced reservoir compaction [85]. Later in 1973, he complemented his study on this topic and specifically considered the Groningen field. He suggested there are higher risks associated with subsidence in the Groningen field [86].

One of the most well-known solutions to describe the impact of variations in geometry and elastic properties on the local stress state was proposed by Eshelby in 1957 [87]. He modeled the elastic strain field perturbations resulting from a change in size or shape in an inclusion inside an infinite medium. He employed a method that begins by extracting the inclusion from the surrounding medium. The inclusion is allowed to experience a stress-free transformational strain. Subsequently, precise surface tractions are applied to restore the inclusion to its initial size and shape. Afterwards, the inclusion is reintegrated into the matrix material, welded and the interfacial boundary tractions is eased. Eshelby (1957) demonstrated the procedure

for computing the constrained strain field that emerges once the interfacial tractions are eased [87].

In 1985, Segall analyzed stress changes as a results of fluid production from a reservoir to evaluate induced seismic events for the 1983 Coalinga Earthquake [88]. In 1989, he suggested that earthquakes can be triggered by poroelastic stresses due to reservoir pore pressure reduction resulting from fluid production. He used constitutive equations for linear poroelastic media and suggested analytical models to describe the phenomena. He made the following conclusions regarding the issue [89]:

- Seismic activity has demonstrated a spatial and temporal correlation with production activities in certain oil and gas fields, where pore pressures have experienced significant declines, often reaching several tens of MPa. Reports of production-induced seismic activity near oil and gas fields have been recorded since the 1920's, such as the case of the earthquakes near the Goose Creek oil field in south Texas [90].

- Both reverse faults above and below petroleum reservoirs, and normal faults on the flanks of reservoirs have been observed to be influenced by pore pressure reduction.

- The theory of poroelasticity can explain how fluid extraction creates localized alterations in the stress state.

- The calculated stress changes correlate well with observed earthquake locations.

In 1992, Segall explained the underlying physics of induced seismicity in oil and gas fields as follows: During depletion, reservoir pore pressure reduction is higher in the reservoir layers than the surrounding. This situation results in a strain imbalance, where reservoir rocks compact more than the surroundings. This imbalance creates additional stresses which can trigger induced seismic events [91].

Later in 1994, Segall et. al. studied induced seismicity near the Lacq gas field in France. They examined changes in the stress field as results of depletion-induced subsidence. They correlated the stress change with the spatial occurrence of induced seismicity [69].

In 2001, Du and Olson analytically analyzed the effect of pressure variations within a reservoir on subsidence and rock compaction [79]. A year later, Walsh (2002) developed another analytical method for calculating the fluid production-induced subsidence. His method yielded a more precise estimate of the surface subsidence [92]. In the same year, Rudnicki generalized the work of Walsh (2002) and reported on the similarities and differences between the study by Walsh (2002) and the studies by Geertsma ([85, 86]) and Segall ([91]) [93].

In 2008, Soltanzadeh and Hawkes studied stress changes and fault reactivation for horizontal and inclined reservoirs under plain strain conditions. They reported that fault reactivation depends on the geometry and dip angle of the reservoir [94].

More recently, Jansen et. al. (2019) analytically calculated stresses, strains and corresponding displacements as a result of fluid depletion and injection in faulted

reservoirs [80]. Jansen and Meulenbroek (2022) extended the earlier work by Jansen et. al. (2019) [95]. They analyzed the onset of fault nucleation based on an earlier study by Uenishi and Rice (2003) [96]. Following the determination of the nucleation pressure, they suggested a method for calculating the magnitude of the seismic moment for vertical and inclined faults. In 2023, this work was extended to account for non-uniform pressure fields [81]. The work conducted by Jansen et. al. in 2019 and Jansen and Meulenbroek (2022) serves as a basis for the semi-analytical and hybrid methods developed in this work. These studies were developed for a single-fault system with a relatively straightforward geometry, leaving opportunities for further exploration and enhancement. Furthermore, another aspect meriting further development is extending the analytical expressions to model post-nucleation fault behavior.

1.4. AN OVERVIEW OF RESEARCH OBJECTIVES, SCOPE AND METHODOLOGY OF THIS STUDY

This project was defined within the Science4Steer project. Science4steer aims to provide a scientific basis for fluid production and re-injection strategies to minimize induced seismicity in Dutch gas fields. Science4steer investigates this problem in different scales from the lab to the field scale.

The Science4Steer project falls under the scope of a larger project known as DeepNL. The goal of the DeepNL research program is to improve the fundamental understanding of the dynamics of the deep subsurface under the influence of human interventions.

The current study aims to analyse computational methods for the study of induced seismicity in reservoirs undergoing pressure change. This involves simulating fault slip, matrix deformation, and fault and matrix pressure in faulted poroelastic media at the field scale. An effort is made to follow a physics-based approach where relevant processes and mechanisms which affect the faults are taken into consideration. This study takes advantage of the vast body of knowledge available in the field of computational geomechanics, relevant models used in the study of induced seismicity and the available real field data from the Groningen gas field.

A notable emphasis within this work is placed on examination, validation, and accurate documentation of the limits in the methodologies used for modeling fault reactivation. This study takes on the challenge of simulating fault reactivation using a combination of methods. These methods are 1. numerical simulation approach, 2. semi-analytical approach and 3. hybrid approach. The subsequent section offers brief reviews of each.

1.4.1. NUMERICAL METHOD

A finite-volume based, embedded numerical approach, called the Smooth Enhanced Finite Volume Method is developed to model heterogeneous faulted poroelastic systems. The sEFVM is a fully-implicit fully-coupled smoothed embedded finite volume approach for modeling poroelastic deformation and fault slip.

This computational framework accommodates the consideration of heterogeneous properties within rock formations and faults. One key aspect addressed in the sEFVM is the oscillation observed in stress and slip profiles along fault planes, arising from the embedded fault representation. These oscillations have implications for simulation of slip, prompting means to mitigate them. Additionally, an iterative strategy is introduced to achieve implicit full coupling of fault slip, pore pressure, and rock deformation. This novel approach enhances the accuracy of fault slip predictions within the numerical framework.

To validate the efficacy of the sEFVM, a comprehensive set of numerical test cases are studied. These cases benchmark the method against available analytical solutions. The sEFVM is shown to effectively simulate deformation and fault slip for complex geological models.

The sEFVM is applied to examine fault configurations relevant to the Groningen field. These setups include faults in reservoirs with offset. In the case of depletion in such systems, the stress profiles demonstrate infinite peaks at offset points and are not continuous. This poses a significant challenge to the sEFVM, leading to diminished accuracy when stress discontinuity exists over the fault.

The infinite peaks and discontinuous shear stress profiles in reservoirs with offset are accurately simulated using an analytical approach in a study by Jansen et. al. (2019) [80]. This motivates the development of a semi-analytical method.

The sEFVM is not en entirely new method. It shares its methodological framework with XFVM originally proposed by Deb and Jenny [65]. The term "enhanced finite volume" in the definition of sEFVM, as opposed to "extended finite volume" in XFVM does not indicate otherwise. The sEFVM deviates from XFVM in the following respects:

- The pressure-mechanics system is solved in a fully-coupled manner. This implementation is aimed at enhancing stability within the computational framework in comparison to when the pressure-mechanics system is sequentially coupled.

- The sEFVM incorporates a procedure to smooth slip profiles. This step is considered for maintaining the convergence of the method, especially when dealing with faults characterized by arbitrary grid-misaligned angles.

1.4.2. SEMI-ANALYTICAL METHOD

The study by Jansen et. al. in 2019 and Jansen and Meulenbroek in 2022 present analytical expressions for the estimation of stresses and aseismic fault slip resulting from pore pressure change [80, 95]. These studies look at single-fault systems in a reservoir with relatively simple geometry.

In the context of this research, these formulations are extended to accommodate the mesh structure of the sEFVM, thereby enabling their application within a semi-analytical framework. The semi-analytical method facilitates the consideration of multiple faults and builds on previous analytical formulations that were tailored to simpler reservoir configurations.

The developed semi-analytical approach is found to agree with analytical solutions. It provides more accurate solutions for stress and slip profiles for faulted reservoirs with an offset, in comparison to the sEFVM.

One drawback of the semi-analytical method is that it is unable to simulate post-nucleation fault behavior. That is when the the slip of a fault outgrows the domain of aseismic slip. In the case of multi-fault systems, semi-analytical simulations only continue up to the point of nucleation of the first fault. Beyond this point, the state of the nucleated fault is unclear and semi-analytical simulations cannot proceed.

The limitation of the semi-analytical method motivates the development of an approach enabling the simulation of fault reactivation both before and after fault nucleation.

1.4.3. HYBRID METHOD

It is reported that in faulted media, slip distributions in one fault can influence nearest neighbouring faults through perturbations in the stress fields [97, 98]. A hybrid method is developed that takes this into consideration in a quasi-static sense.

In the hybrid method, the incremental stresses incurred as a result of nucleation of a fault (and subsequent rupture growth) are incorporated numerically in the overall stresses. Assumptions are made with respect to the post-seismic frictional behavior of the faults. The stress perturbations resulting from seismic rupture are accounted with the use of sEFVM. The hybrid method is used to simulate fault slip before nucleation, and after nucleation in the seismic slip stage. This method is found to be effective in simulating more realistic multi-fault setups.

1.5. THESIS OUTLINE

This thesis is structured in the following manner.

CHAPTER 2: PHYSICS OF FAULTED POROELASTIC SYSTEMS

In the next chapter, the physics associated with flow, deformation and fault slip in faulted poroelastic media are reviewed.

This is followed by an overview of underlying physical equations which are used for the estimation of stresses in specific setups of this study.

Subsequently, a brief overview is given on friction models relevant in the study of induced seismicity in the Groningen field.

Finally, equations for determination of the onset of fault nucleation are discussed.

The chapter ends with a discussion on the validity range for the analytical method used within the framework of the semi-analytical and hybrid methods of this study.

CHAPTER 3: METHODOLOGY

This chapter consists of three main sections which explain the assumptions and implementation of 1. the numerical sEFVM, 2. the semi-analytical method and 3. the hybrid method.

In the first part, a description of the embedded mesh, the basis functions, the finite-volume control volumes, the method used for including the slip discontinuity in the basis functions, and the iterative procedure of the sEFVM is discussed.

In the second part the semi-analytical method is explained. This part begins with a review of the analytical expressions used for estimation of stresses and slip as suggested by Jansen et. al. (2019) [80]. It is demonstrated how these expressions are extended to be solved over the sEFVM computational domain. Lastly, the algorithmic implementation of the semi-analytical method is explained.

In the last part of Chapter 3, the hybrid method is detailed in terms of its link to the semi-analytical method and the sEFVM.

CHAPTER 4: RESULTS AND DISCUSSION

The results in Chapter 4 follow the same pattern as the previous chapter where results for the three methods are presented in a consecutive order.

Initially, the sEFVM is validated against analytical solutions and is benchmarked against alternative simulation methods. This chapter serves to establish the credibility and robustness of the sEFVM for the simulation of faulted poroelastic media.

Next, specific Groningen-relevant test cases are modelled where limitations of the sEFVM become evident. The inaccuracies are evaluated against analytical solution and another grid-conformal finite volume-based method. This is followed by results of the semi-analytical model. The method is benchmarked against earlier analytical solutions.

The semi-analytical method is used to simulate a wide range of reservoir-fault configurations. Simulation results are qualitatively used in the evaluation of the more consequential parameters in the study of induced seismicity. Findings are compared with previous research relevant to the Groningen field.

Finally, some results for the hybrid method are presented and discussed. This section shows the extension of results to multi-fault systems and modeling of quasi-static seismic slip. It ends with application of the results to a more realistic model for the Groningen field.

CHAPTER 5: CONCLUSIONS

In Chapter 5, an overview of the findings of this study is presented. Looking back at the entirety of the thesis, contributions and limitations of each method are reappraised.

Furthermore, based on the performed sensitivity analysis, some remarks are made on the topic of induced seismicity in the Groningen field.

This chapter also provides ideas for potential future directions in the domain of simulation of faulted poroelastic media.

2

PHYSICS OF FAULTED POROELASTIC MEDIA

The intricate interplay between geological structures (e.g. presence of a reservoir offset or faults), fluid movement and mechanical responses defines the behavior of subsurface formations under stress. The first step to modeling the geomechanics of faulted poroelastic systems is understanding the underlying physics. This chapter reviews the fundamental equations that define faulted poroelastic systems, providing a comprehensive investigation of the mathematical expressions that describe the coupling between stress, strain, fluid flow, porous media deformation and fault re-activation. This chapter also includes a discussion regarding the development of the aseismic slip patch and potential rupture.

2.1. PHYSICS OF FLOW IN FAULTED POROELASTIC MEDIA

The single-phase mass conservation equations for a slightly-compressible poroelastic domain and flow-conductive fractures and faults based on the embedded discrete fracture modeling (EDFM) approach read [57, 59]

$$b\frac{\partial \nabla\cdot\vec{u}}{\partial t}+\frac{1}{M}\frac{\partial p_m}{\partial t}+\nabla\cdot\Big(-\frac{k_m}{\mu}\cdot\nabla p_m\Big)+\Psi_{m\to f}=Q_m, \tag{2.1}$$

and

$$\frac{\partial E_f}{\partial t}+\nabla\cdot\Big(-\frac{ak_f}{\mu}\cdot\nabla p_f\Big)+\Psi_{f\to m}=Q_f, \tag{2.2}$$

where b is the Biot coefficient, $\vec{u}$ is matrix deformation, t is time, M is the Biot modulus, p is pressure, k is permeability, μ is phase viscosity, Ψ is the net flux exchanged between the matrix and fracture/fault, Q is the source term, a is fracture/fault aperture and E^f is the total accumulation in the fracture/fault. Subscripts m and f stand for the matrix and fault/fracture, respectively.

Parts of this chapter have been published in the Journal of Computational Physics (2022) [99].

The term E_f becomes negligible if the change in the aperture (e.g. dilation) and porosity of flow-conductive faults and fractures (ϕ_f) is neglected, because

$$\frac{\partial E_f}{\partial t} = \left[\frac{1}{\rho}\frac{\partial}{\partial t}(a\rho\phi_f)\right] \approx \frac{\partial}{\partial t}(a\phi_f). \tag{2.3}$$

Note that one can include dilation due to slip to further model the void aperture E_f term [100].

2.2. PHYSICS OF DEFORMATION IN FAULTED ELASTIC MEDIA

The linear momentum balance for a poroelastic domain with faults and fractures can be stated as

$$\nabla \cdot (\widetilde{\sigma} - bp\widetilde{I}) + \vec{f} = 0, \tag{2.4}$$

where $\widetilde{\sigma}$ is the effective stress tensor, $\widetilde{I}$ is the identity matrix and $\vec{f}$ is the body force per unit volume [101]. Assuming linear elastic deformation [101], stress is linearly proportional to the displacement gradient, i.e.,

$$\widetilde{\sigma} = \widetilde{C} : \nabla^s \vec{u}, \tag{2.5}$$

where ∇^s is the symmetric gradient operator and $\widetilde{C}$ is the elasticity tensor consisting of elasticity parameters [101].

2.3. PHYSICS OF FAULT SLIP IN FAULTED POROELASTIC MEDIA UNDERGOING PRESSURE CHANGE

Fault slip occurs when the tangential stresses on the fault, i.e., τ, surpass the maximum threshold value, i.e., τ^{max}. Here, the Coulomb/Byerlee friction law [32] is applied to quantify τ^{max} as

$$\tau^{max} = |\tau_c| + \mu_f \cdot \sigma_n. \tag{2.6}$$

Here, μ_f is the friction coefficient, τ_c is the cohesive force of the contact, and σ_n is the normal stress on the fault. Where not mentioned in this study, the value of τ_c is taken as zero.

2.4. INITIAL AND BOUNDARY CONDITIONS FOR A WELL-POSED PROBLEM

The governing equations described so far are subject to proper initial and boundary conditions for both flow and mechanics to form a well-posed system of equations. These conditions in general form can be expressed as

$$\text{Prescribed boundary displacement:} \quad \vec{u} = \vec{u}_{\partial\Omega_{u,D}} \tag{2.7a}$$

$$\text{Prescribed boundary total stress:} \quad (\widetilde{C} : \nabla^s \vec{u} - bp\widetilde{I}) \cdot \vec{n}_{\partial\Omega_{u,N}} = \vec{f} \tag{2.7b}$$

$$\text{Prescribed boundary pore pressure:} \quad p = p_{\partial\Omega_{p,d}} \tag{2.7c}$$

$$\text{Prescribed boundary flux:} \quad -(\frac{k_m}{\mu} \cdot \nabla p) \cdot \vec{n}_{\partial\Omega_{p,N}} = Q \tag{2.7d}$$

$$\text{Initial pressure:} \quad p_{\Omega_p} = p_{\Omega_p}(t = 0) \tag{2.7e}$$

$$\text{Initial displacement:} \quad \vec{u}_{\Omega_u} = \vec{u}_{\Omega_u}(t = 0) \tag{2.7f}$$

Here, $\vec{n}$ is the unit normal vector to the corresponding boundaries of flow and mechanics. In addition, sub-indices $\bullet_{,D}$ and $\bullet_{,N}$ indicate the part of the displacement and pressure domain boundaries ($\bullet \in \{\partial\Omega_p, \partial\Omega_u\}$) in which Dirichlet (D) and Neumann (N) boundary conditions are imposed. Note that the union of the Dirichlet and Neumann boundary interfaces form the entire domain boundary, i.e., $\Omega_{p,D} \cup \Omega_{p,N} = \Omega_p$ and $\Omega_{u,D} \cup \Omega_{u,N} = \Omega_u$.

2.5. ANALYTICAL ESTIMATION OF STRESSES AND DEFORMATION

2.5.1. A RELEVANT SETUP IN THE STUDY OF INDUCED SEISMICITY

This section describes relevant setups for the study of induced seismicity in the deep subsurface and the relevant fundamental relationships to define them.

Figure 2.1 shows three images. The left image shows a cross-section from the geomechanical model of the Groningen field. The captured area has a size of 45 km (horizontally) by 4.5 km (from a depth of 0 down to -4.5 km subsurface depth). Details on how this cross section is obtained are provided in Appendix C.

If a segment, consisting of the reservoir and some depths of the overburden and underburden are cropped out of this cross-section, the central image in Figure 2.1 is obtained. This cut-out can be modelled with the simplistic schematic shown on the right side of the aforementioned figure.

The simplistic schematic in Figure 2.1 is a well-known representation for a faulted buried reservoir section. Similar setups have been considered in literature for the simulation of fault reactivation in the Groningen gas field [76, 77, 80, 95, 102].

This setup is a two-dimensional model, with height H and width W. There is a porous reservoir in the center with a thickness of $t_h = h_1 + h_2$. The reservoir, shown in a darker shade in Figure 2.1, is surrounded by the overburden and underburden layers. Flow can occur in the reservoir, as it is considered porous. The segments outside of the reservoir are impermeable.

The entire domain is assumed to have uniform isotropic elastic properties. This simplification is intended for the ease of calculating the stresses analytically later.

There is a fault extending through the entire block, passing through the center point of the domain. The reservoir has an offset at the location of the fault.

This offset is also referred to as the fault throw. Based on the definitions in Figure 2.1, the size of the offset is $t_o = h_2 - h_1$.

The vertical height of the domain, H, is finite. While the entire frame is shown as a square, an assumption can be an infinitely-extending reservoir in the horizontal direction ($W \sim \infty$). This is a valid assumption for very large fields, such as the Groningen gas field. In the current example, the width to height ratio of the realistic cross-section of Figure 2.1 is 10 to 1, based on the actual dimensions of the cross section which is 45 km×4.5 km.

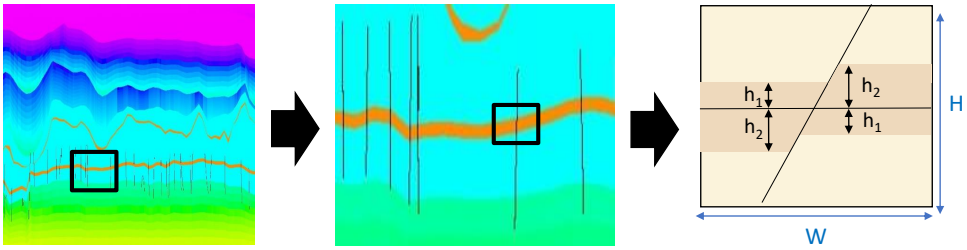

Figure 2.1.: An illustrative model (right) inspired by the Groningen gas field model (left and center). The darker shade shows the permeable reservoir. The images on the left and center are extracted from the geomechanical model developed for the Groningen gas field. Details of this model are presented in Appendix C.

To simulate induced seismicity in the setup of Figure 2.1, the relevant processes are considered. These consist of:

- **Initialization**: In the first step, the initial in-situ stresses and pressure existing in the depositional environment are calculated. The cropped domain is extracted from a larger environment. Therefore, in order to simulate the system when the domain is modelled independently, it needs to be subjected to forces that replicate the presence of the eliminated external environment.
- **Depletion**: In the second step, the reservoir pressure change is simulated. This step is to simulate what happens during production from gas reservoirs.

Each of the above steps is described next.

2.5.2. INITIALIZATION OF STRESSES AND DEFORMATION

INITIAL IN-SITU STRESS CALCULATION

To begin with a simple test case, it is initially assumed that the reservoir is not faulted and there is not an offset in the system (i.e. $h_1 = h_2$). This setup is shown in Figure 2.2. This image shows the reservoir with the applied boundary conditions. These boundary conditions consist of vertical loads on the top and bottom, horizontal loads on the sides and three points with restricted movement to constrain rigid body translations and rotation.

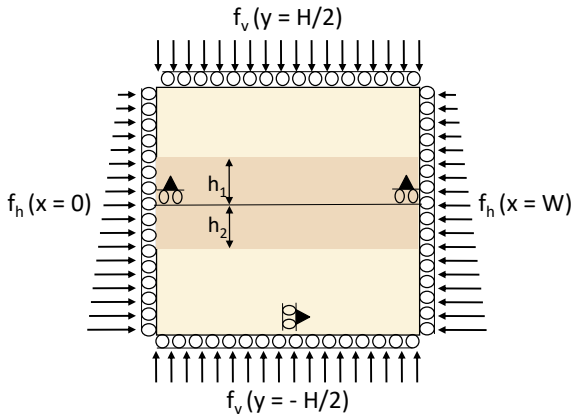

Figure 2.2.: Schematic of load configuration and mechanical boundary conditions to simulate initial stresses. Vectors illustrate the stress direction imposed on the boundaries.

The vertical load on the system, f_v, at depth y depends on fluid density, ρ_{fl}, solid rock density, ρ_s, and rock porosity, ϕ_s, as

$$f_v(y) = \sigma^0_{yy}(y) = [(1-\phi)\rho_s + \phi\rho_{fl}]g(y - D_0), \tag{2.8}$$

In Equation 2.8, g is the acceleration of gravity and D_0 is the depth at the center of the reservoir. σ^0_{yy} is the initial vertical stress. This formula is used for determining the vertical load at the top, and bottom of the model in Figure 2.2. The vertical load can be interpreted as a consequence of the presence of the overburden and underburden layers surrounding the system. The sign of the force is different at the bottom and the top of the domain. This is incorporated in Equation 2.8 by considering y to be positive or negative with respect to the reference depth of D_0.

In addition, there is also another vertical load applied to the system. This second vertical load is due to the effect of gravity on the system itself and is calculated similarly using Equation 2.8.

It is usual, that a ratio is considered between the initial effective horizontal to vertical in-situ stresses. This ratio, denoted here as K^0, is referred to as the coefficient of earth pressure at rest [103]. Based on this idea, the horizontal load, f_h, is

$$f_h(y) = -\sigma^0_{xx}(y) = -\left\{K^0[\sigma^0_{yy}(y) + bp^0(y)] - bp^0(y)\right\}, \tag{2.9}$$

where b is the biot coefficient, σ^0_{xx} is the initial horizontal stress and $p^0(y)$ is the initial pressure distribution.

The initial pressure is calculated based on the initial pressure, p^0_0 at the reference depth (i.e. D_0) as

$$p^0(y) = p^0_0 - \rho_{fl}\, g\, y \tag{2.10}$$

When the model is subjected to vertical and horizontal forces, it may displace (move in the 2D space), and/or rotate. This does not happen in reality for the reservoir. Therefore, to prevent this during the simulation, movement in three points of the model are restricted. This is done by considering

$$u_y(0, \frac{L}{2}) = 0, \tag{2.11a}$$

$$u_y(W, \frac{L}{2}) = 0, \tag{2.11b}$$

$$u_x(\frac{W}{2}, 0) = 0. \tag{2.11c}$$

In Equation 2.11, u_y is the vertical displacement, u_x is the horizontal displacement, the first input in the parenthesis is the horizontal coordinate and the second input in the parenthesis is the vertical coordinate.

With the considerations so far, the initial stresses will be

$$\sigma^0_{xx}(y) = -\frac{1}{2}[f_h(0) + f_h(H)] + [f_h(0) - f_h(H)]\frac{y}{H}, \tag{2.12}$$

$$\sigma^0_{yy}(y) = \frac{1}{2}[f_v(0) + f_v(H)] + [(1-\phi)\rho_s + \phi\rho_{fl}]gy, \tag{2.13}$$

$$\sigma^0_{xy}(y) = 0. \tag{2.14}$$

The initial zero shear stress is not necessarily representative of actual reservoir conditions but is a simplifying assumption made here.

Stress can be found along other orientations with proper mathematical manipulations. This is of interest, for example, when calculating the stresses along a fault line. The stresses tangential and normal to the fault line are of interest when studying the fault friction law as described in Equation 2.6.

The normal stress, σ^0_n, and shear stress τ^0 acting on a fault line making an angle of θ with respect to the horizontal are [95]

$$\sigma^0_n(y) = \sigma^0_{xx}(y)\sin^2\theta + \sigma^0_{yy}(y)\cos^2\theta \tag{2.15a}$$

$$\tau^0(y) = \frac{1}{2}[\sigma^0_{xx}(y) - \sigma^0_{yy}(y)]\sin 2\theta, \tag{2.15b}$$

where positive shear stresses are designated to the setup which promotes normal faulting, as opposed to a reverse faulting configuration.

INITIALIZATION OF DEFORMATION

For the configuration of Figure 2.2, deformation can be determined analytically. Deformation of a block of size $H \times W$ is related to strain, ϵ, as [101]

$$u_y^0 = \int_{-\frac{H}{2}}^{\frac{H}{2}} \epsilon_{yy}^0 \, dy, \tag{2.16a}$$

$$u_x^0 = -\int_{-\frac{W}{2}}^{0} \epsilon_{xx}^0 \, dx. \tag{2.16b}$$

In Equation 2.16, u^0 is the initial deformation and ϵ^0 is the initial strain resulting from the applied loads in the initialization stage.

Strain is a function of stress. By assuming poroelastic plain strain conditions, it is found as [101]

$$\epsilon_{yy}^0 = \frac{1}{E}(1-\nu^2)\sigma_{yy}^0(y) - \nu(1+\nu)\sigma_{xx}^0(y) + b(1+\nu)(1-2\nu)p^0(y), \tag{2.17a}$$

$$\epsilon_{xx}^0 = -\frac{W}{2E}[(1-\nu^2)\sigma_{xx}^0(y) - \nu(1+\nu)\sigma_{yy}^0(y) + b(1+\nu)(1-2\nu)p^0(y)]. \tag{2.17b}$$

In Equation 2.17, E is the Young's modulus and ν is the Poisson ratio. Conversion equations for these properties are presented in Appendix A.

Using Equation 2.17 and Equation 2.16, deformation can be determined based on initial stresses (Equation 2.14) and initial pressure distribution (Equation 2.10).

2.5.3. DEPLETION-INDUCED INCREMENTAL STRESSES AND DEFORMATION

RESERVOIR WITHOUT AN OFFSET

Following initialization, the setup of Figure 2.2 is assumed to undergo depletion. To simulate depletion, new boundary conditions are considered based on the results of the initialization step. A schematic of these boundary conditions is shown in Figure 2.3.

The depletion setup has prescribed boundary displacements which read

$$u_x(0,y) = u_x^0(0,y), \tag{2.18a}$$

$$u_x(W,y) = u_x^0(W,y), \tag{2.18b}$$

$$u_y(x,0) = u_y^0(x,0) + |u_y^0(x,H)|. \tag{2.18c}$$

In Equation 2.18, $u_x^0(0,y)$ and $u_x^0(W,y)$ are the horizontal displacements on the left and right boundary, respectively. These values are simulation outputs from the initialization stage.

According to Equation2.18c, the magnitude of the vertical displacement at the top, $u_y^0(x,H)$, and the bottom, $u_y^0(x,0)$ of the initialized model, are used to confine the displacement of the bottom boundary in the depletion setup.

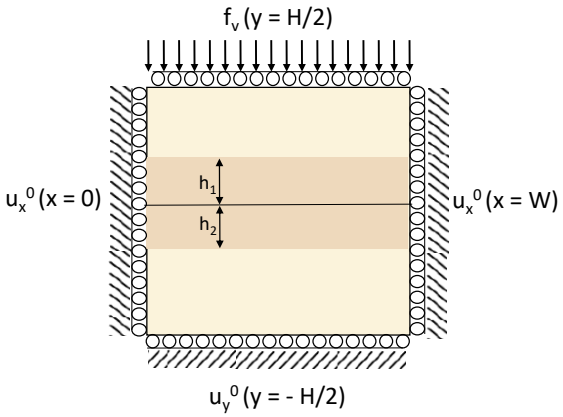

Figure 2.3.: Schematic of load configuration and mechanical boundary conditions to simulate depletion. A vertical load is applied on the top boundary to simulate the effect of overburden. On the left, bottom and right boundary, the displacement values obtained from the initialized model (Figure 2.2) are assigned.

The vertical load calculated in replacement of the overburden (Equation 2.8) continues to affect the system. The vertical load from gravity affecting the reservoir cells similarly remain as in the initialized case.

Reservoir depletion will result in uniform vertical deformation (compaction). The magnitude of this deformation depends on the thickness of the reservoir (t_h) as

$$\Delta h = t_h \epsilon_{yy}, \tag{2.19}$$

where ϵ_{yy} is the vertical strain. This property is defined as

$$\epsilon_{yy} = \frac{\sigma'_{yy}}{K_v}, \tag{2.20}$$

where K_v is the uni-axial vertical stiffness factor with definitions found in Appendix A. σ'_{yy} is the effective vertical stress resulting from pressure depletion and is

$$\sigma'_{yy} = b\Delta p. \tag{2.21}$$

In Equation 2.21, b is the Biot coefficient and Δp is the pressure depletion.

If the reservoir is assumed horizontally infinite, depletion does not enforce any additional horizontal strain, therefore

$$\epsilon_{xx} = 0. \tag{2.22}$$

However, there are incremental horizontal stresses. The incremental effective horizontal stress (σ'_{xx}) is found as [101]

$$\sigma'_{xx} = \frac{\nu}{1-\nu}\sigma'_{yy}, \tag{2.23}$$

here, σ'_{yy} is found according to Equation 2.21.

The total incremental horizontal stress (σ_{xx}) depends on pressure and is

$$\sigma_{xx} = \sigma'_{xx} - bp. \tag{2.24}$$

In a continuum system without faults, incremental shear stresses due to depletion are zero (i.e. $\sigma_{xy} = 0$). Given that the initial shear stresses are also zero (as shown in Equation 2.14), the total shear stresses remain zero after depletion (i.e. $\Sigma_{xy} = 0$).

However, in the same system without an offset, if the shear stresses are evaluated at an inclined angle (for example along the path of a delineated fault), they are not zero. The nonzero incremental horizontal stresses (calculated according to Equation 2.24), influence both the normal and shear stresses based on Equation 2.15.

It should also be noted that in this study, the effective stresses at the fault are calculated by assuming that the biot coefficient for the fault is the multiplier for the pressure term. An alternative definition exists for this multiplier, which aligns with the Terzaghi definition of effective stress. According to that definition, this multiplier is equal to unity [104].

RESERVOIR WITH AN OFFSET

A new setup is considered which includes a fault. This fault separates the reservoir into two compartments that have an offset with respect to each other. This is shown in Figure 2.4. Both reservoir compartments have the same thickness.

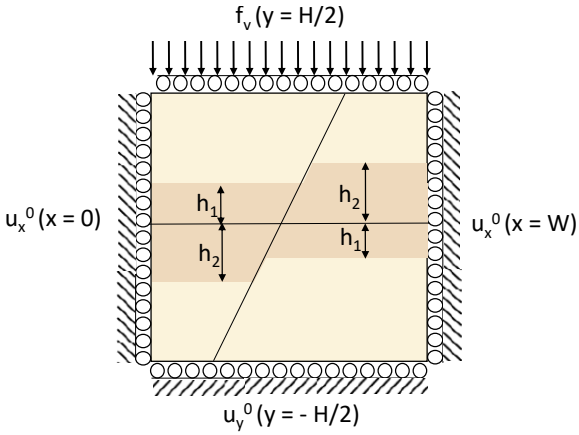

Figure 2.4.: Schematic for load configurations and mechanical boundary conditions for a faulted system with an offset. The vertical load on top and constant displacements on other boundaries are similar to those in Figure 2.3.

In the presence of a fault, friction is important. The friction coefficient appears in the definition of the Coulomb stress, Σ_C, as

$$\Sigma_C = |T| + \mu_f \Sigma_n^{'}, \tag{2.25}$$

where T is the total tangential stress and $\Sigma_n^{'}$ is the total effective normal stress. The definition for T and the total normal stress, Σ_n, is

$$T = \tau^0 + \tau^p, \tag{2.26a}$$
$$\Sigma_n = \sigma_n^0 + \sigma_n^p. \tag{2.26b}$$

In Equation 2.26, $\tau^{\Delta p}$ is the incremental shear stress due to depletion and $\sigma_n^{\Delta p}$ is the incremental normal stress due to depletion.

These terms are obtained with proper rotation of the incremental stresses along the direction of the fault line as

$$\sigma_n^p = \sigma_{xx}^p \sin^2\theta + \sigma_{yy}^p \cos^2\theta - \sigma_{xy}^p \sin 2\theta, \tag{2.27a}$$
$$\tau^p = \frac{1}{2}(\sigma_{xx}^p - \sigma_{yy}^p)\sin 2\theta - \sigma_{xy}^p \cos 2\theta. \tag{2.27b}$$

In Equation 2.27, σ_{xx}^p, σ_{xy}^p and σ_{yy}^p are the components of the incremental depletion-induced stress tensor.

The effective normal stress is calculated as

$$\Sigma_n' = \Sigma_n + \beta(p^0 + p), \tag{2.28}$$

where β may be equal to the Biot coefficient (i.e., $\beta = b$). It can also be taken as unity if the Terzaghi definition is used [104]. In this study, β is taken equal to the Biot coefficient.

The values of T and $\Sigma_n^{'}$ are used to calculate the Coulomb stress according to Equation 2.25. Another parameter in this equation is the friction coefficient which is addressed in the next section.

2.6. MODELS FOR THE FRICTION COEFFICIENT

The friction coefficient, featured in Coulomb stress equation (Equation 2.25), is crucial for assessing fault slip potential.

Under the simplest assumption, the friction coefficient can be held constant. However studies have shown that it can depend on the slip, or the rate of slip. With increasing slip or slip rate, the fault can weaken, meaning its friction coefficient drops. The friction coefficient can also strengthen with slip, meaning its friction coefficient will increase. In this section, some of the more well-known models for the friction coefficient are presented.

2.6.1. LINEAR SLIP-DEPENDENT FRICTION MODEL

A linear, slip-dependent friction coefficient can be defined as [95]

$$\mu_f(s) = \begin{cases} \mu_f^s + \frac{\mu_f^d - \mu_f^s}{\delta}|s| & s \le \delta \\ \mu_f^d & s > \delta \end{cases}$$

where μ_f^s is the static friction coefficient before any slip. After slip, the friction coefficient begins to change until it reaches the critical slip distance (or critical slip length) of δ. The value of the friction coefficient at a slip value of δ is equal to the dynamic friction coefficient, i.e. mu_f^d.

Figure 2.5 shows a schematic of a slip-dependent frictional weakening regime.

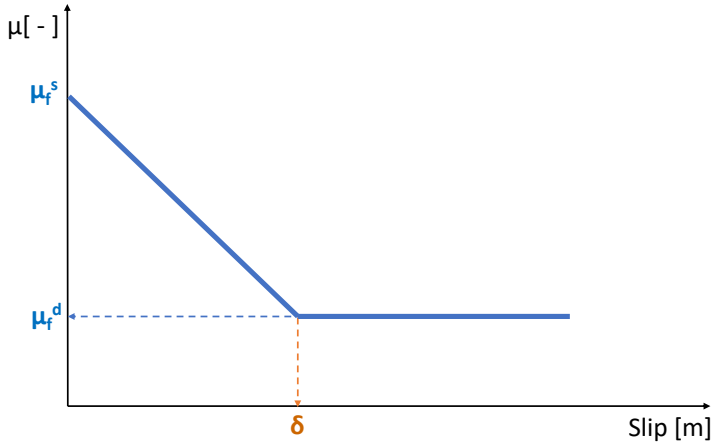

Figure 2.5.: Schematic of a linear slip-weakening friction behavior.

2.6.2. SLIP RATE-DEPENDENT FRICTION MODEL

Another model for the friction coefficient is the slip-rate dependent model. In this law, the friction coefficient depends on the rate of slip (i.e. change of the slip magnitude over time). By assuming steady state conditions as described by [105], the friction coefficient can be found as

$$\mu_f(V) = \mu_f^s + (A - B)\ln\frac{V}{V_0}, \tag{2.29}$$

where, V is the slip rate during depletion and V_0 is the slip rate at initial conditions. The parameters A and B are lab-determined coefficients. This model assumes there is an initial velocity for slip. This indicates that the fault slip even prior to nucleation.

2.7. SLIP PATCH GROWTH

In this section the stages of fault slip in a reservoir undergoing depletion are discussed.

2.7.1. INITIAL IN-SITU CONDITIONS

At initial conditions, before any depletion, the fault is affected by an initial stress regime. This initial stress depends on the geometry of the reservoir and the fault and the geomechanical properties of both. The governing relationships in Section 2.5.2 can be used for calculating these initial stresses. Two possibilities can exist based on the Coulomb stress affecting the fault at initial conditions

- **Case 1**: The initial Coulomb stress has a negative magnitude. This implies that the fault does not slip. Under this assumption, the system can be initialized for depletion according to the procedure explained in Section 2.5.3. Where the fault has a throw, points located at the tip of the offset will slip during depletion. With increasing depletion, it is possible for the Coulomb stress to become positive for larger sections along the fault. When this happens, the slip patch grows.
- **Case 2**: The initial Coulomb stress is positive. This indicates the fault already slips before any depletion. With this assumption, the procedure of Section 2.5.3 cannot be followed. This condition can favor the occurrence of a run-away rupture [106], which is addressed later in this section

The magnitude of the stresses on the system can be determined as

$$\Sigma_{xx} = \sigma^0_{xx} + \sigma^p_{xx}, \tag{2.30a}$$
$$\Sigma_{yy} = \sigma^0_{yy} + \sigma^p_{yy}, \tag{2.30b}$$
$$\Sigma_{xy} = \sigma^p_{xy}. \tag{2.30c}$$

Here, Σ is used to show total stresses. The superscripts ^{0} denote initial stresses, and σ^p_{xx}, σ^p_{yy}, and σ^p_{xy} are incremental stresses due to depletion.

For a fault line with an angle of θ with the horizontal direction, the acting shear and normal stresses are

$$\Sigma_n = \Sigma_{xx}\sin^2\theta + \Sigma_{yy}\cos^2\theta - \Sigma_{xy}\sin 2\theta, \tag{2.31a}$$
$$T = \frac{1}{2}(\Sigma_{xx} - \Sigma_{yy})\sin 2\theta - \Sigma_{xy}\cos 2\theta. \tag{2.31b}$$

Equation 2.31 is another representation for Equation 2.26 based on the definitions of total stresses in the x-y coordinate.

The threshold for slip, Σ_{sl}, for a friction regime without cohesion is

$$\Sigma_{sl} = -\mu_f \Sigma'_n, \tag{2.32}$$

where Σ'_n is the effective total normal stress calculated according to Equation 2.28. If $-\Sigma_{sl} \leq T$, fault will slip, otherwise there is no slip in the fault.

If the initial stresses acting on a fault (i.e. σ^0_{xx} and σ^0_{yy}) are large enough to meet the $-\Sigma_{sl} \leq T$ condition, slip occurs even before any depletion. In this situation the system is unstable and run-away rupture can occur [72].

Using the equations provided in this section, it is possible to identify a minimum threshold for the friction coefficient that ensures system stability, given a particular initial stress state.

2.7.2. DEPLETION-INDUCED FAULT SLIP

The analytically determined depletion-induced slip profiles for reservoirs with an offset indicate that there are points, exactly at the offset location, which will slip following even infinitesimal amount of fluid depletion [95].

There are two offset points along the fault: one in the shallower region (top) and another in the deeper part (bottom) of the reservoir. With a growing positive Coulomb stress acting on the fault, these slip patches will grow. The pace and the size of the slip patch growth is not identical for the shallower and the deeper slip patches. With increasing depletion, both slip patches grow in size. But for the simple one-fault model of Figure 2.3, the slip patch in the shallower section precedes that in the deeper section. For this case, the shallower slip patch is also larger in size. There may be instances where only one slip patch exists. Where there are two slip patches, they can influence each other. The magnitude of this influence depends on the distance between the slip patches [98].

With the growth of the slip patches, the following situations can occur [95]

- If a constant friction coefficient is considered, the slip patches grow and merge to create a single large slip patch. Fault nucleation before this merging is not captured.
- Assuming a linear slip-weakening friction regime, the slip patches grow with increasing depletion until reaching nucleation. At the nucleation point, there is a fast, sudden merging of the slip patches.
- Van den Bogert (2018) reports another condition under the linear slip-weakening regime. He reports that the slip patches can grow to merge without nucleation. Following nucleation, a single merged slip patch will continue to grow. Then, at a certain point, this single slip patch will nucleate [77].

According to the above description, when a slip-weakening friction law is considered, the slip patches will grow in size with increasing depletion until reaching nucleation. Any further depletion beyond the nucleation point will result in seismic rupture. This correlates with an induced seismic event.

For this reason, determination of the nucleation point is of high importance. The depletion pressure at which nucleation occurs is called the nucleation pressure [95].

2.7.3. FAULT NUCLEATION

Uenishi and Rice (2003) presented an analytical stability criterion for aseismic slip. They found an upper limit for the slip patch, up to which a fault remains stable with increasing shear stress [96]. Instability of the slip patch coincides with the nucleation point. Therefore their relationship is widely accepted for analytical determination of the nucleation point [76, 77, 95].

Uenishi and Rice (2003) used a linear slip-weakening law for the friction coefficient and found the critical slip patch size (Δy^*_{UR}) as [96]

$$\Delta y^*_{UR} = 1.158 \frac{G}{W_{av}(p)(1-\nu)}, \tag{2.33}$$

where G is the shear modulus, ν is the Poisson coefficient and $W_{av}(p)$ is a spatial average function defined as

$$W_{av}(p) = \frac{\int_{y_-}^{y_+} W(y,p)\, dy}{y_+ - y_-}, \tag{2.34}$$

where y_- and y_+ are the bounds of the slip patch along the vertical axis. $W(y,p)$ is a multiplier of the effective total normal stress (Σ'_n) and is defined as

$$W(y,p) = \frac{(\mu^s_f - \mu^d_f)}{\delta} \Sigma'_n, \tag{2.35}$$

where μ^s_f, μ^d_f and δ are constants of the linear slip weakening friction model defined in Equation 2.6.1.

It is possible to find nucleation point using simulation. However, using simulation is generally more time consuming. Simulation results are also more susceptible to precision-related errors. For this reason, Equation 2.33 is preferred for determining the nucleation point [80].

2.7.4. POST-NUCLEATION RUPTURE PROPAGATION

When nucleation takes place, there is an abrupt energy release, indicating the occurrence of an earthquake. The aseismic slip patch merges and creates what is referred to as a seismic slip patch, or a rupture.

In 2020, Buijze performed a dynamic study of rupture propagation in the Groningen field. She reports that the rupture can [102]:

- Grow until reaching the limits of the reservoir. This is referred to as a confined rupture. Buijze reports that most of their simulated ruptures are of this type and grow within the limits of the reservoir.

- Grow past the internal boundaries of the reservoir and arrest at a certain depth outside the reservoir. Buijze reports that some ruptures propagate into the underburden and the overburden in this manner.
- Grow indefinitely past the boundaries of the reservoir. There can be instances assumed where the rupture does not rest. This is referred to as a runaway rupture.

Buijze (2020) suggested a rupture has more potential to grow past the boundaries of the reservoir under the following conditions [102]

- The fault is critically stressed at initial in-situ conditions. This is explained in Section 2.7.
- The fault offset is small. Nucleation is promoted in reservoirs with a smaller offset but the developed rupture is smaller.
- There is a large drop in the stresses affecting the fault. This can be the result of a strong friction weakening regime. An example of this is a steep change in the friction coefficient from the static friction coefficient to the dynamic friction coefficient.
- If the fracturing energy is small. This energy is the energy that is dissipated during frictional weakening. When there is a linear slip weakening friction law, this is equivalent to the area under the slip weakening function, above the dynamic shear stress level. When the system has a higher potential for fracturing, the fault can propagate more easily.
- If the stress distribution over the fault does not impede rupture propagation. The Coulomb stress profile is discontinuous along the fault. Depletion creates peaks in Coulomb stress profile which result in slip at the offset points. There are also stress peaks at the tip of the reservoir boundary. These stresses, depending on their magnitude, can act as a barrier to rupture growth.

The study of Buijze (2020) showcases a range of rupture behaviors, from confined ruptures within reservoir limits to runaway ruptures that extend indefinitely. This study highlights the influence of factors like critical stress, fault offset, stress drop, fracturing energy, and stress distribution on the potential for rupture growth beyond reservoir boundaries [102].

3

METHODS FOR SIMULATION OF FAULTED POROELASTIC MEDIA

Three different methods are presented in this chapter. First is a finite volume-based approach that is customized for modeling fault reactivation in heavily-faulted poroelastic media. The development is called the Smoothed Enhanced Finite Volume Method (sEFVM). This method relies on the framework proposed by Deb and Jenny [65] which incorporates faults in an efficient embedded manner and finite volume basis functions are appended to allow for the direct calculation of slip at the fault nodes. The sEFVM finds the solution for displacement, pressure in the matrix, pressure in the fault in a fully implicit fully coupled manner.

The second development is the semi-analytical method. In the semi-analytical method, analytical expressions for estimating depletion-induced incremental stresses and fault slip are solved over the refined computational domain of the sEFVM.

Lastly, the hybrid method is introduced. The hybrid method extends the semi-analytical solution to simulate post-nucleation seismic slip. This method relies on relevant assumptions regarding the post-nucleation state of faults and numerical estimation of stress perturbations resulting from fault rupture.

3.1. THE SMOOTHED ENHANCED FINITE VOLUME METHOD: sEFVM

3.1.1. COMPUTATIONAL DOMAIN AND DERIVATIONS

In this section, the underlying framework for sEFVM is described. This framework is based on the methodology of the XFVM suggested by Deb and Jenny [65]. In this study, the "enhanced" nomenclature used in the sEFVM was chosen instead of "extended" in the XFVM only to substantiate the difference of the FVM approach to the extended finite element method known as XFEM [63].

Parts of this chapter have been published in the Journal of Computational Physics (2022) [99].

The finite volume method (FVM) is applied on staggered structured grids for both flow and mechanics. In this approach, the equations for mechanics and flow (as described in Section 2.1) are integrated over corresponding control volumes for mechanics (Ω_u) and flow (Ω_p) shown in Figure 3.1.

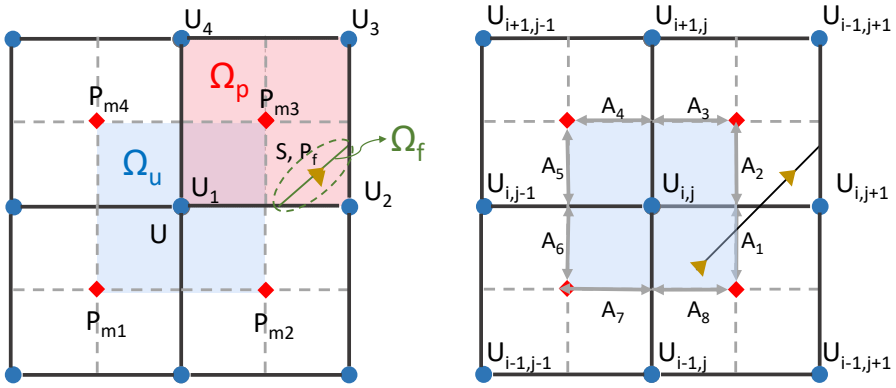

Figure 3.1.: Control volumes and numbering scheme for displacement and matrix pressure (top) and integration surfaces for mechanical control volume (bottom).

For flow inside a faulted poroelastic rock matrix, Equation 2.1 is integrated over the control volume for flow inside the matrix (Ω_p) as

$$b\int_{\partial\Omega_p}\frac{\partial\vec{u}}{\partial t}\cdot\vec{n}\;dS+\int_{\Omega_p}\frac{1}{M}\frac{\partial p_m}{\partial t}\;dV-\int_{\partial\Omega_p}\frac{k_m}{\mu}\cdot\nabla p_m\cdot\vec{n}\;dS+\int_{\Omega_p}\Psi_{m\to f}\;dV=\int_{\Omega_p}Q_m\;dV. \tag{3.1}$$

Faults are represented with a lower dimension than the matrix grid. Slip (s) and fault pressure (p_f) unknowns are located on the embedded fault. Clearly, the mesh for the reservoir and faults and fractures are completely independent. For flow inside the fault, Equation 2.2 is integrated over the displacement control volume of the fault, i.e. Ω_f, as

$$\int_{\Omega_f}\frac{\partial E_f}{\partial t}\;dS-\int_{\partial\Omega_f}\frac{ak_f}{\mu}\cdot\nabla p_f\cdot\vec{n}\;dl=\int_{\Omega_f}\Psi_{f\to m}\;dS+\int_{\Omega_f}Q_f\;dS. \tag{3.2}$$

In these equations, the net flux leaving the matrix to the fracture/fault domain is identified by $\Psi_{m\to f}$ [59], which is defined as

$$\Psi_{m\to f}=\eta\frac{k_m}{\mu}\frac{p_f-p_m}{V}. \tag{3.3}$$

Similarly, $\Psi_{f\to m}$ indicates the flux leaving fracture/fault to matrix, i.e.,

$$\Psi_{f\to m} = \eta \frac{k_m}{\mu} \frac{p_m - p_f}{A}. \tag{3.4}$$

Here, V and A are volume of matrix element and area of the overlapping fault cell. Moreover, η is the connectivity index between matrix and fault/fracture. For matrix cell (i, j) and fracture element k, it is defined as

$$\eta_{ij,k} = \frac{A_{ij,k}}{\langle d \rangle_{ij,k}}, \tag{3.5}$$

where $A_{ij,k}$ is the area fraction of the fracture element inside the matrix cell and $\langle d \rangle_{ij,k}$ is the average distance of a point inside the cell to the fracture segment. More details can be found in the literature [59, 71].

For mechanics, Equation 2.4 is integrated over control volume Ω_u as

$$\int_{\Omega_u} \nabla \cdot (\widetilde{C} : \nabla^s \vec{u} - bp\widetilde{I}) \; dV = \int_{\Omega_u} \vec{f} \; dV. \tag{3.6}$$

According to the divergence theorem [107], this integral is restated as

$$\int_{\partial\Omega_u} (\widetilde{C} : \nabla^s \vec{u}) \cdot \vec{m}_{\Omega_u} \; dS - b \left(\int_{\partial\Omega_u} p \; dS \right) \widetilde{I} = \int_{\Omega_u} \vec{f} \; dV, \tag{3.7}$$

where, $\partial\Omega_u$ is the boundary of the displacement control volume, which consists of 8 segments for each cell named A_1 to A_8 as shown in Figure 3.1.

The effective stress tensor is defined as

$$\widetilde{\sigma} = \begin{pmatrix} \sigma_{xx} & \sigma_{xy} \\ \sigma_{yx} & \sigma_{yy} \end{pmatrix}, \tag{3.8}$$

and by incorporating this definition into Equation 3.7 it is found that

$$\int_{\partial\Omega_u} (\sigma_{xx} - bp) \; dy + \int_{\partial\Omega_u} \sigma_{xy} \; dx + \int_{\Omega_u} f_x \; dV = 0, \tag{3.9a}$$

$$\int_{\partial\Omega_u} (\sigma_{yy} - bp) \; dx + \int_{\partial\Omega_u} \sigma_{yx} \; dy + \int_{\Omega_u} f_y \; dV = 0. \tag{3.9b}$$

for structured grids.

Using linear elasticity theory based on the first (λ) and second (G) Lame parameters, components of $\widetilde{\sigma}$ are

$$\sigma_{xx} = (\lambda+2G)\frac{\partial u_x}{\partial x}+\lambda\frac{\partial u_y}{\partial y}, \tag{3.10a}$$

$$\sigma_{yy} = (\lambda+2G)\frac{\partial u_y}{\partial y}+\lambda\frac{\partial u_x}{\partial x}, \tag{3.10b}$$

$$\sigma_{xy} = \sigma_{yx} = G\left(\frac{\partial u_x}{\partial y}+\frac{\partial u_y}{\partial x}\right). \tag{3.10c}$$

The elasticity parameters (λ) and (G) are assigned to mechanical control volumes (i.e. Ω_u). They can constitute a heterogeneous map over the domain.

If Equation 3.10 is placed in Equation 3.9, the momentum balance reads

$$\int_{d\Omega_u}\left((\lambda+2G)\frac{\partial u_x}{\partial x}+\lambda\frac{\partial u_y}{\partial y}-bp_m\right)dy+\int_{d\Omega_u}G\left(\frac{\partial u_x}{\partial y}+\frac{\partial u_y}{\partial x}\right)dx = -\int_{\Omega_u}f_x\,dV, \tag{3.11}$$

$$\int_{d\Omega_u}\left((\lambda+2G)\frac{\partial u_y}{\partial y}+\lambda\frac{\partial u_x}{\partial x}-bp_m\right)dx+\int_{d\Omega_u}G\left(\frac{\partial u_x}{\partial y}+\frac{\partial u_y}{\partial x}\right)dy = -\int_{\Omega_u}f_y\,dV. \tag{3.12}$$

These equations can be quantified based on the integrals of derivatives of displacement.

The displacement field is discontinuous when slip occurs. To capture this discontinuity it is suggested to append the regular, continuous part of displacement with a jump [108]. Based on this approach the appended displacement field is

$$\vec{u}\approx\sum_{i=1}^{4}N_i\vec{u}_i+\sum_{i=1}^{n_s}s_iW_i\vec{t}_i, \tag{3.13}$$

where s is slip. N_i are bi-linear FVM basis functions that interpolate displacement at local coordinates of (x,y) inside a block of dimensions Δx by Δy. These are

$$N_1(x,y) = \left(1-\frac{x}{\Delta x}\right)\left(1-\frac{y}{\Delta y}\right), \tag{3.14a}$$

$$N_2(x,y) = \left(\frac{x}{\Delta x}\right)\left(1-\frac{y}{\Delta y}\right), \tag{3.14b}$$

$$N_3(x,y) = \left(\frac{x}{\Delta x}\right)\left(\frac{y}{\Delta y}\right), \tag{3.14c}$$

$$N_4(x,y) = \left(1-\frac{x}{\Delta x}\right)\left(\frac{y}{\Delta y}\right). \tag{3.14d}$$

The numbering from 1 to 4 refers to corners of a square grid counted counter-clockwise beginning from the bottom-left as shown in Figure 3.1 for displacements.

For cells intersected by faults, the latter part of Equation 3.13 is included.

This term consists of tangential slip (s), directional component of the unit tangent vector to the fault ($\vec{t}$), and function W defined as

$$W(x,y) = \sum_{i=1}^{4} N_i(x,y) \left[H\Big(f(x,y)\Big) - H\Big(f(x_i,y_i)\Big) \right], \tag{3.15}$$

where H is a modified Heaviside function defined as

$$H(\zeta) = \begin{cases} -1 & \zeta \leq 0 \\ +1 & \zeta > 0 \end{cases} . \tag{3.16}$$

In Equation 3.15, $f(x,y)$ is the signed distance from the fault. Depending on which side of the fault a point is located, it will be positive or negative. The Heaviside value of $f(x,y)$ will be +1 or -1. This introduces a discontinuity into the model which is used to calculate the tangential slip. It is noted that the current framework allows for definition of a single fault node per matrix grid cell.

Figure 3.2 shows a plot of the FVM basis functions and $W(x,y)$ over a unit square grid. This image shows that the displacement is linearly interpolated inside each grid cell. In the case of a faulted grid, there is a jump at the location of the fault.

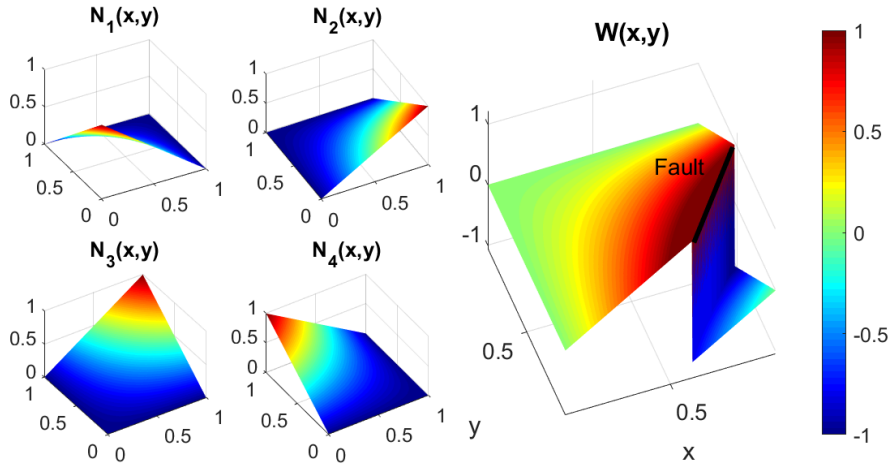

Figure 3.2.: Illustration of basis functions and the W function used in the EFVM.

The chosen form for Equation 3.13 gives the EFVM advantages. First, the simplicity of the bi-linear basis functions allows for analytical determination of the integrals in Equation 3.12. Here, the derivatives of the displacement are calculated analytically, and then integrated over the control volume surfaces of the structured grid considered in Figure 3.1.

One example of analytical derivation of the terms in Equation 3.12 is provided here. The integral in this equation contains derivatives of displacement which are found analytically based on definitions given in Equation 3.13 as follows

$$\frac{\partial u_x}{\partial y} = \frac{\partial N_1(x,y)}{\partial y} u_{x,1} + \frac{\partial N_2(x,y)}{\partial y} u_{x,2} + \frac{\partial N_3(x,y)}{\partial y} u_{x,3} + \frac{\partial N_4(x,y)}{\partial y} u_{x,4} + \frac{\partial W(x,y)}{\partial y} st_x. \tag{3.17}$$

The numbering scheme in Equation 3.17 follows that in Figure 3.1.

Next, derivatives in Equation 3.17 are calculated. One example for a derivative of a basis function is shown here as follows

$$\frac{\partial N_1(x,y)}{\partial y} = (\frac{-1}{\Delta y})(1 - \frac{x}{\Delta x}), \tag{3.18}$$

Another example for the derivative of the W function is

$$\begin{aligned}\frac{\partial W(x,y)}{\partial x} = \frac{\partial N_1(x,y)}{\partial x} \left[H\left(f\left(x,y\right)\right) - H\left(f\left(x_1,y_1\right)\right)\right] + \\ \frac{\partial N_2(x,y)}{\partial x} \left[H\left(f\left(x,y\right)\right) - H\left(f\left(x_2,y_2\right)\right)\right] + \\ \frac{\partial N_3(x,y)}{\partial x} \left[H\left(f\left(x,y\right)\right) - H\left(f\left(x_3,y_3\right)\right)\right] + \\ \frac{\partial N_4(x,y)}{\partial x} \left[H\left(f\left(x,y\right)\right) - H\left(f\left(x_4,y_4\right)\right)\right],\end{aligned} \tag{3.19}$$

where the values of $\left[H\left(f\left(x,y\right)\right) - H\left(f\left(x_i,y_j\right)\right)\right]$ are found numerically based on the local coordinates of corner points (x_i and y_i) at any location x and y. For each grid cell, this location is the coordinate of the fault node. Other terms in Equation 3.12 are similarly found.

Next, the integral in Equation 3.12 is determined. This integral is calculated analytically at boundary segments A_1 to A_8 shown in Figure 3.1. The range of integrals are from $\frac{-\Delta x}{2}$ to $\frac{\Delta x}{2}$ and $\frac{-\Delta y}{2}$ to $\frac{\Delta y}{2}$ for x and y, respectively. One example is provided for an integral over section A_1 as

$$\int_{A_1} \frac{\partial u_x}{\partial y} dx = [(\frac{-u_{x,1}}{8} - \frac{-3u_{x,2}}{8} + \frac{3u_{x,3}}{8} + \frac{u_{x,4}}{8}) + (\frac{-H_1}{8} - \frac{-3H_2}{8} + \frac{3H_3}{8} + \frac{1H_4}{8}) st_x] \frac{\Delta x}{\Delta y}. \tag{3.20}$$

Other integrals are obtained similarly. The multipliers for u_1 to u_4 are used to the coefficients for displacement.

For the multipliers of pressure in the momentum balance equation, the following term from Equation 3.12 is integrated as

$$\int_{\partial\Omega_u} -bp_m dy = \frac{-b\Delta y}{2}((p_{m_4} + p_{m_1}) - (p_{m_3} + p_{m_2})). \tag{3.21}$$

The numbering scheme is shown in Figure 3.1. The momentum balance equation is not assumed to be affected by fault pressure, multipliers of fault pressure are zero.

An advantage of the EFVM is that the total displacement function of Equation 3.13

includes the slip. The slip is calculated directly as an independent variable at the fault location and is not determined as a post-processed estimate. Furthermore, the EFVM can be used with embedded fracture/fault models for flow with the least amount of complexity.

Next, the friction law (Equation 2.6) is considered for the fault. Based on the τ^{max} obtained from friction law, the following is implemented based on the local shear stress for node i along the fault j (i.e. $\tau_{i,j}$):

$$\tau_{i,j} = \begin{cases} \tau_{i,j} & \tau_{i,j} < \tau_{i,j}^{max} \\ \tau_{i,j}^{max} & \tau_{i,j} \geq \tau_{i,j}^{max} \end{cases} . \tag{3.22}$$

In Equation 3.22, the shear stress (τ) is compared to τ^{max}, which depends on the normal stress (σ_n). These stresses are found by projection of the effective stress tensor onto the fault. This is done via defining the traction vector $\vec{T}_r$ as

$$\vec{T}_r = \tilde{\sigma} \cdot \vec{n}. \tag{3.23}$$

Here, $\vec{n} = n_x\vec{i} + n_y\vec{j}$ is the unit normal vector to the fault. Then, the normal and tangential stress components are

$$\sigma_n = \vec{T}_r \cdot \vec{n}, \tag{3.24a}$$

$$\tau = \vec{T}_r \cdot \vec{t}. \tag{3.24b}$$

Here, $\vec{t}$ is the unit tangential vector to the fault. Given that this vector is normal to $\vec{n}$, it has components $\vec{t} = n_y\vec{i} - n_x\vec{j}$. It is noted that the vector form for these stresses is used to represent the vector of scalar values of normal and tangential stresses along the nodes of the fault.

Equation 3.24 can be used to express the stresses at the fault location as

$$\sigma_n = (\lambda + 2Gn_x^2)\frac{\partial u_x}{\partial x} + (\lambda + 2Gn_y^2)\frac{\partial u_y}{\partial y} + 2Gn_xn_y(\frac{\partial u_x}{\partial y} + \frac{\partial u_y}{\partial x}), \tag{3.25a}$$

$$\tau = 2Gn_xn_y\frac{\partial u_x}{\partial x} - 2Gn_xn_y\frac{\partial u_y}{\partial y} + G(n_y^2 - n_x^2)\frac{\partial u_y}{\partial x} + G(n_y^2 - n_x^2)\frac{\partial u_x}{\partial y}. \tag{3.25b}$$

3.1.2. IMPLEMENTATION OF THE SEFVM

The sEFVM differs from XFVM [65] in two key implementation aspects. First, the XFVM finds the solution to the pressure-mechanics system with sequential coupling, while the sEFVM solves for a fully-coupled system. Furthermore, a smoothing procedure is included in the sEFVM to assist with oscillatory slip profiles that arise in the embedded method due to misalignment of the embedded faults with the underlying grid. These points are clarified further in this chapter.

In sEFVM, the momentum balance equation for the matrix, i.e. Equation 3.12, friction law for the fault, i.e. Equation 3.25, mass balance equation for the matrix, i.e. Equation 3.1, and mass balance equation for the flow-conductive fault, i.e. Equation 3.2, are solved together fully-implicitly and fully-coupled for the faulted poroelastic system, i.e.,

$$\begin{bmatrix} J_{uu} & J_{us} & J_{up_m} & J_{up_f} \\ J_{su} & J_{ss} & J_{sp_m} & J_{sp_f} \\ J_{p_m u} & J_{p_m s} & J_{p_m p_m} & J_{p_m p_f} \\ J_{p_f u} & J_{p_f s} & J_{p_f p_m} & J_{p_f p_f} \end{bmatrix} \cdot \begin{bmatrix} u \\ s \\ p_m \\ p_f \end{bmatrix} = \begin{bmatrix} f_u \\ c_s \\ Q_{p_m} \\ Q_{p_f} \end{bmatrix}. \tag{3.26}$$

The Jacobian matrix entries are identified by $J_{i,j},\ \forall\{i,j\} \in \{u, s, p_m, p_f\}$. Also note that the slip nodes at which the most-updated estimate of friction is equal or greater than the maximum tolerable friction are included in this system. All other slip nodes, i.e., belonging to stick condition, are excluded in the linear system of Eq. (3.26).

The procedure of the sEFVM for each time step is shown in Algorithm 1. In the first time step, the system of equations is solved using a continuum model (assuming there are no slipping nodes). This predictor-step solution is used as a first estimate for calculating stresses at the faults. The shear stresses along the faults, i.e. τ, are then obtained and compared to the maximum tolerable threshold of τ^{max}, as in Equation 2.6, for each fault. New degrees of freedom, i.e. $\vec{n}_s$, are then appended to the system of Eq. (3.26) only when, and where, the slip criterion is met (i.e. nodes which satisfy $\tau > \tau^{max}$). The new system is solved, stresses are recalculated, slip-stick conditions are re-identified and the procedure is repeated until convergence is reached.

Algorithm 1: Procedure of the sEFVM at each time step

Result: $[u_x, u_y, p_m, p_f, s']$

Solve poroelastic continuum model to find $[u_x, u_y, p_m, p_f]^1$; `// Initialize`

Calculate stresses $\vec{\tau}^1$ and $\vec{\sigma}_n^1$;

Determine frictional threshold $\vec{\tau}^{max,1}$ using Equation 2.6;

Find slipping nodes $\vec{n}_s^1$ where $\vec{\tau}^1 \geq \vec{\tau}^{max,1}$;

Set $\xi = 1$ and $\kappa = 1$;

while $\xi \neq 0$ **do** `// Begin iterative loop`

  Append system of equations with $\vec{n}_s^\kappa$ unknowns for fault slip;

  Solve poroelastic faulted model to find $[u_x, u_y, p_m, p_f, s]^{\kappa+1}$;

  Calculate stresses $\vec{\tau}^{\kappa+1}$ and $\vec{\sigma}_n^{\kappa+1}$;

  Find smooth stress profiles $\vec{\tau'}^{\kappa+1}$ and $\vec{\sigma'}_n^{\kappa+1}$; `// Smoothing of stress`

  Determine frictional threshold $\vec{\tau}^{max,\kappa+1}$ using Equation 2.6;

  Find new slipping nodes $\vec{n}_s^{\kappa+1}$ where $\vec{\tau'}^{\kappa+1} \geq \vec{\tau}^{max,\kappa+1}$;

  Update ξ, i.e., count of nodes for which stick-slip condition is changed ;

  Assign $(\kappa+1) \rightarrow \kappa$;

Find smooth slip profile s' ; `// Smoothing of slip`

As numerical examples will show in the results of Section 4.1, oscillations can arise in the fault stress (and slip) profiles of the EFVM. These oscillations are an anticipated consequence of the embedded incorporation of faults in the EFVM, when faults are misaligned with the matrix grid. An oscillatory stress profile will cause problems because it is used for determining stick-slip conditions. When an oscillatory stress profile is used, the slip-stick condition can fluctuate for a node, preventing the convergence to a consistent slip condition.

To resolve this challenge, a smoothing procedure is developed in this study. During iterations, the smoothing domain covers the stress profile for each fault. The fault stress profile has no overlap or gaps. So, a smooth profile is fitted to the original curve. The method for deriving this fit can vary.

The smoothed stress is used instead of the oscillatory curve, to find $\vec{n}_s$ again. If the estimates are different, the system is solved with new degrees of freedom for fault slip defined by the updated $\vec{n}_s$ vector. This is repeated until $\vec{n}_s$ remains unchanged. At that point, the procedure moves forward in time. For problems where faults are close to slip, neglecting this iterative step can result in incorrect results (as shown in later examples). For cases far from such conditions (e.g. the fault will clearly slip or remain stationary), the initial assumption is usually correct. For most problems, a single iteration is sufficient, thus the added computational load for the studied cases is found to be insignificant. The small number of iterations is believed to be due to the fact that there is little nonlinearity in the simplified physics of the studied model.

The slip profile may also demonstrate oscillations. For this reason, it is smoothed at the last time-step for improved interpretation.
In this study when not defined otherwise, the error ϵ is defined as

$$\epsilon = \frac{\left\| x_{ref} - x \right\|_\infty}{\left\| x^h_{ref} \right\|_\infty}, \tag{3.27}$$

where x_{ref} is the reference solution and x is the approximate solution.

Flow simulations are time-dependent. In this study, following the literature [109], dimensionless time t_D is obtained as $t_D = t/t_c$, where the characteristic time scale t_c is defined as

$$t_c = \frac{\mu\ \phi\ L^2}{\bar{k}\ \Delta p}. \tag{3.28}$$

Here, ϕ is rock porosity, $\bar{k}$ is average permeability, L is the characteristic length of the domain and Δp is the estimation of the pressure difference across the domain, e.g. the difference between injection and production pressures.

3.2. SEMI-ANALYTICAL METHOD

3.2.1. DEPLETION-INDUCED STRESSES

In the context of the semi-analytical and hybrid methods of this study, an approach described by Jansen et. al. (2019) [80] is adapted for calculating depletion-induced

stresses over faults. In this section, the adapted method is briefly reviewed.

Jansen et. al. (2019) use Green's functions (g_i) to give the displacement at a point (x, y, z) in direction $i \in x, y, z$ as a result of a unit force at point (ζ, ξ, ψ) in direction $j \in x, y, z$ as [80]

$$u_i(x, y) = \frac{C}{2} \iint_\Omega g_i(x, y, \zeta, \xi)\ d\zeta\ d\xi, \tag{3.29}$$

where C is

$$C = \frac{(1-2\nu)bp}{2\pi(1-\nu)G} \tag{3.30}$$

and g_i in Equation 3.29 are the Green functions found as

$$g_x(x, y, \zeta, \xi) = \frac{x-\zeta}{R^2} \tag{3.31a}$$

$$g_y(x, y, \zeta, \xi) = \frac{y-\xi}{R^2}, \tag{3.31b}$$

with R defined as

$$R = \sqrt{(x-\zeta)^2 + (y-\xi)^2}. \tag{3.32}$$

Strain is found according to

$$\epsilon_{ij} = \frac{1}{2}\left(\frac{\partial u_i}{\partial x_j} + \frac{\partial u_j}{\partial x_i}\right), \tag{3.33}$$

which gives

$$\epsilon_{xx} = C\frac{\partial}{\partial x} \iint_\Omega g_x(x, y, \zeta, \xi)\, d\zeta\, d\xi, \tag{3.34a}$$

$$\epsilon_{yy} = C\frac{\partial}{\partial y} \iint_\Omega g_y(x, y, \zeta, \xi)\, d\zeta\, d\xi, \tag{3.34b}$$

$$\epsilon_{xy} = \frac{C}{2}\left(\frac{\partial}{\partial x} \iint g_y(x, y, \zeta, \xi)\, d\zeta\, d\xi + \frac{\partial}{\partial y} \iint g_x(x, y, \zeta, \xi)\, d\zeta\, d\xi\right). \tag{3.34c}$$

Using Hook's law, stresses are written based on strain as

$$\sigma_{xx} = (\lambda + 2G)\epsilon_{xx} + \lambda\epsilon_{yy} - bp\delta_\Omega, \tag{3.35a}$$

$$\sigma_{yy} = \lambda\epsilon_{xx} + (\lambda + 2G)\epsilon_{yy} - bp\delta_\Omega, \tag{3.35b}$$

$$\sigma_{xy} = 2G\epsilon_{xy}. \tag{3.35c}$$

Combining equations 3.29 to 3.35, the general formula for total stress outside the reservoir is

$$\sigma_{ij}(x,y) = C \int\int_{\Omega} g_{ij}(x,y,\zeta,\xi)\, d\Omega. \tag{3.36}$$

A general formula for total stresses both inside and outside the inclusion is [80]

$$\sigma_{ij}(x,y) = C \left[\int\int_{\Omega} g_{ij}(x,y,\zeta,\xi)\, d\Omega, -2\pi\delta_{\Omega} \right], \tag{3.37}$$

where δ_{Ω} has a value of 1 inside the inclusion and 0 outside of it. This means that only for cells inside the reservoir, a value of 2π is deducted. The definitions for the Green's functions (g_{xx}, g_{yy} and g_{xy}) are available in [80] and will not be repeated here.

Equation 3.37 can be used for finding the Coulomb stress for a vertical frictionless fault (i.e. $\theta = 90^0$ and $\mu_f = 0$). For a frictionless fault, the Coulomb stress is equivalent to the tangential stress, and for a vertical fault, the tangential stress is σ_{xy}. With these assumptions and a geometry similar to Figure 2.4, the Coulomb stress is [95]

$$\Sigma_C(y) = \sigma_{xy} = \frac{C}{2} \ln \frac{(y-h_1)^2 (y+h_1)^2}{(y-h_2)^2 (y+h_2)^2}, \tag{3.38}$$

where C is defined in Equation 3.30.

3.2.2. FAULT SLIP

The semi-analytical and hybrid methods rely on the work of Jansen and Meulenbroek (2022) for finding a value for the slip profile analytically [95]. These authors use dislocation theory to quantify a slip profile that eliminates the positive Coulomb stress over the fault. A brief description of their procedure is provided in this section.

Jansen and Meulenbroek (2022) define an edge dislocation (δ) as a shear displacement along a semi-infinite slip line. They show that the shear stress from infinitesimal edge dislocations ($d\delta$) for plain-strain conditions is [95]

$$\widehat{\tau(s)} = D \int_{s_-}^{s_+} \frac{\nabla\delta(\xi)}{\xi - s}\, d\xi, \tag{3.39}$$

where s is slip and D is defined as

$$D = \frac{G}{2\pi(1-\nu)}, \tag{3.40}$$

and $\nabla\delta(s)$ is the slip gradient found as

$$\nabla\delta(\xi) = \frac{\partial\delta(s)}{\partial s}|_{s=\xi}. \tag{3.41}$$

The value of $\nabla\delta(s)$ is calculated based on mathematical inversion of Equation 3.39 as outlined in [80]. Following this inversion, slip is

$$\delta(s) = \int_{s_-}^{s} \nabla\delta(\xi)\, d\xi. \tag{3.42}$$

According to this procedure, the slip profile for the case of a vertical, frictionless fault with the geometry of Figure 2.4 is [95]

$$\delta(y) = \frac{C}{D} \begin{cases} 0 & \text{if } y \le h_2 \\ -(y + h_2) & \text{if } -h_2 \le y \le h_1 \\ (h_1 - h_2) & \text{if } -h_1 \le y \le h_1 \\ (y - h_2) & \text{if } h_1 \le y \le h_2 \\ 0 & \text{if } h_2 \le y, \end{cases}$$

where D and C were defined by Equations 3.40 and 3.30, respectively.

As mentioned in Section 2.7, where there are two slip patches along a fault, they are expected to influence each other [98]. However, in the analytical method discussed here, the interactions between slip patches is ignored. According to the findings of Jansen and Meulenbroek (2022), the interaction between slip patches affects the results when the slip patches grow closer to each other [95]. In ignoring this effect, it should be expected that the results of the semi-analytical and hybrid solutions of this study will not be precisely accurate for slip patches that have grown large enough in the vicinity of each other.

3.2.3. MAGNITUDE OF THE SEISMIC MOMENT

The seismic moment is a parameters used to quantify the magnitude of an earthquake. The magnitude of the seismic moment is important in the study of induced seismicity, because it provides an estimation of the energy released during seismic events [110].

The idea to use the seismic moment to measure the size of an earthquake is based on the equivalency of displacement (i.e. slip along a fault) and a double couple. In seismology, a "double couple" is characterized by two opposing forces acting in opposite directions along a fault plane. One force is a normal faulting motion, pushing rocks apart vertically, and the other is a dip-slip motion, causing horizontal motion along the fault. These two motions combined create the observed fault slip [111].

For the case of a linear slip-weakening fault, Jansen and Meulenbroek (2022) presented a relationship for determining the magnitude of the seismic moment (M_s) as [95]

$$M_s = G\left(\int_{y_{1,ps}}^{y_{2,ps}} \delta_{ps}(y)\, dy + \int_{y_{3,ps}}^{y_{4,ps}} \delta_{ps}(y)\, dy - \int_{y_1^*}^{y_2^*} \delta^*(y)\, dy - \int_{y_3^*}^{y_4^*} \delta^*(y)\, dy\right), \tag{3.43}$$

where G is the shear modulus and δ^* is the slip patch size at nucleation pressure. If the reservoir has the geometry of Figure 2.4, there will be two slip patches forming. This is explained in Section 2.7.

There will be a slip patch at the top and another at the bottom offset point. The variables y_1^* to y_4^* give the extension of these patches. The bottom patch will extend from y_1^* to y_2^* and the top patch from y_3^* to y_4^*. The parameter δ_{ps} is the post-nucleation seismic slip profile. This profile is obtained by assuming the fault seismic slip profile will continue to slip according to the dynamic friction coefficient (i.e. μ_f^d).

It is important to note that when using the dynamic friction coefficient at nucleation pressure, there may be two slip patches, or a single merged slip patch. If there are two patches, similarly as explained above, the first will extend from $y_{1,ps}$ to $y_{2,ps}$ and the second from $y_{3,ps}$ to $y_{4,ps}$. If there is just one merged patch, the two integrals of Equation 3.43 become one. In the case of one large merged slip patch, the seismic slip profile is then integrated from start to end (i.e. $y_{top,ps}$ to $y_{bot,ps}$) and included in the equation.

3.2.4. COMPUTATIONAL DOMAIN AND IMPLEMENTATION OF THE SEMI-ANALYTICAL METHOD

In Section 2 the formulas for analytical determination of initial in-situ stress were presented. In Section 3.2.1, the analytical expressions for calculation of depletion-induced stresses were presented. These equations show that stresses depend on the location of the fault and the cells undergoing pore pressure change. Depletion-induced stresses were determined by calculating Green function integrals over the cells of the domain undergoing pressure change.

For this purpose, the reservoir is subdivided into geometrical entities for the integrals to be calculated. The integrals are added back together based on the principle of superposition, to obtain the total value for the domain. The computational domain and procedure of the semi-analytical method are described in this section.

COMPUTATIONAL DOMAIN AND DERIVATIONS

In the study by Jansen et. al. (2019) [80], reservoirs with and without offsets are considered. The configuration of the reservoir where there is an offset is shown in Figure 2.4.

The computational domain they assumed is created by sub-dividing the depletion zone into four large domains consisting of two large triangles, and two large rectangles.

Later in 2023, Cornelissen and Jansen used a finer mesh consisting of many triangles and many rectangles [81]. This attempt is made to allow for the incorporation of the effect of non-uniform pressure fields in the depleting reservoir. The suggested grid by Cornelissen and Jansen (2023) conformed to the fault. They used same-size rectangles and triangles. Both studies in 2019 and 2023 focused on single-fault systems.

In the semi-analytical approach proposed in this study, the computational grid is more flexible. The flexibility is in allowing for the consideration of multiple faults and non-uniform geometry. The embedded gridding of the sEFVM, as shown

in Figure 3.1 is used for the semi-analytical, and later the hybrid method. The analytical expressions of Section 3.2.1 are solved over the refined grid of the sEFVM.

The computational gridding method used by Jansen et. al. (2019) [80], Cornelissen and Jansen (2023) [81] and the one of this study, are shown in Figure 3.3.

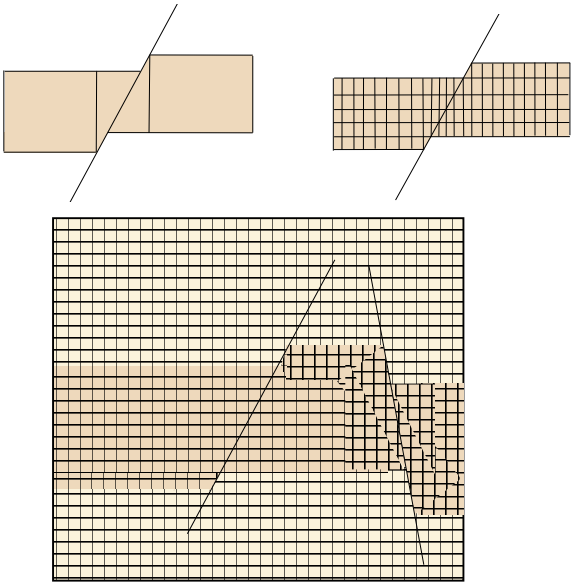

Figure 3.3.: The computational grid used by Jansen et. al. (2019) [80] (top left), Cornelissen and Jansen (2023) [81] (top right) and in this study (bottom).

Jansen et. al. (2019) provided expressions for the Green function integrals over triangular, rectangular (and trapezoidal) domains [80]. They defined these geometrical entities as shown in Figure 3.4.

Based on the location parameters of Figure 3.4, they defined Green function integrals as [80]

$$G_{ij}^{\text{rec}} = \int_r^s \int_p^q g_{ij}(x,y,\zeta,\xi)\, d\zeta\, d\xi, \tag{3.44a}$$

$$G_{ij}^{\text{tri}} = \int_r^s \int_{\frac{\xi}{\tan(\theta)}}^p g_{ij}(x,y,\zeta,\xi)\, d\zeta\, d\xi, \tag{3.44b}$$

where G_{ij}^{rec} is the Green function integral for rectangles and G_{ij}^{tri} the Green function integral for triangles.

It can be seen from Equation 3.44 that the orientation of the rectangle does not influence the Green function integral. Only the coordinates of the rectangle vertices are important. However, for the case of triangles (and trapezoids), the orientation influences the integral bounds, and therefore require attention. This can be seen in

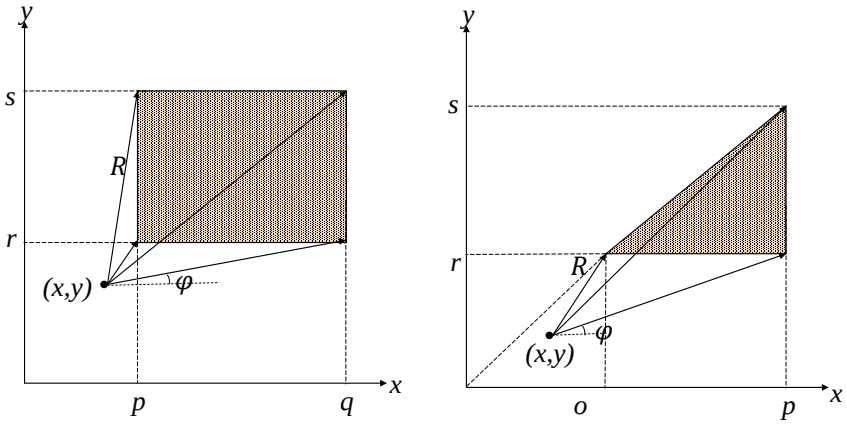

Figure 3.4.: Illustration of the shapes for integration of the Green functions in the hybrid method for the rectangle (left) and normal triangle (right) [80].

the integral bounds of Equation 3.44 for G_{ij}^{tri}.

The semi-analytical method used here calculates the integrals over the triangles and rectangles created by the more accurate geometry of the reservoir and the fault(s). This is explained for the case of a one-fault model.

The computational grid of the sEFVM is Cartesian and embedded. This implies that the fault passes through the grid independently of its alignment with the matrix mesh. Therefore, the faulted reservoir can be represented with a series of triangles, rectangles and trapezoids of various sizes and orientations. Trapezoids can be divided up into triangles and rectangles. Therefore, using analytical expressions for rectangles and triangles would suffice in capturing the computational domain.

This gives the sEFVM an advantage in being used for the development of a semi-analytical method. Various configurations that arise in the embedded mesh of the sEFVM are shown in Figure 3.5.

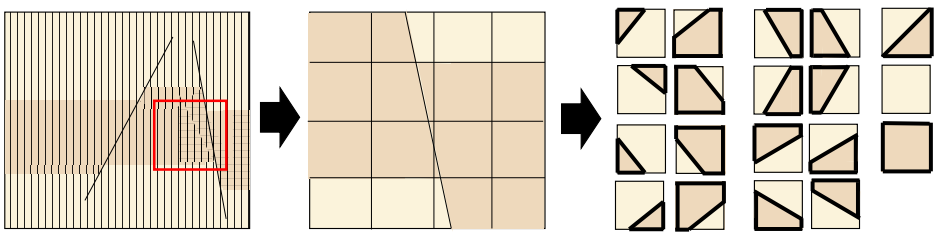

Figure 3.5.: Illustration of the possible configurations of the fault and the reservoir in the 2D computational domain used for the semi-analytical method.

As can be seen in Figure 3.5, there are four types of triangles. There can also be rectangles, and or a combination of a rectangle and a triangle in each cell.

The integration area used in Equation 3.44 depends on which side of the fault depletes. Clearly, only the depletion zone affects the depletion-induced stresses. Various forms of the triangle are shown in Figure 3.6. The triangles are defined as normal, up-side down, and mirrored version of both (i.e. mirrored normal and mirrored upside-down).

The "normal" triangle is the form shown in Figure 3.4. Other triangle orientations are shown in Figure 3.6.

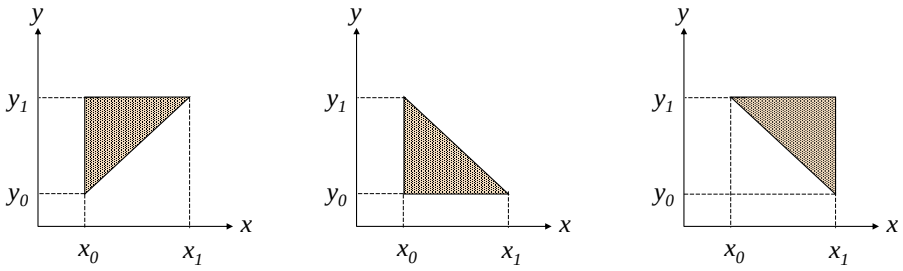

(a) upside-down (b) mirrored normal (c) mirrored upside-down

Figure 3.6.: Triangles of other orientations (than Figure 3.4) in the semi-analytical method.

The formulations for the normal triangle (Figure 3.6) are given by [80] as

$$G_{xx} = \int_{y_0}^{y_1} \int_{\frac{\xi}{\tan\theta}}^{x_1} g_{xx}\, d\zeta\, d\xi, \tag{3.45a}$$

$$G_{yy} = \int_{x_0}^{x_1} \int_{y_0}^{\zeta \tan\theta} g_{yy}\, dy\, d\zeta. \tag{3.45b}$$

Here, $x_0 = \min(o, p)$, $x_1 = \max(o, p)$, $y_0 = \min(r, s)$, and $y_1 = \max(r, s)$. According to this definition, the locations of points (o, r) and (p, s) are equivalent to (x_0, y_0) and (x_1, y_1), respectively. The definition for o, p, r and s can be found in Figure 3.4.

For the upside-down triangle, i.e. Figure 3.6a, the Green function integrals are re-written as

$$G_{xx} = \int_{r}^{s} \int_{x_0}^{\frac{\xi}{\tan\theta}} g_{xx}\, d\zeta\, d\xi = -\int_{y_0}^{y_1} \int_{\frac{\xi}{\tan\theta}}^{x_0} g_{xx}\, d\zeta\, d\xi = \int_{y_1}^{y_0} \int_{\frac{\xi}{\tan\theta}}^{x_0} g_{xx}\, d\zeta\, d\xi, \tag{3.46a}$$

$$G_{yy} = \int_{o}^{p} \int_{\zeta \tan\theta}^{y_1} g_{yy}\, dy\, d\zeta = -\int_{x_0}^{x_1} \int_{y_1}^{\zeta \tan\theta} g_{yy}\, dy\, d\zeta = \int_{x_1}^{x_0} \int_{y_1}^{\zeta \tan\theta} g_{yy}\, dy\, d\zeta. \tag{3.46b}$$

Here, $x_0 = \min(o, p)$, $x_1 = \max(o, p)$, $y_0 = \min(r, s)$ and $y_1 = \max(r, s)$. With this definition, the points (o, r) and (p, s) are equivalent to (x_1, y_1) and (x_0, y_0), respectively.

For the mirrored normal triangle, i.e. Figure 3.6b, the Green integrals become

$$G_{xx} = -\int_{y_0}^{y_1} \int_{\frac{\xi}{\tan\theta}}^{x_0} g_{xx}\, d\zeta\, d\xi, \tag{3.47a}$$

$$G_{yy} = -\int_{x_1}^{x_0} \int_{y_0}^{\zeta\tan\theta} g_{yy}\, dy\, d\zeta, \tag{3.47b}$$

where $x_0 = \min(o,p)$, $x_1 = \max(o,p)$, $y_0 = \min(r,s)$ and $y_1 = \max(r,s)$. Based on this definition, the points (o,r) and (p,s) are equivalent to (x_1,y_0) and (x_0,y_1), respectively.

Lastly, for the mirrored normal triangle, i.e. Figure 3.6c, the Green function integrals are

$$G_{xx} = -\int_{y_1}^{y_0} \int_{\frac{\xi}{\tan\theta}}^{x_1} g_{xx}\, d\zeta\, d\xi, \tag{3.48a}$$

$$G_{yy} = -\int_{x_0}^{x_1} \int_{y_1}^{\zeta\tan\theta} g_{yy}\, dy\, d\zeta, \tag{3.48b}$$

where $x_0 = \min(o,p)$, $x_1 = \max(o,p)$, $y_0 = \min(r,s)$ and $y_1 = \max(r,s)$. With this definition, the points (o,r) and (p,s) are equivalent to (x_0,y_1) and (x_1,y_0), respectively.

Using the above changes in how o, p, r and s are defined, the equations in [80] can be used for calculating the Green function integrals over triangular segments of all orientations.

Figure 3.5 shows possible segments that can arise in a Cartesian grid system. If a depleting cell is partly in the reservoir region, then the following can occur

- **Cell is not depleted**: where there is no pressure depletion (i.e. $\Delta p = 0$) the cell is not included in the calculation performed analytically over the fault.
- **Cell is entirely depleted**: the sEFVM mesh is Cartesian. Therefore if the grid cell is entirely in the depleted region, the rectangular formulas for g_{ij} are used.
- **Triangular depleted region is inside a cell**: if only a triangular corner of a cell undergoes depletion, g_{ij} are calculated for the triangle based on the orientations shown in Figure 3.6.
- **The entire cell, excluding a triangular corner, is depleted**: This setup is also shown in Figure 3.5. For this configuration, g_{ij}'s are determined by including the entire cell as a rectangle (using the g_{ij} for rectangle). Then, the non-depleting triangular segment is taken out (using the g_{ij} for the triangle as described in the previous bullet).
- **Trapezoidal depleted region is inside a cell**: If the depleted and non-depleted zones divide the cell from top to bottom, or left to right, two trapezoids form

on either side of the fault. For such setups, the trapezoid on the depleted side is used in the analytical method. As a trapezoid can be considered the sum of a rectangle and triangle, for this configuration, g_{ij} are calculated for both these shapes and added together to obtain the total g_{ij} for that cell.

The above calculations depend on the location of the integration points (i.e. o, p, r and s). These points depend on the location of the sEFVM mesh nodes, the geometry of the depleted zone (e.g. how the reservoir geology is defined and the offset) and the orientation of the fault (e.g. fault dip and and where the fault nodes are placed along the fault). In the semi-analytical method, these calculations are carried over from the sEFVM.

IMPLEMENTATION OF THE SEMI-ANALYTICAL METHOD

The procedure of the semi-analytical method for each time step is shown in Algorithm 2.

In the first step, in-situ stresses are initialized. This gives the initial deformation (u_x and u_y) field which will be used as bounds for the second simulation stage, where depletion is modeled. Initial pressure distribution is also calculated.

In the second step, the system is depleted in steps, until reaching a chosen final depletion pressure (i.e. p^{final}). In every depletion step, the Coulomb stress (σ_c) profiles are analytically calculated.

The Coulomb stress profile is used for the evaluation of slip. For any fault node where $\sigma_c \leq 0$, there is no slip. Otherwise, σ_c is used for calculating the slip according to the analytical solution which would reset σ_c to zero (as explained in Chapter 3).

Algorithm 3 is defined for the case of having a non-constant friction coefficient. When the friction coefficient depends on slip or slip-rate, both the slip and friction coefficient are found in an iterative manner. This means that the slip is calculated first and then it is used to find the friction coefficient. The new friction coefficient is used again to re-estimate slip and so on. Therefore, when a slip-dependent or slip rate-dependent friction law is used, the friction coefficient is iteratively estimated until the changes in the estimated friction coefficient reach a desired accuracy (e.g. $\Delta\mu_f \leq 1e-2$).

Algorithm 4 is used to detect nucleation. In this algorithm, the slip patch sizes are monitored. For each pressure step, the effective normal stress profiles over the slipping region are used for calculating the analytical Uenishi and Rice (2003) nucleation critical slip patch size [96]. When the size of the simulated slip patch size become equal or greater than the Uenishi and Rice critical value, the fault is assumed to nucleate. This criterion is used for the identification of the nucleation pressure.

Algorithm 2: Procedure of the semi-analytical method

Result: $[\sigma_n, \tau, s, \mu_f]$

Initialize $[u_x, u_y, p_m, p_f]^{i=0}$ according to Section 2.5.2. ;

Assume no slip: $[s]^{i=0} = 0$. ;

Set the initial friction coefficient: $[\mu_f]^{i=0}$. Assume no initial nucleation = 0. ;

Set i = 0 ; `// Initialize`

while $p \leq p_{max}$ ***and*** *nucleation* $= 0$ **do**

  $i = i + 1$;

  Deplete: $[p]^{i+1} = [p]^i + \Delta p^i$ according to Section 2.5.3;

  Find $[\sigma_c]^i$ according to 3.2.1 ; `// Analytical depletion-induced stress update`

  if $0 \leq [\sigma_c]^i$ **then**

    Calculate slip $[s]^i$ according to 3.2.2 ;

    if *slip-dependent friction law* **then**

      Run Algorithm 3 to find corrected $[s]^i$ and μ_f^i ;

    Run Algorithm 4 to detect nucleation pressure.;

    if *nucleation detected* **then**

      nucleation = 1 ;

Calculate the magnitude of the seismic moment according to Equation 3.43.;

Algorithm 3: Iterative determination of the slip and friction coefficient in case of a slip-dependent friction law

Result: $[s, \mu_f]$

Initialize error: $\varepsilon_s = 1$;

set tolerance:$\varepsilon_t = 1e-2$;

Initialize **while** $\varepsilon_s \geq \varepsilon_t$ **do**

  Calculate friction coefficient $[\mu_f]^i$ based on the governing friction law (Section B.0.3);

  Set $x_{ref} = [s]^i$;

  Calculate new slip $x = [s]^i$ according to Section 3.2.2.;

  $\varepsilon_s = \frac{|(x_{ref} - x)|_2}{|(x_{ref})|_2}$; `// Iterations for friction coefficient`

Algorithm 4: Detection of the nucleation pressure using the Uenishi and Rice (2003) method [96]

Result: $[s, \mu_f]$

Find top slip patch size: y^i ;
Extract the corresponding section of the effective normal stress profile that pertains to y^i ;
Calculate $W(y,p)$ from Equation 2.35 ;
Calculate $W_{\text{av}}(p)$ by integrating $W(y,p)$ over y^i ;
Calculate the critical length using Equation 2.33 as $[y^*_{UR}]^i$;
if $[y^*_{UR}]^i \geq y^i$ **then**
    Report nucleation pressure of $[p_n]^{(i)}$

Algorithm 2 runs until one of the following two outcomes occur:

- The depletion pressure is reached prior to reaching nucleation.
- Nucleation occurs. In this case the semi-analytical simulation ends. This algorithm only captures aseismic fault slip and cannot simulate the system further.

To visualize the procedure of the semi-analytical method, Algorithms 2, 3 and 4 are summarized in the flow-chart of Figure 3.7.

In order to simulated post-nucleation slip, the Hybrid method is developed. The procedure of this method is described next.

3.3. HYBRID METHOD

In this section, the hybrid method is introduced for the simulation of aseismic and seismic fault slip. This method builds up on the semi-analytical method by allowing quasi-static simulation of fault slip in the post-nucleation phase.

In the hybrid method, the stresses affecting the fault(s) consist of the effect of three factors. These are 1. the effect of initial stresses, 2. the effect of depletion. 3. the effect of seismic rupture of a fault on other faults (if present). In the semi-analytical method, only the first two were considered. In the hybrid method, the last effect is introduced.

The hybrid method is different from the semi-analytical method in that a new procedure is followed after a fault nucleates. Assumptions of the hybrid method are:

- During depletion, at least one fault will reach nucleation pressure and nucleate before reaching the final depletion pressure. Otherwise, the calculations of the hybrid method are the same as the semi-analytical method.
- When the depletion pressure exceeds the nucleation pressure of a fault, that fault will undergo seismic slip. This would create a post-seismic slip patch also referred to as rupture. This is explained in Section 2.7.

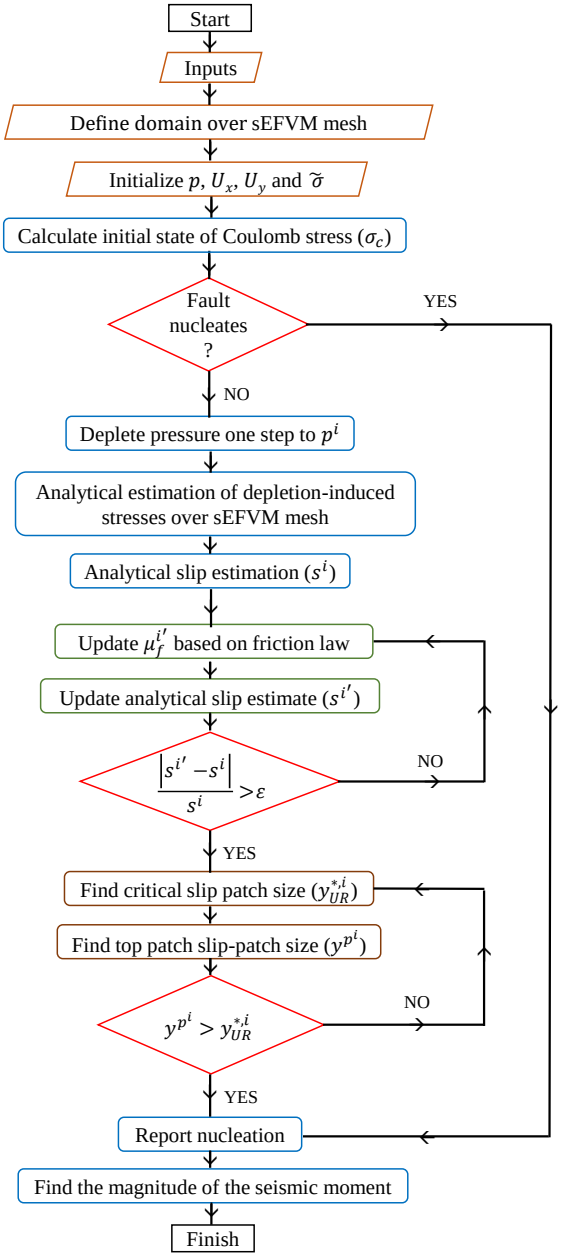

Figure 3.7.: A flow-chart outlining the procedure of the semi-analytical method for each fault.

- The size of the seismic rupture is determined assuming depletion would occur with a dynamic friction coefficient for the fault.
- With increased depletion exceeding nucleation pressure, the post-seismic slip patch will grow.
- The post-seismic slip patch will affect the local stress map, creating a new perturbed stress state.
- The new perturbed stress field is assumed to not affect the fault itself. It is assumed that such effects are already considered in the analytical solution.
- The new perturbed stress field can affect other faults, if other faults are located close enough and the effects are large enough in terms of magnitude.

The procedure of the hybrid method is shown in Algorithm 5.

Algorithm 5: Procedure of the hybrid method

Result: $[\sigma_n, \tau, s, \mu_f]$

Initialize $[u_x, u_y, p_m, p_f]^{i=0}$ according to Section 2.5.2. ;
Assume no slip: $[s]^{i=0} = 0$. ;
Set initial friction coefficient: $[\mu_f]^{i=0}$. ;
Assume no initial nucleation = 0. ;
Set i = 0 ; `// Initialize`
while $p \leq p_{max}$ **do**
    $i = i + 1$;
    Deplete: $[p]^{i+1} = [p]^i + \Delta p^i$ according to Section 2.5.3;
    Find $[\sigma_c]^i$ according to Section 3.2.1 ; `// Analytical depletion-induced stress update`
    if *nucleation = 1* **then**
        Run Algorithm 6 to update initial stress field.
    if $0 \leq [\sigma_c]^i$ **then**
        Calculate slip $[s]^i$ according to 3.2.2 ;
        if *slip-dependent friction law* **then**
            Run Algorithm 3 to find corrected $[s]^i$ and μ_f^i ;
        Run Algorithm 4 to detect nucleation pressure.;
        if *nucleation detected* **then**
            nucleation = 1 ;

Algorithm 5 is similar to that for the semi-analytical solution (Algorithm 2). However, it does not stop with the nucleation of the first fault. It continues to simulate the system until reaching a desired depletion pressure.

Algorithm 6 is used to update the stresses in the system as a result of dynamic slip. It incorporates the effect of dynamic slip with the assistance of the sEFVM. The algorithm is defined as follows:

Algorithm 6: Stress update following nucleation of a fault

Result: $[s, \mu_f]$

1 Initialize nucleation pressure $[p_n]^i$;

2 Assume $\mu_f = \mu_f^d$ at $[p_n]^i$ Calculate rupture size $[s^*]^i$ according to Section 3.2.2 ;

3 Calculate the deformation of the matrix $\Delta U_{x,y}$ due to rupture using the sEFVM ;

4 Calculate incremental stresses due to rupture using the sEFVM; Update $[\sigma_c]$ based on new incremental stresses ;

A visualization of the procedure of the hybrid method, is shown in the flow-chart of Figure 3.8.

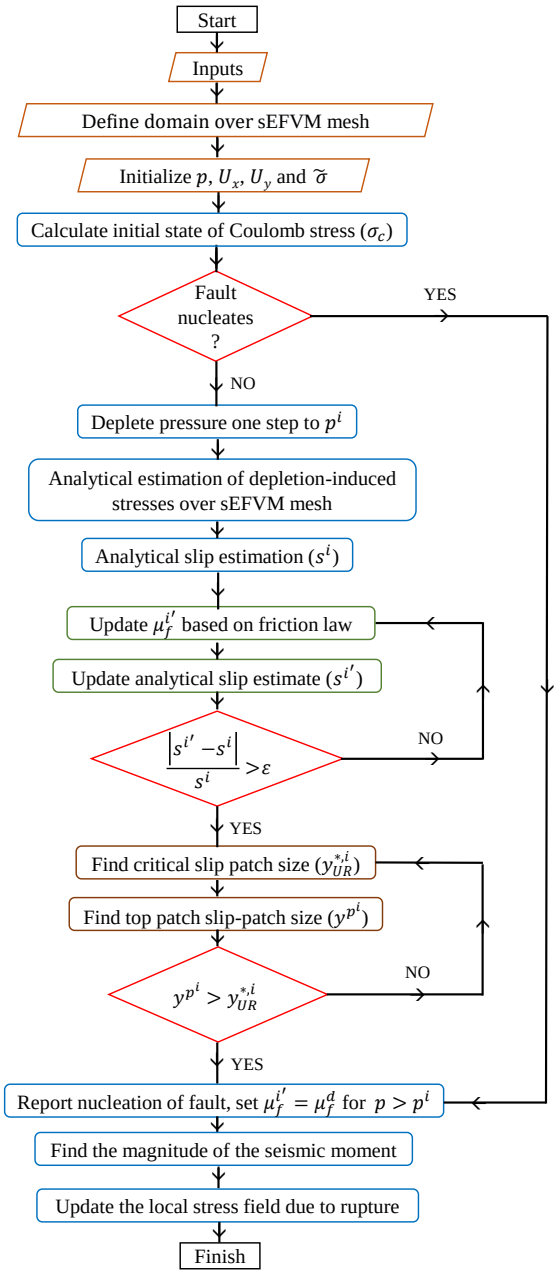

Figure 3.8.: A flow-chart outlining the procedure of the hybrid method for each fault.

4

RESULTS AND DISCUSSIONS

This chapter begins with results from the sEFVM. The examples provide a step-by-step assessment of the method by comparing its solutions to well known test cases.

It is shown that for the cases with continuous shear stress profiles, the sEFVM can accurately simulate stress and the slip profile. However, for cases with discontinuous shear stress profiles, the sEFVM is limited in accuracy. Following this idea, the results of the semi-analytical method are presented. The accuracy of this method is benchmarked with analytical methods. The chapter includes a sensitivity study over some of the most crucial parameters that influence induced seismicity in the Groningen field.

In the last part of this chapter, the results of the hybrid method are presented. The examples in this section demonstrate the capabilities of the hybrid method in simulating post-nucleation rupture and fault-fault interactions in multi-fault setups in a quasi-static fashion..

4.1. THE sEFVM TEST CASES

In this section numerical examples to demonstrate the consistency, monotonicity and applicability of the sEFVM for non-faulted continuum media (i.e. the FVM), and faulted domains are studied. For non-faulted media, the sEFVM reduces to the FVM. For faulted domains, comparative studies are carried out to identify the key strengths of the fully-implicit, fully-coupled and monotone sEFVM compared with the sequentially-coupled, non-iterative and oscillatory EFVM.

4.1.1. CONSISTENCY AND ORDER OF ACCURACY VERIFICATION FOR PURE MECHANICS IN NON-FAULTED/FRACTURED MEDIA

Analytical displacement fields (u_x, u_y) for a 2D homogeneous domain, taken from the literature [66], are given as

Parts of this chapter have been published in the Journal of Computational Physics (2022) [99] and as proceedings of the U.S. Rock Mechanics/Geomechanics Symposium [112].

$$u_x = 10^{-5} \sin\left(\frac{\pi x}{L}\right) \sin\left(\frac{\pi y}{W}\right),$$
$$u_y = 10^{-5} \cos\left(\frac{\pi (L-x)}{L}\right) \sin\left(\frac{\pi y}{W}\right), \tag{4.1}$$

where L and W are model length and width, both taken equal to 1 m here. Moreover, λ and G are, respectively, 10 GPa and 2.5 GPa. Figure 4.1 shows a plot for the displacement fields of Equation 4.1.

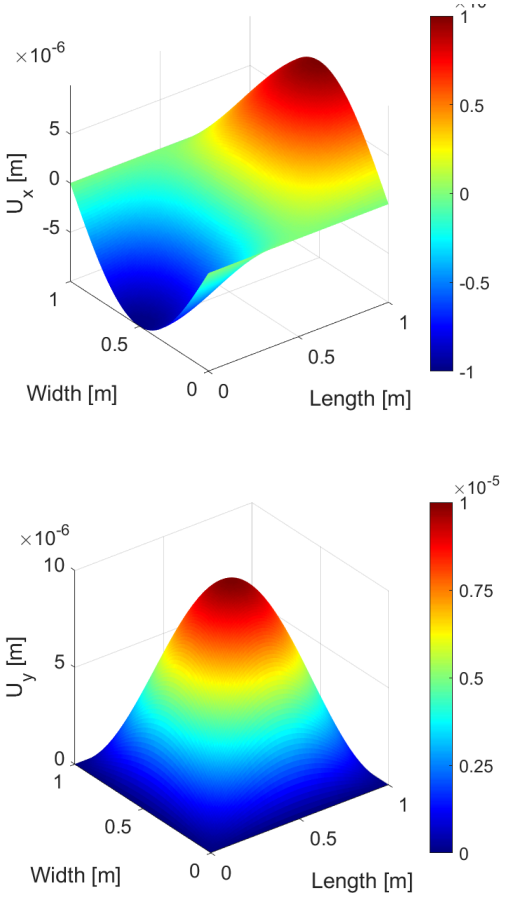

Figure 4.1.: A plot of the horizontal fields of Equation 4.1 over a 1×1 m^2 domain.

Figure 4.2 illustrates the error of the solutions obtained by the FVM, i.e. ϵ, for different mesh sizes Δx. Note that $\Delta x = \Delta y$ at all refinement levels. This test confirms the consistency of the FVM implementation, in the absence of faults. The order of accuracy is confirmed to be 2, consistent with the literature [66].

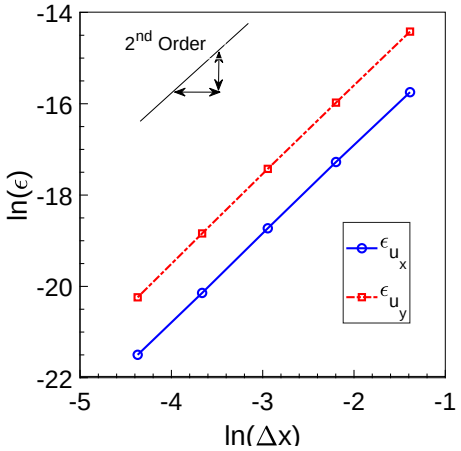

Figure 4.2.: Second order accuracy of the FVM model.

4.1.2. BENCHMARK FOR POROMECHANICS SIMULATIONS FOR NON-FAULTED MEDIA: TERZAGHI TEST CASE

In this test case, complementary to the previously-studied pure mechanics test case, the sEFVM (which again reduces to the FVM in the absence of faults) is validated for poromechanics deformation. A porous medium is compressed from the top and constrained from movement in the normal direction on all other sides. Fluid is allowed to drain from the top, while a no-flow sealing condition applies to all other sides. Figure 4.3 shows an illustration of this test case, which is named after Terzaghi [101].

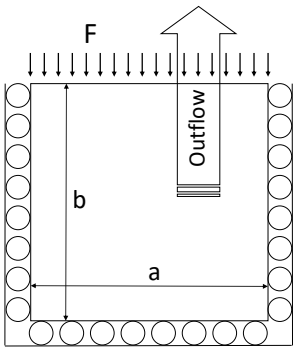

Figure 4.3.: Illustration of Terzaghi poromechanics test case.

An 1×1 m^2 porous medium is considered, for which $E = 1e4$ Pa, $\nu = 0.2$, $k_m/\mu_{fl} = 1e-4$ m^2/Pa.sec, $b = 1$ and $M = 1e100$ are assigned. Moreover, F is 100 Pa and the time-step size of $\Delta t = 0.001$ sec is taken. The initial pressure in the system is set to be 100 Pa. The computational grid consists of 100×100 cells.

Figure 4.4 shows the pressure and displacement profiles only across the depth of the domain, since there exists no change along the horizontal direction. Pressure declines with time as fluid drains out from the top of the porous medium. The vertical displacement is negative, indicating contraction of the compressed system. The contraction increases with time. It is seen that the numerical and analytical results closely replicate each other. More precisely, as an example, the errors of the sEFVM (which again turns to the FVM in the absence of faults and fractures) solution at simulation time 0.9 sec are $\epsilon_{u_y} = 1e-3$ for the vertical displacement and $\epsilon_p = 1.6e-3$ for pressure.

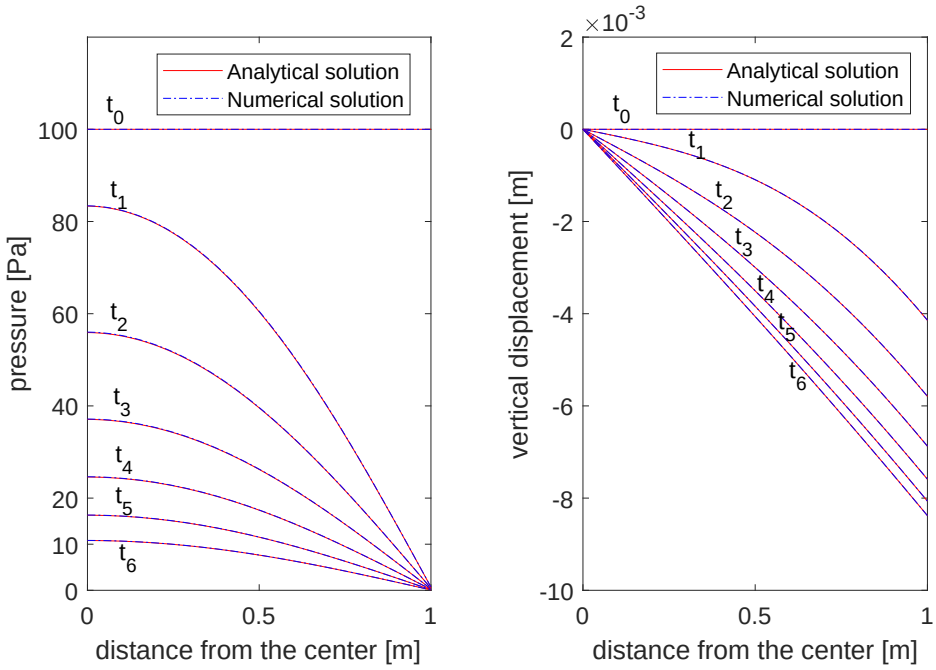

Figure 4.4.: Pressure (left) and displacement (right) profiles for the Terzaghi test case at times t_1 to t_6 with values 0, 0.15, 0.3, 0.45, 0.6, 0.75 and 0.9 sec, respectively.

4.1.3. BENCHMARK FOR POROMECHANICS SIMULATIONS FOR NON-FAULTED MEDIA: MANDEL TEST CASE

In this section the sEFVM, which will be reduced to the FVM due to the absence of faults, is compared with the analytical solution to the Mandel test case. A poroelastic sponge of length $2a$ and width $2b$ is assumed to be open to flow at both its ends. This sponge is compressed from the top and from below with force F. The analytical solutions for pressure and displacement distributions are given in [101].

Due to its symmetric geometry, only a quarter of the domain needs to be modeled as illustrated in Figure 4.5.

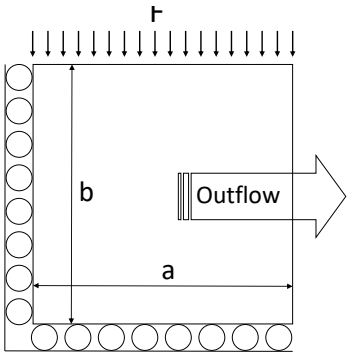

Figure 4.5.: Mandel problem illustration.

Model dimensions, computational grid resolution, and values of E, ν, k_m/μ, b and M are all taken the same as in the Terzaghi test case. Moreover, F is 5 Pa and the time-step size is $\Delta t = 0.1$ sec. The initial pressure in the system is set to be 2.5 Pa.

Figure 4.6 shows the pressure profile along the horizontal center-line of the model at different times. This image shows that the pressure drops as fluid outflows from the right side. At smaller times, i.e. $t_1 = 5$ sec, there is a small pressure buildup above initial conditions near the center of the system. This occurs due to the contraction of the drained edges [101]. Figure 4.6 also confirms that the solution of the FVM numerical model is close to the analytical solution. More specifically, with the chosen grid resolution and time step size, at $t_4 = 30$ sec, the errors are $\epsilon_p = 6.1e-3$ for pressure, $\epsilon_{u_x} = 3.6e-2$ for displacement along the x axis, and $\epsilon_{u_y} = 5e-3$ for displacement along the y axis.

4.1.4. MODELING OF PLANE STRAIN SUBSIDENCE IN A HETEROGENEOUS DEPLETED GAS FIELD

The goal of this section is to compare the numerical FVM poroelastic model with a purely-mechanical FVM model for modeling plane strain subsidence in a heterogeneous setting. It is expected that the solution of the poroelastic model asymptotically reaches the mechanical one at long times.

Surface subsidence is studied in a gas field in the Adriatic basin neighboring Italy. The geometry of Figure 4.7 is conceptualized based on published data [113]. Two methods were used for studying surface subsidence. In the first, the system is modeled dynamically assuming flow inside the porous reservoir. This reservoir is encapsulated by an elastic non-porous medium. In the second approach, the system is entirely impermeable and elastic. For this setup, a force equivalent to the pressure depletion of the dynamic model is applied to the outer boundaries of the assumed reservoir at each time-step.

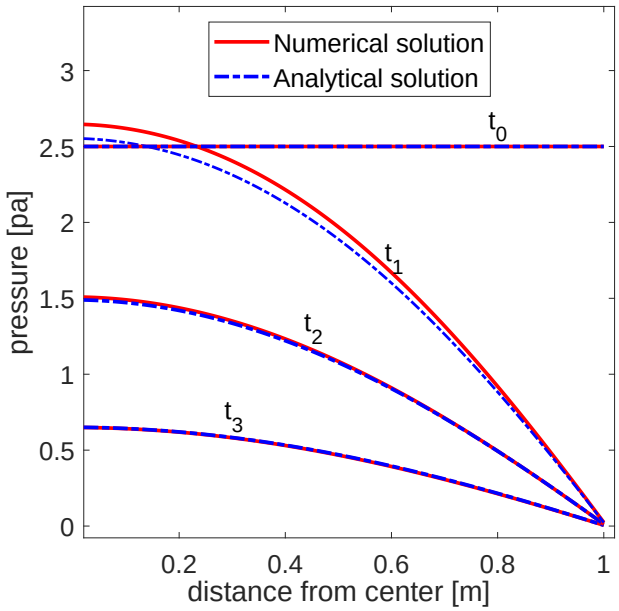

Figure 4.6.: Pressure profiles for the Mandel test case at times t_0 to t_3 with values 0, 5, 15, 30 sec, respectively. The mesh resolution is 100×100 in this example.

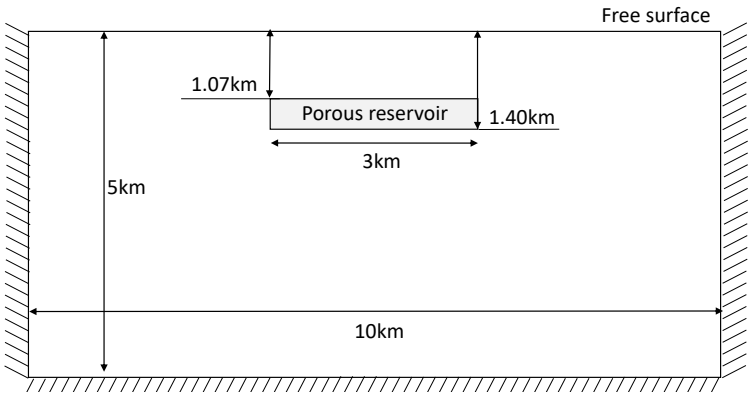

Figure 4.7.: Illustration for modeling plane strain subsidence.

The reservoir is stationary (zero displacements) at all boundaries except for the top free surface. The porous region has no-flow boundaries. The computational grid consists of 50×150 cells, with a finer mesh vertically to capture the thin reservoir. A single gas producer is considered for depletion. The mobility in the horizontal direction is $k_{m,x}/\mu_{fl} = 8e-10$ m^2/Pa.sec.

The vertical to horizontal permeability is $k_{m,y}/k_{m,x} = 0.1$. Value of Poison ratio is $\nu = 0.3$ and $b = 1$. An empirical correlation is used [114] for the Young modulus (E) in this field as given by .

$$E = \frac{(1-2\nu)(1+\nu)}{(1-\nu)c_M}, \tag{4.2}$$

where c_M is the vertical compressibility in $bars^{-1}$ found as a function of depth (z, in meters) according to [114] as

$$c_M = 0.01241 \mid 0.1\ z - 0.12218\ z^{1.0766} \mid^{-1.1342}. \tag{4.3}$$

Values of E and ν are used for determining Lame constants used in Equation (3.10) according to available conversion formulae [101].

The Biot modulus (M, which appears in Equation (2.1)) is calculated as

$$\frac{1}{M} = \frac{\phi}{K_{fl}} + \frac{b-\phi}{K_s}, \tag{4.4}$$

where K_{fl} and K_s are fluid and solid moduli taken as 0.02 and 50 and GPa, respectively [115]. The porosity, ϕ, is calculated as a function of depth (z, in meters) as [116]

$$\phi = -0.005\ log(z) + 0.3. \tag{4.5}$$

Figure 4.8 shows the evolution of surface subsidence for the studied problem. The static and dynamic results are plotted at various simulation times. Simulation time is reported as a multiples of dimensionless time t_c, which is calculated according to Equation (3.28). It can be seen that both methods converge to the same solution at late times. This is an expected outcome. Errors are quantified according to Equation (3.27). At simulation time $t = 500t_c$, the errors are $\epsilon_{u_y} = 1.26e-2$ and $\epsilon_{u_x} = 1.53e-2$ for displacement fields. The error for surface subsidence is $5.0e-3$.

4.1.5. FAULTED RESERVOIR IN AN INFINITE DOMAIN

A finite reservoir is assumed in an infinite domain. A vertical fault with an initial offset is present in the middle of the reservoir. The fault is fully permeable but does not transmit fluid pressure above the top or below the bottom of the reservoir. The setup is shown in Figure 4.9. Analytical solutions for production/injection-induced displacements, stresses and strains for this system are given by Jansen et. al. (2019) [80]. Here, the sEFVM predictions are compared with the analytical solutions for the shear stress along the fault.

Elastic parameters are G = 6.5 GPa and ν = 0.15. The fault surfaces are frictionless. Values of a and b in Figure 4.9 are 75 m and 150 m, respectively. In the analytical solution, the reservoir stretches throughout the entire horizontal extent of the system. To approximate such infinite boundaries, the external medium in the numerical set up is assumed 10 times larger than the reservoir thickness (i.e. 2250 m × 2250 m). Roller boundary conditions are considered on all external boundaries.

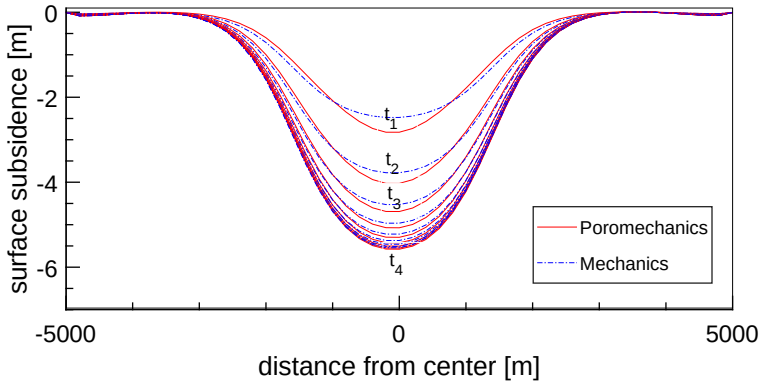

Figure 4.8.: Comparison of evolution of surface subsidence in a depleting gas field as predicted using static and poroelastic FVM models from t_1 to t_4 corresponding to $50t_c$, $100t_c$, $150t_c$ and $500t_c$.

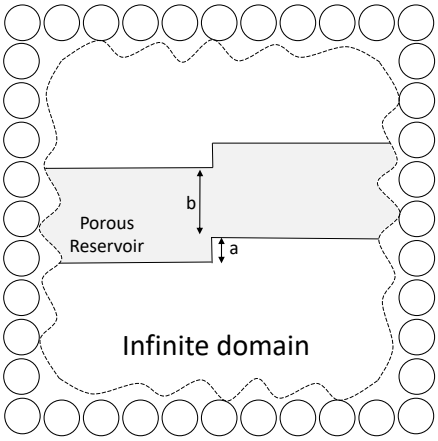

Figure 4.9.: Schematic of a faulted reservoir in an infinite domain.

The reservoir boundaries are impermeable. The reservoir is depleted via a single production well placed centrally in the reservoir. This well produces at a constant draw down pressure of ΔP = -25 MPa.

The computational grid consists of 200×200 cells. The numerical results were obtained by considering different orders for the time-step (1 minute, 1 hour and 1 day).

The shear stress is plotted along the depth of the reservoir at the location of the fault. Figure 4.10 shows the results of the dynamic FVM model at various time-steps and the analytical solution based on equations in [80]. The stress profile shows 2 minima and 2 maxima. These extrema correspond to the 4 edges of the displaced reservoir sections.

The numerical solution approaches the analytical solution at full depletion, which is seen after approximately 6 days, although the finite grid resolution results in smoothed extrema instead of the peaks of infinite magnitude as observed in the analytical solution.

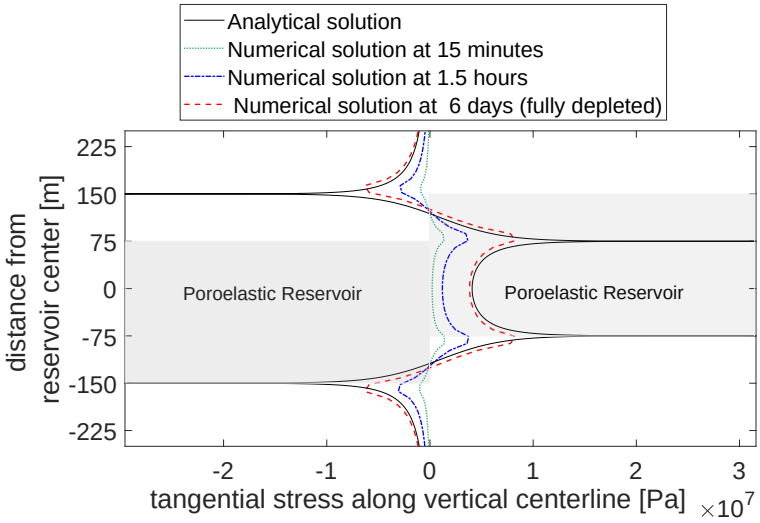

Figure 4.10.: Shear stress profile across the vertical center-line in an infinite faulted reservoir

4.1.6. ELASTIC FAULTED MODEL

The analytical solution for the slip profile in the faulted, unbounded and elastic block of Figure 4.11 is found according to the literature as [117]

$$s\ (L_x)\ =\ \frac{2(1-\nu^2)\ \tau_c}{E}\sqrt{L_f^2-(x-L_f)^2}, \tag{4.6}$$

where L_x is the location along the fault and L_f is the fault length. θ is the friction angle defined as

$$|\ \tau\ | = -\tan\theta\ \sigma_n, \tag{4.7}$$

and τ_c is defined as

$$\tau_c = \sigma \sin\alpha\ \Big(\cos\alpha - \sin\alpha\ \tan\theta\Big), \tag{4.8}$$

where α is the angle of the fault with the negative direction of the horizontal axis [117].

A 100×100 m^2 cube is considered. There is a 10 meter fault at the center of the block with $\theta = 20$ degrees.

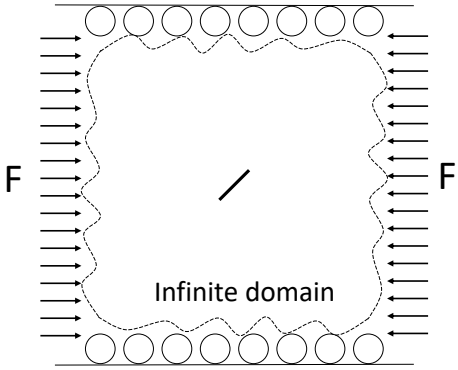

Figure 4.11.: Illustration for the infinite, elastic faulted system under compression

Force F compresses the horizontal sides of the block. Top and bottom sides are constrained from normal displacement to simulate an infinite domain. Values of $E = 7e10$ Pa, $\nu = 0.2$ and $\alpha = 30$ degrees are assigned to the model. The computational grid consists of 100×100 cells. The slip profiles from the analytical solution and the EFVM are shown in Figure 4.12 for three different values of F of 50, 100 and 200 MPa. These results show good agreement between EFVM and analytical solutions. The slip increases with increased applied force.

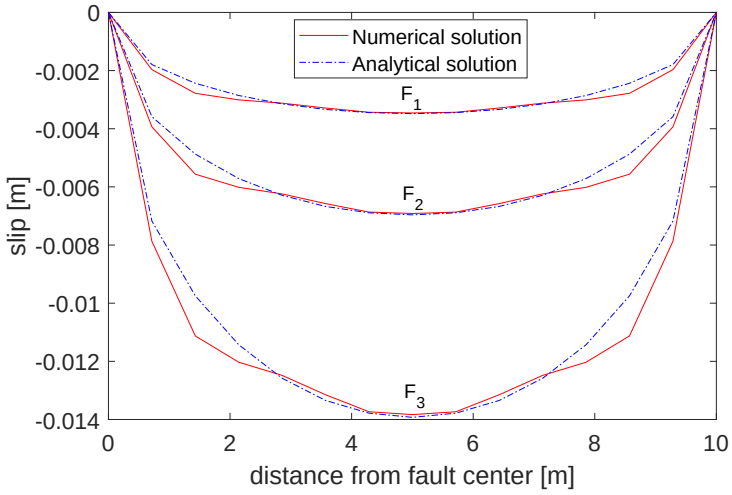

Figure 4.12.: Comparison of analytical solutions with numerical solutions of EFVM for the slip profile in a infinite faulted domain under compression loads of F_1 to F_3 equal to 50, 100 and 200 MPa.

4.1.7. TEST CASE WITH OSCILLATORY BEHAVIOR AND THE USE OF THE SEFVM

The EFVM can produce non-smooth profiles for the slip and stress fields. As an example, a 1×1 m^2 elastic domain is considered.

The top and the bottom surfaces are subject to a Dirichlet displacement vector (u_x, u_y) of $(0,0)$ and $(0.05, 0.005)$ meters, respectively. The East and West boundaries are subject to free stress. A fault is defined with a length of 0.4 m, located centrally, having an angle of α towards the horizontal axis. Lame parameters are both chosen equal to 1 Pa. The friction coefficient is set to be 0.85. The setup is shown in Figure 4.13.

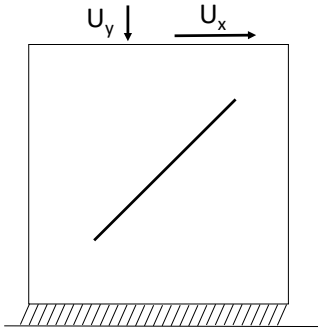

Figure 4.13.: Illustration for faulted test case with surface displacements.

The slip profile for the case of a horizontal fault (i.e., $\theta = 0$) is shown in Figure 4.14. For this case, the slip profile is smooth and in good agreement with results of the Porepy simulator [118]. The order of accuracy for slip is determined by altering the computational grid from 10×10 to 160×160. The error is calculated using Equation (3.27) with respect to the most refined mesh (i.e., 160×160) and plotted in Figure 4.14. This figure shows that the slip profile converges linearly to the solution.

However, the smoothness of the slip profile is not always guaranteed. The same setup is modeled by rotating the fault to hold the angle of $\alpha = 18$ degrees. The slip profile is shown in Figure 4.15. For this example, the slip profile takes a saddle form, and the fully-implicit EFVM results are non-smooth. The EFVM results, even though being non-smooth, are fully converged for the state of slip-stick at each fault node. It is observed in Figure 4.15 that the magnitude of oscillations decays as the mesh gets finer, and that the slip function remains convergent in spite of oscillatory behaviour.

However, oscillations can pose a significant challenge as the stress fields become also non-smooth. The stress fields are used to determine slip-stick conditions of the fault. When the fault is critically stressed, the oscillations can potentially result in the incorrect determination of slipping nodes.

For this reason, it is crucial to systematically resolve the oscillations within stress fields. To resolve this challenge, and guarantee smoothness of the results, a smoothing procedure is included in the EFVM and the method is referred to as the sEFVM.

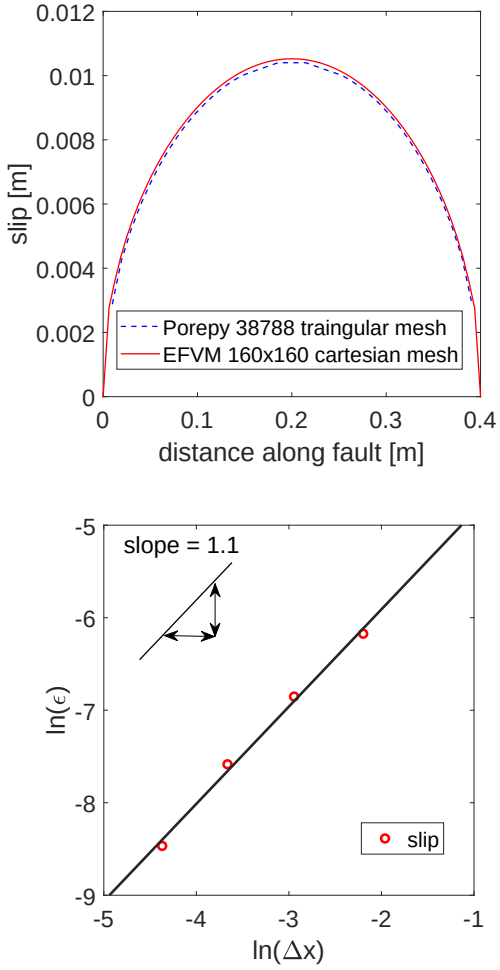

Figure 4.14.: EFVM slip profile (top) and the order of accuracy of slip (bottom) for a block with surface displacement and a horizontal fault.

.

A polynomial fit to the oscillating curve is used to capture the behavior without oscillations. It is found that this fitted polynomial is in close agreement with the expected results. For the studied example, this is shown in Figure 4.16 for stress and slip. The fit is in good agreement with results of Porepy and the solution of the EFVM on a finer mesh.

The smooth solution presented in Figure 4.16 for to the stress and slip profiles are

$$\tau(L_x) = c_1 L_x^2 + c_2 L_x + c_3, \tag{4.9a}$$

$$s(L_x) = d_1 L_x^4 + d_2 L_x^3 + d_3 L_x^2 + d_4 L_x + d_5, \tag{4.9b}$$

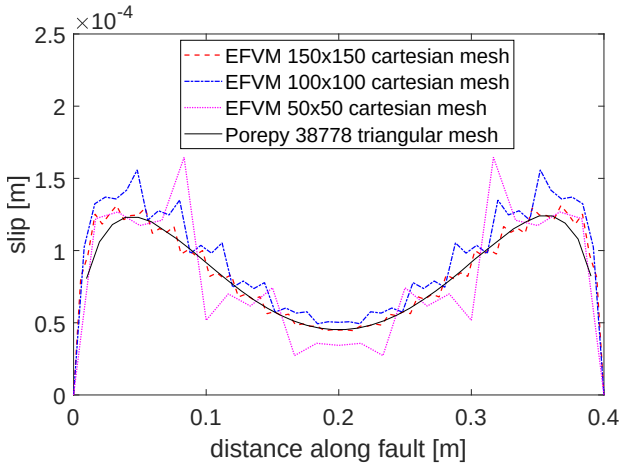

Figure 4.15.: Convergent oscillatory solution of EFVM for the slip profile for a fault inclined at 18 degrees.

where L_x is the distance from the beginning of the fault in meters (i.e., the tip with minimum x and y values). Values of c_1 to c_3 are found as -0.1508 Pa/m^2, 0.06031 Pa/m and 0.02948 Pa, respectively. Values of d_1 to d_5 are found as -0.1821 m^{-3}, 0.1457 m^{-2}, -0.03589 m^{-1}, 0.002701 and $6.003e-5$ m, respectively. The norm of residuals for stress and slip are $3.8e-3$ Pa and $1.1e-4$ m, respectively. The small norm values indicate a good fit.

In later work on the sEFVM, a better smoothing procedure was adapted. The smoothing spline fit was used to capture a smoothed stress and slip profile. A smoothing spline is characterized as a series of piece-wise polynomials and serves as a fitting function to the oscillatory stress and slip data. The spline finds the best fit (S_f) to the data (x_i versus y_i) by finding the minimum value to function F_{min} defined as

$$F_{\text{min}} = p\sum_i (y_i - S_f(x_i))^2 + (1-p)\int \left(\frac{d^2 S_f}{dx^2}\right)^2 dx. \tag{4.10}$$

Here, p is a smoothing parameter with a value between 0 and 1. If $p = 1$, the fit is a cubic spline interpolant and if $p = 0$, the fit is a least-squares straight line fit. The built-in MATLAB function "fit" is used to implement this smoothing [119].

Note that the EFVM oscillations are due to the misaligned faults and the embedded grid cells. This is because the stress profile over the fault is calculated based on displacement values in each fault-containing grid cell.

For most problems, the EFVM results are found to be smooth. But when oscillations do arise, the proposed smoothing procedure leading to the sEFVM guarantees monotone solutions for all faults. This is crucial for practical cases; which typically involve challenging fault geometries and orientations.

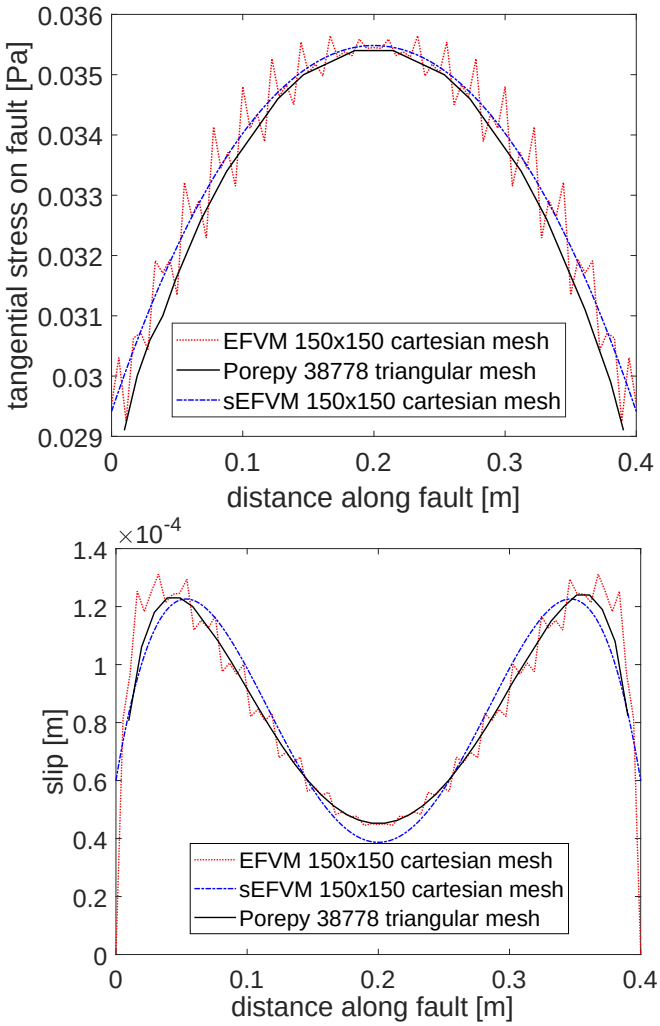

Figure 4.16.: Post-processing of the stress (top) and slip profile (bottom) in the sEFVM for the example of a fault inclined at 18 degrees.

.

Another important advancement of the proposed fully-coupled fully-implicit sEFVM is that the state of slip-stick is found implicitly based on the updated state of the stress. This is elaborated in Algorithm 1.

This figure shows severe errors in the fault slip predictions, if this important feature is neglected, as in the literature [64, 65], where the stress from the previous time step is used to indicate the slip-stick state of fault nodes.

Figure 4.17 illustrates this important aspect, by presenting the slip profile if no iterations are employed to indicate the slip-stick state.

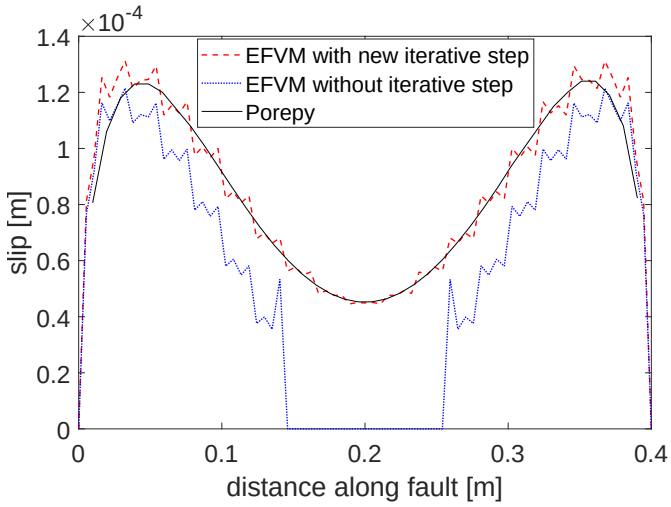

Figure 4.17.: Demonstration of the role of the new iterative step in the sEFVM for the example of a fault inclined at 18 degrees in the block with surface displacement.

4.1.8. HEAVILY-FAULTED POROELASTIC MODEL

A conceptual model is considered with dimensions of 30×50 km^2. Values of $\nu = 0.2$, $b = 1$ and $\phi = 0.2$ are assigned to the model. The system is heavily-faulted with 29 impermeable faults, some of which are located very close to each other. This is shown in Figure 4.18.

The model consists of a poroelastic saturated reservoir surrounded by an impermeable elastic external medium. A production well is placed centrally in the porous reservoir region. The initial reservoir pressure and production well bottom-hole pressures are 150 MPa and 100 MPa, respectively. Mobility is $1e-6$ m^2/Pa.sec. The friction coefficient for all faults is set to be 0.6. The computational grid consists of 128×128 cells, and the time step size is 1.5 hours.

A force per length of 1 kPa/m is applied at the top boundary. The bottom boundary is stationary. Horizontal boundaries are constrained from normal displacement as shown in the illustration in Figure 4.18.

Figure 4.19 shows the displacement fields for the test case after 15 hours. Both horizontal and vertical displacement fields show that the highest magnitude of deformation occurs inside and in the vicinity of the porous reservoir domain. The effect of the heterogeneous E field is clearly seen in the vertical displacement profile, resulting in heterogeneous displacement patterns.

Another representation for stress is the von Mises stress (σ_{VM}). This parameter aids with geomechanical interpretation by considering the overall stress state rather than focusing solely on individual stresses. The von Mises stress combines the principal stresses to calculate the equivalent von Mises stress [120].

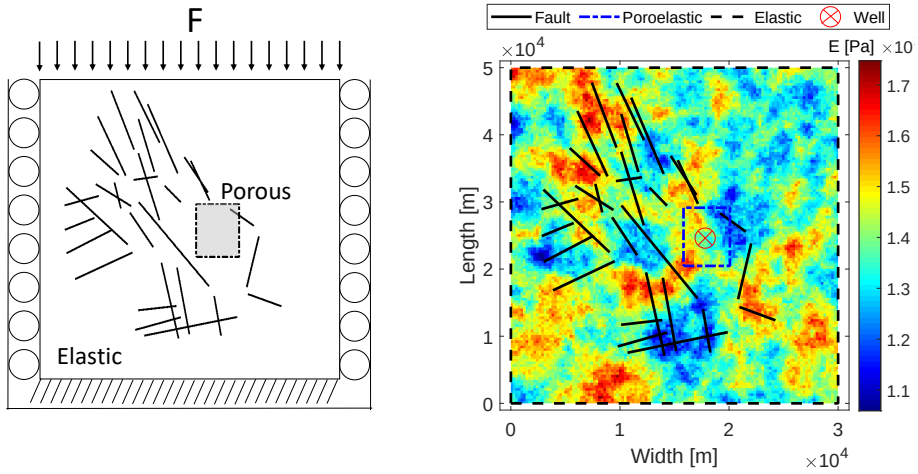

Figure 4.18.: Schematic (left) and heterogeneous map for the Young modulus (right) of a heavily faulted poroelastic model.

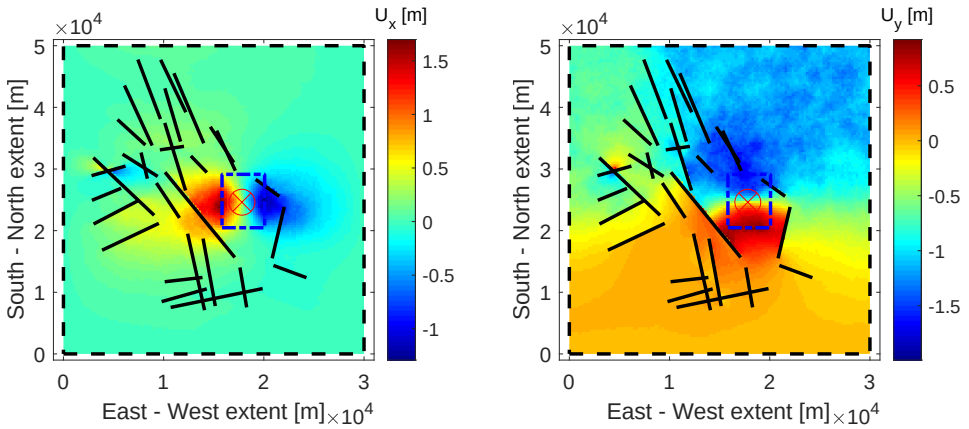

Figure 4.19.: Horizontal (left) and vertical displacement fields (right) following depletion of the reservoir in a heavily faulted poroelastic model.

The von Mises stress and the pressure map for the current example are shown in Figure 4.20. According to the von Mises stress map, the maximum stress is observed inside the poroelastic region.

The pressure map reflects the depletion inside the porous region. One fault which intersects with the reservoir at the top right boundary has influenced depletion in that region. It is worth mentioning that in this test case, no smoothing was required as the EFVM results were non-oscillatory.

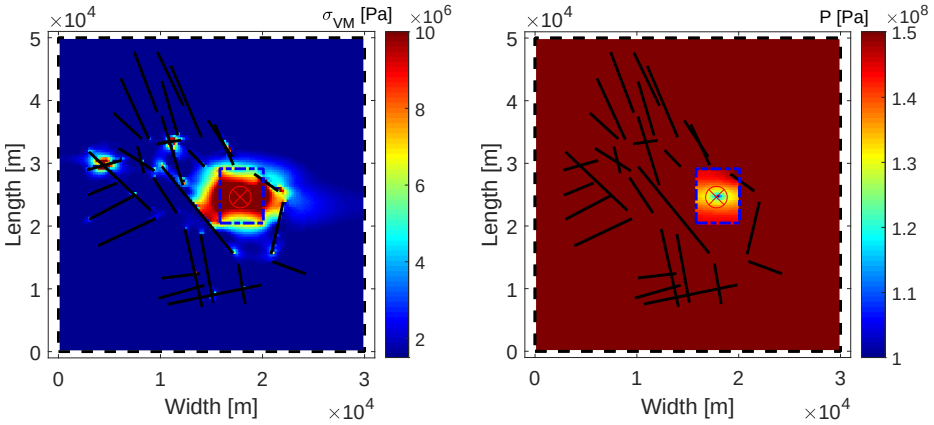

Figure 4.20.: von Mises stress (left) and pressure map (right) in a heavily faulted poroelastic model.

.

4.1.9. TEST CASES WITH DISCONTINUOUS SHEAR STRESS PROFILES AND THE SEFVM ACCURACY LIMITATION

In this section, the test case shown in Figure 2.4 is considered. The model is built up from the simplest possible configuration: no fault and no offset. Then, the configuration is extended to include a fault, and later to include a fault and an offset.

The results from the sEFVM are compared to analytical solutions that are presented in Chapter 2. Results from another numerical method developed by Novikov et. al. (2022) are also used in this comparison [121]. The latter uses a finite-volume collocated scheme with an unstructured grid and a conformal mesh to the fault for modeling the setup.

The base-case properties considered in this section are shown in Table 4.1. Based on the values in Table 4.1, the vertical force affecting the top surface of the reservoir (i.e. $y = 2250$ m) and bottom (i.e. $y = -2250$ m) is calculated according to Equation 2.8 as

$$f_{v,\text{top}} = \sigma^0_{yy}(2250) = -29.50 \times 10^6 \,\text{Pa}, \tag{4.11a}$$

$$f_{v,\text{bot}} = -\sigma^0_{yy}(-2250) = 135.7 \times 10^6 \,\text{Pa}. \tag{4.11b}$$

A negative $f_{v,top}$ implies that this load acts in the negative y direction (i.e. downward) and vice versa.

This load is used for finding the horizontal load, f_h, at the top and bottom of the domain according to Equation 2.9 as

$$f_{h,\text{top}}(2250) = 20.37 \times 10^6 \,\text{Pa}, \tag{4.12a}$$

$$f_{h,\text{bot}}(-2250) = 93.73 \times 10^6 \,\text{Pa}, \tag{4.12b}$$

Table 4.1.: Base-case setup data for the simulation of depletion-induced fault reactivation in reservoirs with an offset.

Symbol	Property	Value	SI units
h_1	See Figure 2.4	112.5 or 75	m
h_2	"	112.5 or 150	m
D_0	Depth at reservoir center ($y = 0$)	3500	m
g	Acceleration of gravity	9.81	m/s^2
G	Shear modulus	6500	MPa
H	Height of simulation domain	4500	m
K^0	Initial horizontal to vertical stress ratio	0.5	–
p	Incremental reservoir pressure	−25	MPa
p_0^0	Initial reservoir pressure at reservoir center	35	MPa
W	Width of simulation domain	4500	m
α	Biot coefficient	0.9	–
β	Effective stress coefficient for fault friction	0.9	–
θ	Dip angle	90 or 70	degree
κ	Cohesion	0	MPa
μ	friction coefficient	0.52	–
ν	Poisson's coefficient	0.15	–
ρ_{fl}	Fluid density	1020	kg/m^3
ρ_s	Solid density	2650	kg/m^3
ϕ	Porosity	0.15	–

The initial stresses corresponding to the above loads are calculated analytically based on Equation 2.14 as

$$\sigma_{xx}^0(y) = -57.05 \times 10^6 + 16.30 \times 10^3 \times y\,\text{Pa}, \tag{4.13a}$$

$$\sigma_{yy}^0(y) = -82.60 \times 10^6 + 23.60 \times 10^3 \times y\,\text{Pa}, \tag{4.13b}$$

$$\sigma_{xy}^0(y) = 0\,\text{Pa}. \tag{4.13c}$$

The initial pressure field is calculated analytically using Equation 2.10 as

$$p^0(y) = 35.00 \times 10^6 - 10.06 \times 10^3 \cdot y\,\text{Pa}. \tag{4.14}$$

The map of the initial pressure, and post-depletion pressure calculated using the sEFVM is shown in Figure 4.21. In the depleted pressure map, the darker region in the center of the model outlines the reservoir.

The application of the loads $f_{v,top}$, $f_{v,bot}$ and $\pm f_h$ to the boundaries results in initial vertical and horizontal displacement fields $u_y^0(x, y)$ and $u_x^0(x, y)$.

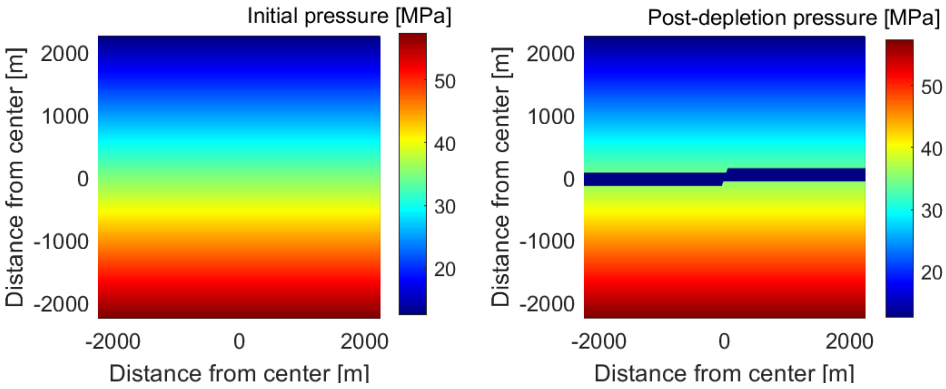

Figure 4.21.: Pressure map at initial conditions (left) and after 25 MPa depletion (right) in a model with an offset. Calculations are performed on a computational domain consisting of 300×300 cells.

These displacements are calculated using 2.16. Accordingly, the vertical displacement at the top of the domain is

$$u_y^0(+2250) = -13.66\,\text{m}. \tag{4.15}$$

The initial horizontal displacements at the top left and bottom left of the simulation domain are

$$u_x^0(-2250, +2250) = 0.87\,\text{m}, \tag{4.16a}$$
$$u_x^0(-2250, -2250) = 3.98\,\text{m}. \tag{4.16b}$$

Identical displacements, but in opposite direction exist at the right boundary. The true displacement field will show small deviations from these approximate values because of contraction effects due to non-isotropic compression of the simulation domain as a result of the nonuniform initial distributed loads.

These displacements are comparable to that obtained from the sEFVM as shown in Table 4.2. When using the sEFVM, the vertical displacement (i.e. 13.66 m) is obtained by summing the magnitude of the vertical displacement profiles at the top (i.e. $y = -2250$ m) and at the bottom (i.e. $y = 2250$ m) of the domain as

$$u_y^0 = |u_{y,top}^0| + |u_{y,bot}^0| \tag{4.17}$$

Figure 4.22 shows the initial displacement fields calculated using sEFVM.

Table 4.2.: Comparison of the results of the sEFVM and the analytical solution for the estimation of initial displacements.

Method	Cells in x-y	u_y^0 [m]	$u_{x,top}^0$ [m]	$u_{x,bot}^0$ [m]
Analytical	-	-13.66	0.87	3.98
sEFVM	81 x 81	-13.51	0.91	3.99
sEFVM	121 x 121	-13.58	0.90	3.99
sEFVM	201 x 201	-13.63	0.89	3.99
sEFVM	300 x 300	-13.66	0.87	3.98

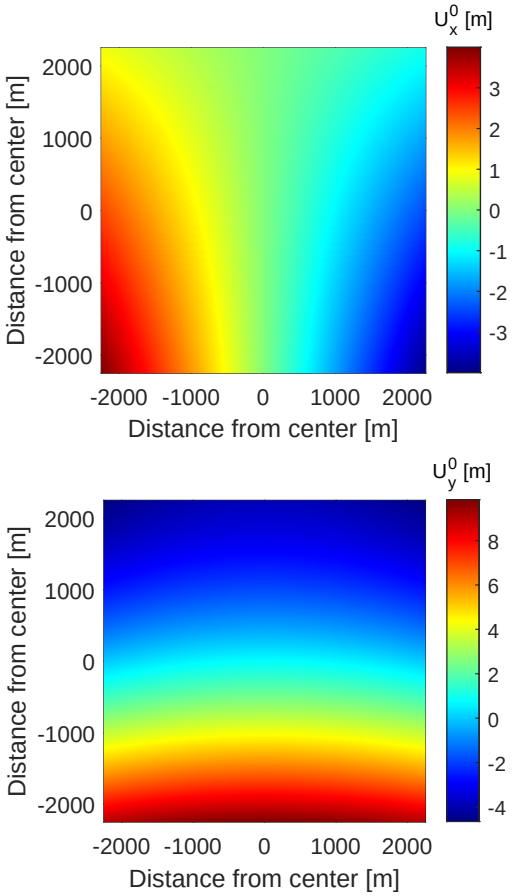

Figure 4.22.: Displacement field in the horizontal direction (top) and vertical direction (bottom) calculated using the sEFVM over a domain consisting of 300×300 cells.

.

Assuming there can be a fault in the system, the stresses are calculated along an angle of 70 degrees with the horizontal direction. The normal and shear stresses along this direction are analytically calculated according to Equation 2.15.

Figure 4.23 shows the values calculated using the sEFVM, the collocated FVM (also known as DARTS [122]) and the analytical approach.

Both numerical codes produce a fully satisfactory results. The results from DARTS for the shear stresses display small irregularities resulting from the use of an unstructured grid [112].

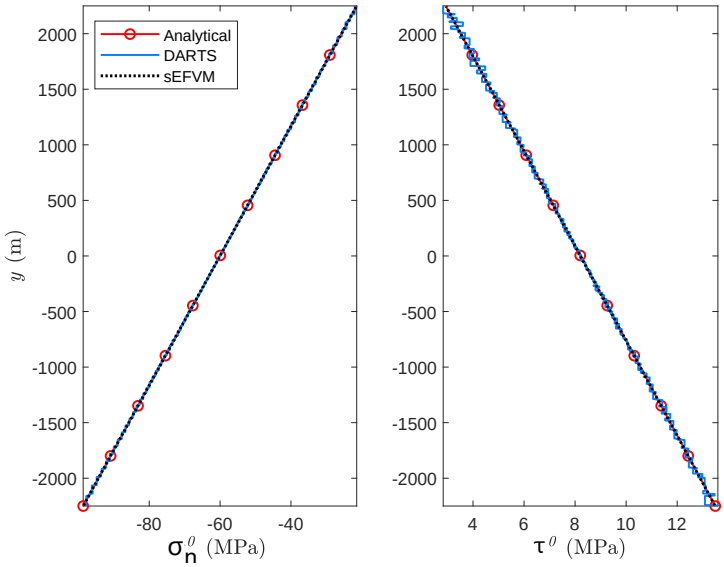

Figure 4.23.: Initial normal stresses (left) and initial shear stresses (right) along a line through the center of the reservoir at an angle of 70 degree with the horizontal.

The reservoir compaction following a depletion of 25 MPa is calculated using Equation 2.19 as

$$\Delta h = -0.32\,\text{m}. \tag{4.18}$$

The compaction can be calculated numerically as well, by comparing the vertical displacement before depletion to that after depletion.

The compaction is simulated using the sEFVM on a computational domain consisting of 135 × 135 cell. The results of this simulation show that the initial vertical displacement is $u_y^0 = 13.59$ m. After 25 MPa depletion, the vertical displacement is $u_y^{\Delta p} = 13.91$ m. The difference between the two is 0.32 m, equivalent to the analytical derivation in Equation 4.18.

The incremental horizontal strain ϵ_{xx} remains equal to zero, because of the infinite horizontal extent of the reservoir. This is also true for the numerical results.

For example, using the sEFVM with 135 × 135 cells, the change in horizontal strain is close to the machine accuracy range (i.e., 10^{-15}).

The incremental horizontal effective stress is found using 2.23 as $\sigma'_{xx} = -3.97$ MPa. From this, the incremental total horizontal stress is calculated from Equation 2.24 as $\sigma_{xx} = 18.53$ MPa.

For the simple case of a reservoir without faults no incremental shear stresses σ_{xy} develop, and because there were no initial shear stresses σ^0_{xy} it follows that also the combined shear stresses vanish. However, for the line at an angle of 70 degrees that was considered earlier in Figure 4.23, the incremental horizontal stresses σ_{xx} have an effect on both the incremental normal and shear stresses and therefore also on the combined normal and shear stresses (i.e. Σ_n and T from Equation 2.26).

Figure 4.24 shows the total stresses along the inclined line for the two simulation codes and the analytical solution. Both codes produce a fully satisfactory match.

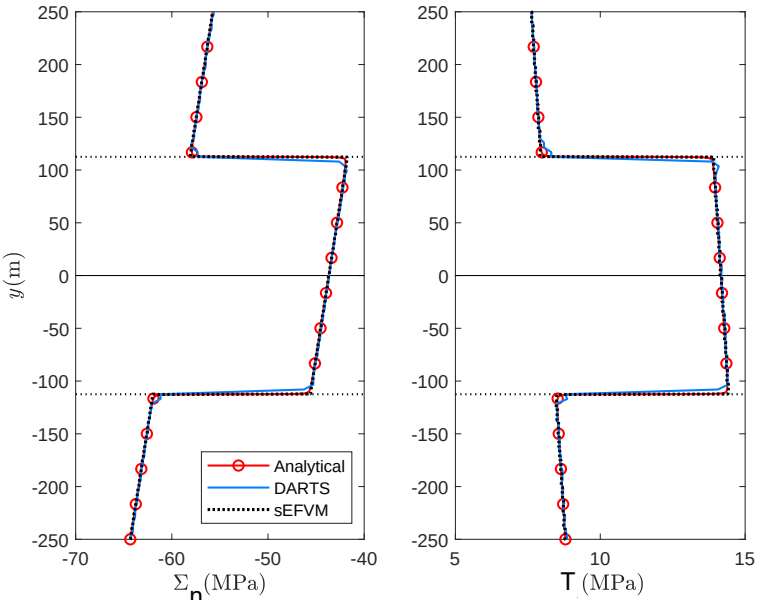

Figure 4.24.: Combined normal stresses (left) and combined shear stresses (right) along a line through the center of the reservoir at an angle of 70 degree with horizontal.

The same reservoir is considered but with a vertical frictionless fault (i.e. $\theta = 90$ degrees and $\mu_f = 0$) at the centre. This fault introduces a throw as in the schematic of Figure 2.4. For this setup, the pre-slip coulomb stress and slip is calculated using Equation 3.38 and 3.2.2, respectively. The constant C in Equation 3.30 based on the parameters of Table 4.1 for a depletion of 25 MPa is equal to −2.95 MPa. The value of A from Equation 3.40 is 1217.1 MPa.

Figure 4.25 (right) displays this slip distribution over the height of the reservoir, and Figure 4.25 (left) displays the pre-slip Coulomb stress profile over the vertical frictionless fault.

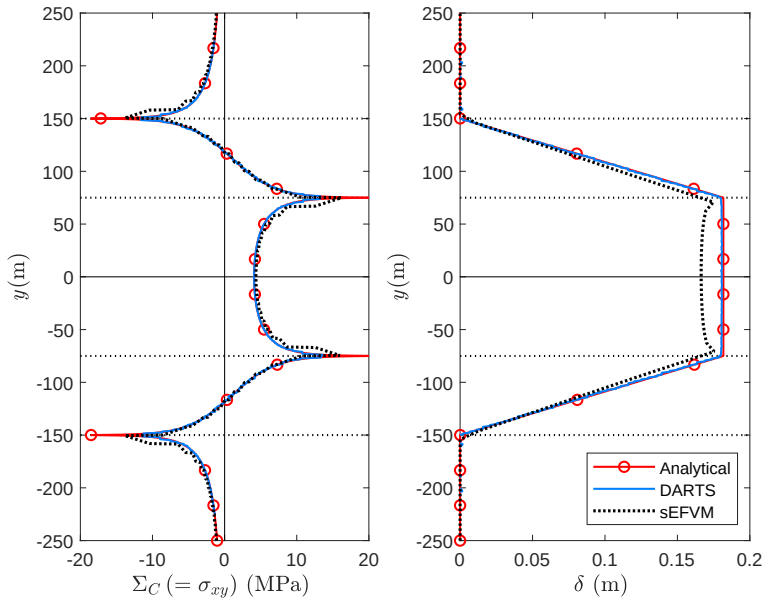

Figure 4.25.: Pre-slip Coulomb stresses Σ_C in a frictionless vertical fault with offset (left) and the resulting slip δ (right).

The correspondence between the DARTS results and the semi-analytical results is excellent. The sEFVM results are slightly in error. This is because the sEFVM calculates the slip by enriching the displacement field with one additional degree of freedom per matrix grid node. This is as opposed to other embedded methods such as the XFEM, where in 2D each node that is enriched with the jump function is given 2 degrees of freedom. For fault tip enrichment, there are 4 extra degrees of freedom. This means the sEFVM is much faster in terms of CPU time, but the predictions are expected to be less accurate [63, 68].

Another setup is considered where the fault is at 70 degrees with the horizontal and has a constant friction coefficient. Figure 4.26 (left) displays the pre-slip shear stresses T and the slip threshold (Equation 2.32) for an incremental pressure $p = -25$ MPa, and Figure 4.26 (right) shows the corresponding pre-slip Coulomb stresses.

The sEFVM results in Figure 4.26 show a deviation. For the cases of depleted reservoirs with offset such as the case studied in the aforementioned figure, the sEFVM accuracy is off by about 20%. In such cases, the infinite peaks in the stress profile are a problem for the smoothed embedded method. Efforts were made to understand the cause of this error and address it. These efforts are discussed next.

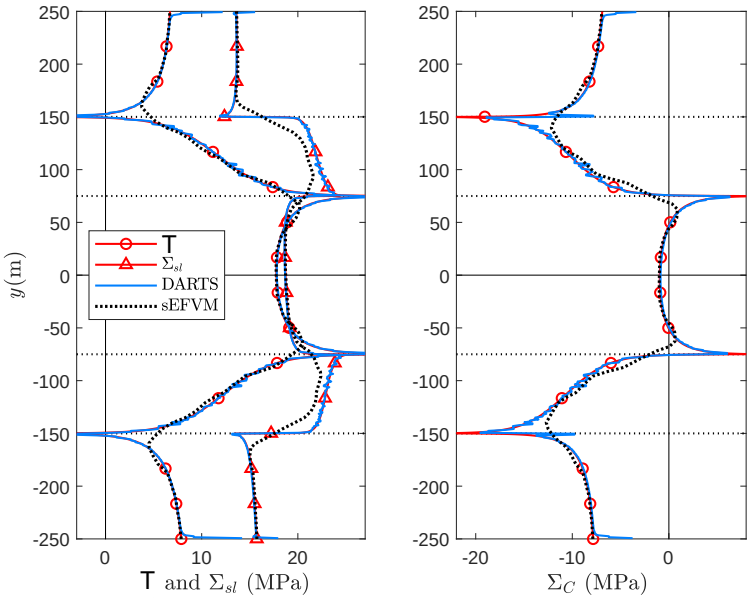

Figure 4.26.: Pre-slip shear stresses T and slip threshold Σ_{sl} in an inclined fault with offset and constant friction (left) and the corresponding pre-slip Coulomb stresses Σ_C (right). Simulation domain width $W = 4500$ m.

EFFORTS TO IMPROVE THE ACCURACY OF THE SEFVM IN SIMULATION OF FAULTED RESERVOIRS WITH OFFSET

Following the issues with the accuracy of the sEFVM for test cases similar to that of Figure 4.26, efforts were made to minimize errors. Several approaches were taken:

- Grid refinement was initially tried. One obstacle to refining the grid was longer run-times. To address this limitation, the code was optimized. This was done by replacing "for" and "while" loops used for finding the coefficients of matrices in Equation 3.26 with vectorized equivalents. This reduced the run-times considerably, allowing for further refinement of the grid. For example, for a 500×500 grid, the size of the matrix of coefficients (from Equation 3.26) was 750,000×750,000. The initial run-time for the sEFVM to solve this system was 8 hours. Following vectorization, this time was reduced to 4 minutes.

- The peaks in the Coulomb stress profile shown in Figure 4.25 occur exactly at the offset points at 75 and 150 meters below and above the center line of the reservoir. The Cartesian mesh of the sEFVM is defined so that the boundaries of the pressure control volume coincide with these depths. If the number of cells in the vertical direction is divisible by the offset location depths (i.e. 75

and 150 meters in this example), the depths corresponding to the stress peaks will be captured exactly. Otherwise, there is an error in capturing the geometry of the analytical problem. Given that the peaks exist precisely at offset depths, this can introduce a visible miss-match between the results of the analytical solution and the sEFVM.

- Further on the subject of capturing the geometry, is the importance of the location of the fault with respect to the matrix grid. In the embedded scheme of the sEFVM, the fault cannot pass through a displacement node exactly. This is because the appended basis functions (plotted in Figure 3.2) require the existence of two sides within each grid block, to define the discontinuity. This is the foundation of the sEFVM and a limitation to it. In the sEFVM algorithm, for instances where such intersection occurs, the fault is moved infinitesimally to one side of the displacement node. Assuming the case of a vertical fault, this indicates the fault cannot be exactly located centrally in the reservoir. This is shown in Figure 4.27. This miss-match exists inherently in the case of the vertical fault where the Coulomb stress profile was earlier shown in Figure 4.25.

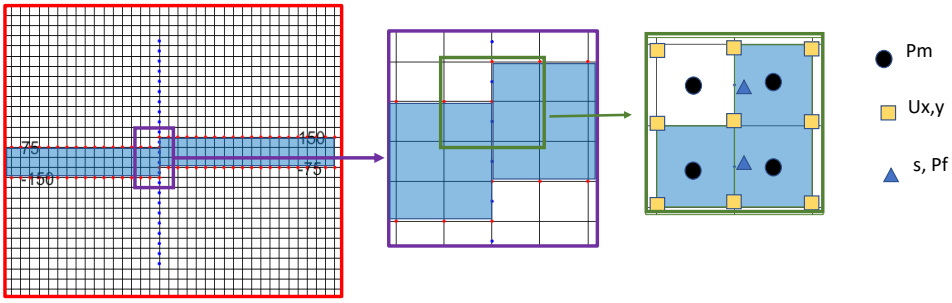

Figure 4.27.: Moving the fault slightly to one side from the center line to avoid intersection with the sEFVM matrix displacement nodes.

- Further grid refinement was addressed by introducing local grid refinement. Initially, a simple one-step grid refinement was implemented. This implementation is shown in Figure 4.27. Here, the grid size was reduced from an initial size $\Delta^1_{x,y}$ to size $\Delta^2_{x,y}$ in one step. The results showed that the sudden refinement created kinks in the stress profiles in between the larger and smaller grids. Another method was chosen whereby refinement was implemented in a step-wise manner. The size of the grids would lessen with size in an order defined by a geometric series as shown by Equation 4.19.

$$\Delta^n_{x,y} = \frac{\Delta^i_{x,y}(1-x^n)}{1-x}, \tag{4.19}$$

where $\Delta^i_{x,y}$ is the size of the unrefined grid in x or y direction, n is the number cells intended for refinement and x is the common ratio between consecutive entries.

The value of x was determined based on the range of cells intended for refinement and the depths that were of interest.

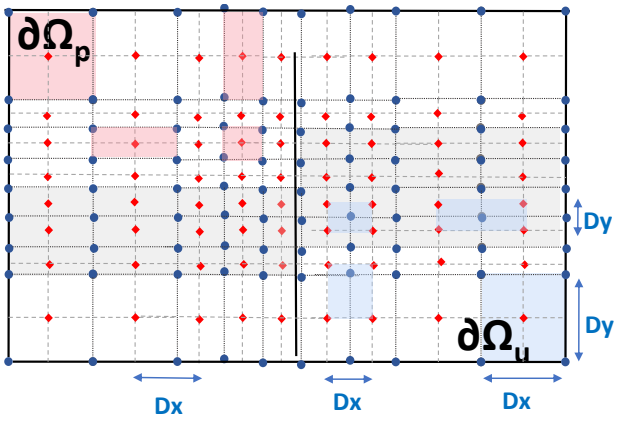

Figure 4.28.: New control-volumes for the locally refined scheme in the sEFVM showing the location of the pressure nodes (red) and displacement nodes (blue) and fault (black).

- The local refinement allowed for multiple depths to be captured in refined format. The results for this are shown in Figure 4.29. This figure demonstrates that an illustrative displacement field is smoothly captured with a single patch of refinement on cells in the central region of the reservoir.

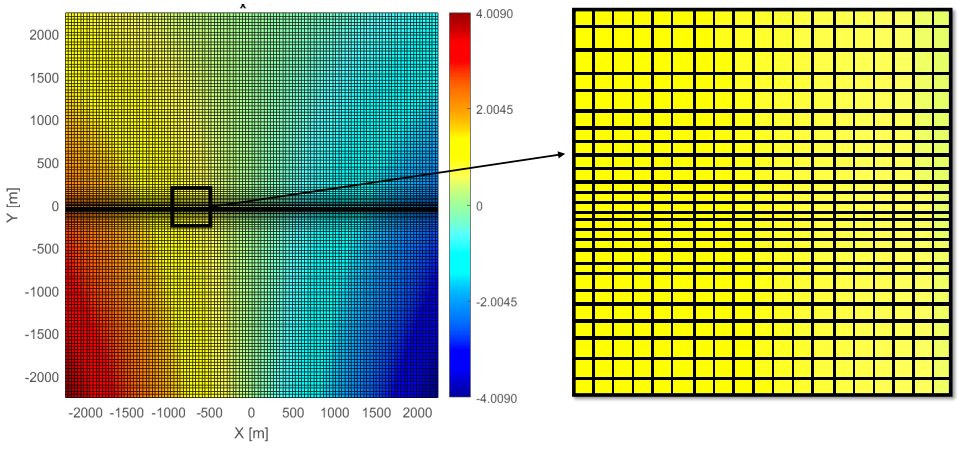

Figure 4.29.: A displacement profile obtained after grid refinement for the initialized system with details outlined in Table 4.1. This setup was studied earlier with results shown in Figure 4.22.

Despite implementing the aforementioned changes, the sEFVM's lack of accuracy, as shown in Figure 4.26 and Figure 4.25, persisted. It was acknowledged that the method has inherent limitations in achieving the required precision. Despite the sEFVM showing promising results even in comparison to known analytical solutions and simulators, this method was ultimately deemed insufficiently capable for studying depletion-induced fault reactivation in reservoirs with offset. For such cases, the stress profiles are not continuous and infinite peaks exists.

Following this acknowledgement, efforts were redirected towards seeking an alternative approach for simulating faulted reservoirs with offset. This lead to the development of the semi-analytical method with results discussed next.

4.2. SEMI-ANALYTICAL METHOD FOR FAULTED RESERVOIRS WITH DISCONTINUOUS SHEAR STRESS PROFILES

In this section, the results of the semi-analytical approach are presented. The first attempt was to ensure that the analytical stresses are calculated correctly over the sEFVM mesh.

The results for this were compared with code presented by [80] and [81]. For the case of a 70 degree fault with values of Table 4.1 and an offset of 75 meters and 25 MPa depletion, the effective normal stress and shear stress are compared for the purely analytical method and the semi-analytical method. The results are shown in Figure 4.30. The results show close agreement between the methods. Upon a closer look at the tails of the stress profile in Figure 4.30 it is observed that there is slight deviation between the methods. The semi-analytical method prediction are not exactly the same as the purely analytical approach. This is because for the purely analytical case, the assumption is an infinite reservoir. But for the test case modelled here, the system size is finite and equal to 4500×4500 m^2. When the results are repeated for horizontally-elongated domains (for example system size of 4500 m^2), the difference minimizes. This is because the horizontally elongated domain better resembles the assumption of an infinite reservoir.

In the next step, the slip is calculated analytically. The slip depends on the depletion. Figure 4.31 shows the slip patch growth for a 45 degree fault undergoing depletion. This angle is not relevant for the faults in the Groningen field but it is chosen so that various stages of the fault slip can be shown in one plot. The slip of the fault, as shown in this figure consists of the following stages:

- **No slip range** ($\sigma_c < 0$): In the analytical solution, there is an infinite peak to the Coulomb stress profile. This indicates that there is a point which slips, even initially, when the semi-analytical simulator predicts no slip at all. Due to the numerical errors inherent to the semi-analytical simulation, these infinite peaks are masked and the slip begins to be identified at a finite value of depletion. That is when the peaks of the estimated Coulomb stress become positive. Therefore in the semi-analytical solution, as long as the Coulomb stress profile is negative, there is no slip. This is shown in Figure 4.31 up to the depletion pressure of 11 MPa.

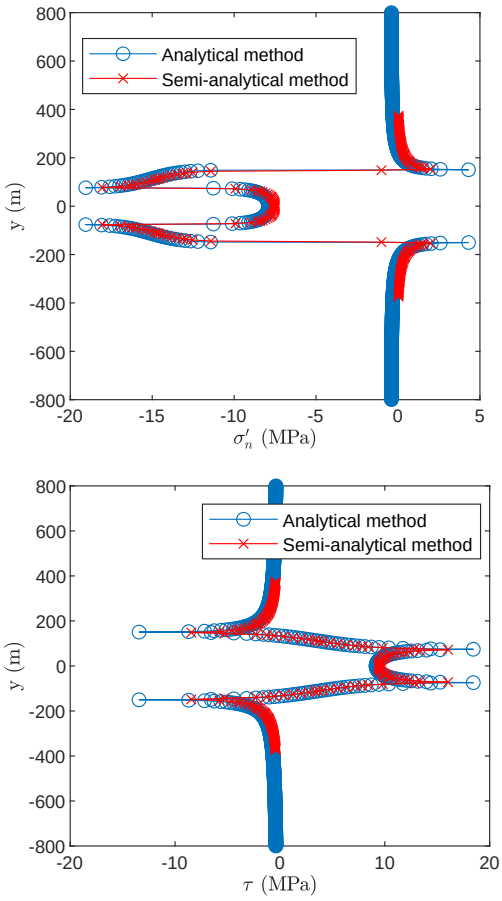

Figure 4.30.: Comparison of the effective normal stress (top) and shear stress (bottom) for the analytical and semi-analytical methods.

- **First point of slip**: It can be seen in Figure 4.31 that the slip patch begins to grow from the upper offset point. This occurs at 13.4 MPa of depletion. The reason why the top patch forms before the bottom patch and there is an element of asymmetry, is gravitational effects. Gravity results in a slightly higher Coulomb stress in the upper section. It is shown that unto a depletion of 14.8 MPa, the top patch continues to grow while the bottom patch does not slip.

- **Independent growth of two slip patches**: With further depletion, the bottom section will catch up. The Coulomb stress profile will be positive for both patches and there will be two slip patches. This is seen first in Figure 4.31 at a depletion pressure of 16.4 MPa. With increasing depletion, the two slip patches continue to grow. Until a depletion pressure of 24.4 MPa, there are two separate patches.

- **Merging of the slip patches**: It is seen that between the depletion pressure of 24.4 MPa and 27 MPa, the two slip patches have merged to form one large slip patch. This occurs quickly across one small pressure step. When the two slip patches merge, it is important for the semi-analytical method to recognize the merger and switch its calculation of slip to consider one large merged slip patch, as opposed to two smaller patches which have an overlap somewhere in between. As can be seen in Figure 4.31, the slip patch merger occurs before the entire Coulomb stress profile is on the positive side.

- **Growth of a single large slip patch**: Further depletion will result in the advancement of a single slip patch. If enough time passes, the slip profile form will also change. The slip profile is expected to eventually resemble the slip profile of the frictionless vertical fault shown in Figure 4.25.

The above mentioned points regarding the development and advancement of the slip profile pertain to the case of a fault with constant friction coefficient. If the friction coefficient depends on slip or time, there will be differences which will be outlined later in this chapter.

Figure 4.32 is a another form of representing the slip patch growth. Here, the slip patch is plotted versus the depletion pressure. Similar to Figure 4.31, the slip patch does not exist before 11 MPa. It is seen that the top patch grows first (at $y = 75$ m, the depth of the offset seen in Figure 2.4). This is followed by the bottom patch (at $y = -75$ m, corresponding to the bottom offset point). The two patches merge at a depletion pressure of $p = 22.9$ MPa. Following that there is only one single patch growing.

Another plot is shown in Figure 4.33. This is the slip patch profile for the original test case with the 70 degree fault. Here, a comparison is given between the results predicted with the current semi-analytical method and the method presented by [80]. This image shows that the two methods have results that are close. The slight difference between the methods is found to be mostly due to the assumption of an infinite reservoir in the analytical solution as opposed to a finite 4500×4500 m^2 model in the semi-analytical definition.

4.2.1. LINEAR SLIP WEAKENING FRICTION AND FAULT NUCLEATION

In this section the friction coefficient follows the linear slip weakening relationship defined in Equation 2.6.1. Three coefficients appear in this law: 1. the static friction coefficient (μ_{f_s}), 2. the dynamic friction coefficient (μ_{f_d}) and 3. the critical distance slip distance (δ) over which the friction drops.

It is noted that the critical distance is important because it is the combination of this parameter and μ_{f_d} which determine the slope of the slip weakening curve. This slope governs the Uenishi and Rice (2003) stability criterion described in Equation 2.33.

Smaller values for the dynamic coefficient result in a stronger slip-weakening regime and vice versa. When this law is used instead of a static friction coefficient, fault nucleation is observed.

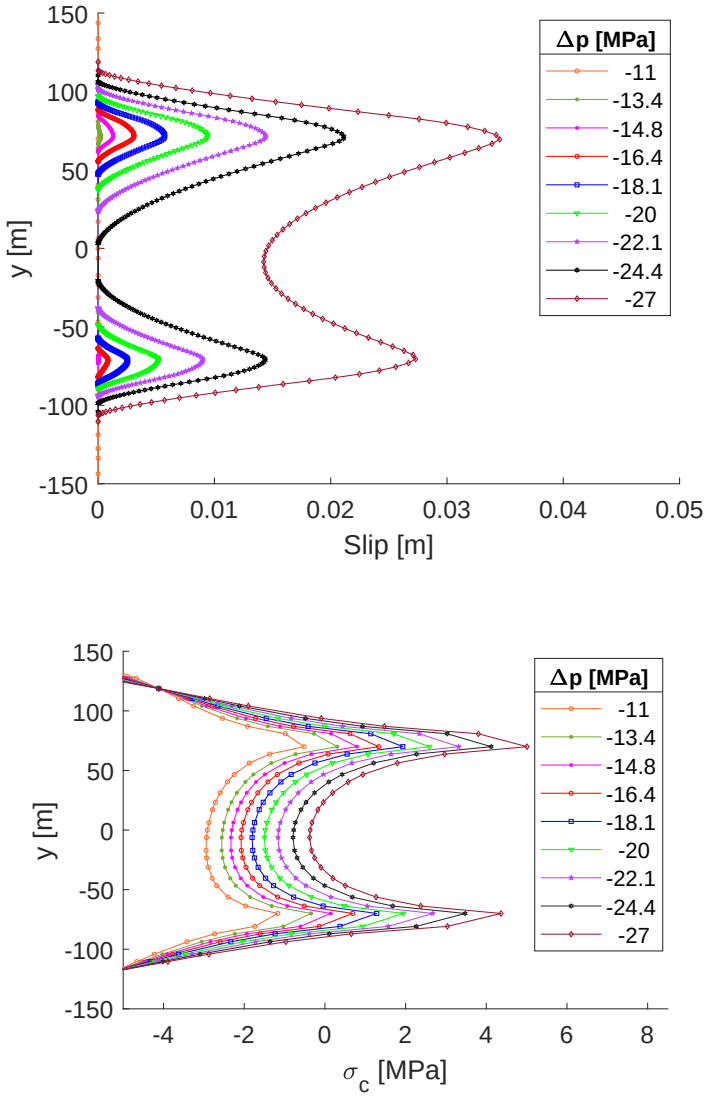

Figure 4.31.: The growth of the slip patch for a 45 degree fault with increasing depletion (top) and the corresponding pre-slip Coulomb stress profile (bottom).

Determination of fault nucleation is of high interest because it can be correlated with the occurrence of a seismic event. To define fault nucleation, it is useful to discern between the different phases a fault will go through when undergoing increasing Coulomb stresses [123]:

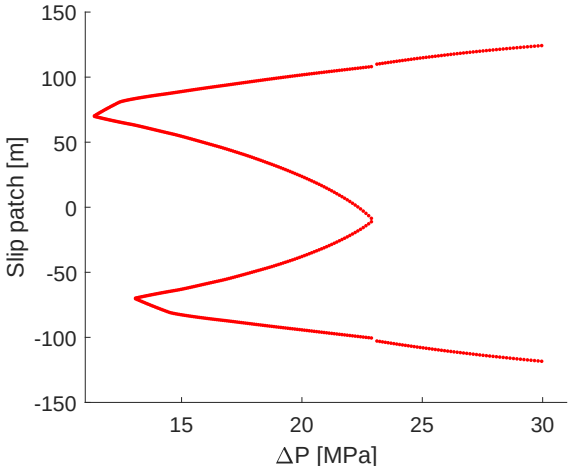

Figure 4.32.: Slip patch for a 45 degree fault undergoing depletion. Other properties for this simulation as are shown in Table 4.1.

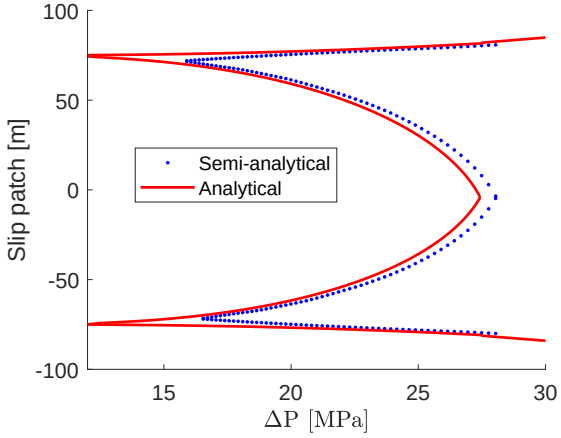

Figure 4.33.: Comparison of slip patch found using the analytical method presented by [80] and the semi-analytical method, for a 70 degree fault undergoing depletion. Other properties were defined in Table 4.1.

- The fault is initially stationary. Some models for friction assume an initial velocity for slip along the fault. This is the case for the rate and state friction model as shown by Equation 2.29. The initial slip velocity of a fault is not expected to be large in the geological scale. For the example of the Groningen field, where historically no seismic events are recorded prior to depletion, faults can be assumed inactive and stationary at first.

- Increasing Coulomb stresses on a fault may become large enough to induce slip of the fault. Initially, the fault will begin to slip steadily. This can be modelled assuming a quasi-static system.

- With further increase in the Coulomb stresses, it is possible that the fault nucleates. Fault nucleation is a pre-seismic stage just before an earthquake.

- If the Coulomb stresses surpass the nucleation point, then the fault will experience dynamic slip where slip will have an acceleration. This results in an earthquake.

The semi-analytical approach described here can model dynamics of poroelastic systems prior to dynamic slip. By assuming quasi-static conditions, the fault slip is modelled up to the point of nucleation. Fault nucleation can be determined via simulation and also with analytical equations according to the procedures outlined in Section 3.2.2 and Section 2.7.3.

When using the semi-analytical method, the quasi-static calculations will fail to converge when reaching nucleation. Analytically, nucleation can be found using the Uenishi and Rice formulation (2003) as described by Equation 2.33 [96]. The Uenishi and Rice formulation is preferred among researchers [12, 80] for determining nucleation. This is because using a numerical solver for finding nucleation point is time-consuming and is subject to errors stemming from the accuracy of the solver. The following points are relevant matters on the accuracy of the numerical solvers for finding nucleation point:

- In numerical simulation, it is very important to use sufficiently small pressure-steps to capture the correct nucleation pressure. With large pressure steps, the actual nucleation point can easily be over-stepped. For the example of the 70 degree fault shown in Figure 4.33, the pressure steps were in the order of $0.01-0.001$ MPa. To assist with simulation time, Jansen et. al. (2019) devised an automated pressure-stepping algorithm where pressure stepping is governed by the change in the size of a slip patch. Their algorithm would initially consider larger pressure steps. The steps would gradually minimize near the nucleation point. Close to nucleation, the algorithm would move above and below the nucleation point in a trial-and-error manner, to capture the nucleation more accurately [95].

- The number of fault and mesh grids also affect the results. The analytical solution can solve for hundreds of points along a fault and consider 4 blocks to model the setup of Figure 2.4. This is shown in the meshing for the method in Figure 3.3. This figure also shows the mesh of the semi-analytical method, which is the sEFVM mesh. The sEFVM considers one element for the fault per matrix mesh grid. This in itself reduces the number of points along the fault, in comparison to the analytical approach. For the example of Figure 4.30, the analytical solution considers 500 points along the fault while the sEFVM mesh allows for 100 points when a 360×360 matrix grid is used. The fewer number of grid nodes for the fault indicates a weaker estimation.

- Furthermore, as mentioned earlier, an assumption of the analytical solution is a reservoir which extends infinitely in the horizontal direction. However, the horizontal extent that can be modelled in the semi-analytical method is finite. This introduces deviations between the analytical and the semi-analytical methods. In reality, the Groningen field has areal dimensions which are large enough to be modelled as an infinite reservoir.

Given the above reasons, Jansen and Meulenbroek (2022), proposed a method for obtaining the nucleation point during numerical simulations with the assistance of the Uenishi and Rice method [95]. This is outlined in the Algorithm of the semi-analytical solution shown in Algorithm 2. In this algorithm, in every pressure step, the simulated slip patch is reported. The patch size is also calculated using the Uenishi and Rice formulation described in Equation 2.33 [96]. The two values are compared in each step. Nucleation is defined as the point where the larger slip patch size (i.e. the top patch), reaches a size equal or greater than the predicted Uenishi and Rice estimation for the nucleation slip patch size. This is shown in Figure 4.34.

Figure 4.34 shows four plots: 1. the simulated slip patch size for the top patch, 2. the simulated slip patch size for the bottom patch, 3. the analytically derived nucleation slip patch size using the Uenishi and Rice formulation for the top patch and 4. the analytically derived nucleation slip patch size using the Uenishi and Rice formulation for the bottom patch. The latter two plots include error bars to demonstrate a ±10% range for the calculated values.

This figure shows that all four plots demonstrate an increase in size of the slip patch with increasing depletion. In both cases (simulation and analytical Uenishi and Rice method), the growth of the lower patch is delayed in comparison to the upper patch. These findings are expected as demonstrated in the previous section.

The nucleation slip patch calculated using the Uenishi and Rice (2003) formulation is determined based on the effective normal stress profile for the segments of the fault which undergo slip [96]. This is outlined in Equation 2.33. The values are anticipated to remain constant because they indicate the value of the slip patch at nucleation point, as opposed to the plots for the semi-analytical method. The semi-analytical plots merely show the size of the slip patch at each depletion pressure.

Figure 4.34 shows that indeed, the calculated nucleation slip patch size using the Uenishi and Rice formulation is almost constant with increasing depletion. There are some negligible changes observed in the plots. This is due to the change in the effective normal stress profile used at each depletion step.

At around a depletion pressure of 25.1 MPa, the semi-analytical values for the slip patch size in the upper patch crosses the analytical Uenishi and Rice value. This point is identified as nucleation point. If the semi-analytical simulation continues, it will fail to converge at a later depletion pressure. This is shown in Figure 4.34 as the last plotted point at around 25.7 MPa. This pressure is the nucleation point determined by simulation. This value depends on the mesh and the pressure step size and carries a numerical error. For this reason and others explained earlier, the Uenishi and Rice criteria is used for determining nucleation.

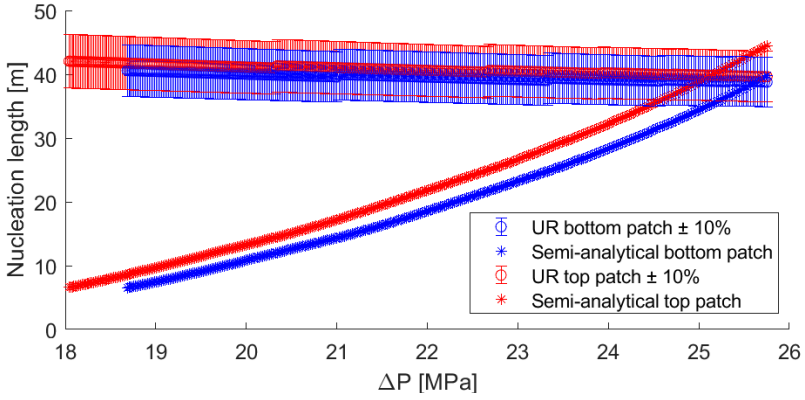

Figure 4.34.: Comparison of the slip patch growth using simulation with the semi-analytical approach and as determined using Equation 2.33. The setup is that described in Table 4.1.

According to the above procedure, the nucleation pressure is determined for the semi-analytical approach. Figure 4.35 shows the evolution of the slip patch profile with depletion for three different setups. They are all based on the 70 degree fault setup described in Table 4.1 but with different friction coefficients: 1. a constant friction coefficient of $\mu_f^s = 0.52$, 2 and 3. a linear slip weakening friction with a static friction coefficient of $\mu_f^s = 0.52$, a critical distance of $\delta = 0.02$ m and dynamic friction coefficients of $\mu_f^d = 0.4$ and $\mu_f^d = 0.2$, respectively.

Figure 4.35 shows that in the case of a static friction coefficient, the two slip patches grow and merge. However, for the cases with linear slip weakening friction, the slip patch profiles grow until nucleation is reached. The results of Figure 4.35 were obtained previously by Jansen and Meulenbroek (2022) [95]. The comparison of the found values for nucleation pressure in this study and the previous analytical study by Jansen and Meulenbroek (2022) is shown in Table 4.3. There are some differences between these values. The reason is the assumption of an infinite reservoir in the analytical method and also the differences in accuracy due to the coarser meshing in the semi-analytical method and the pressure stepping used.

4.2.2. STRATIGRAPHY-INFLUENCED FRICTIONAL RESPONSE ALONG THE FAULT

The faults in the Groningen field are not confined to the reservoir layer. They extend into the salt and also much further down into the underburden [124]. Lab tests on different layers of rock from the Groningen field have demonstrated that they have different frictional properties and behaviors when subjected to stress [105]. In this section, the effect of assuming relevant friction coefficients for the layers is analyzed. In the first try, constant friction coefficients for layers of the Groningen field are used. This is presented in Table B.1. The setup of Figure 2.4 is considered.

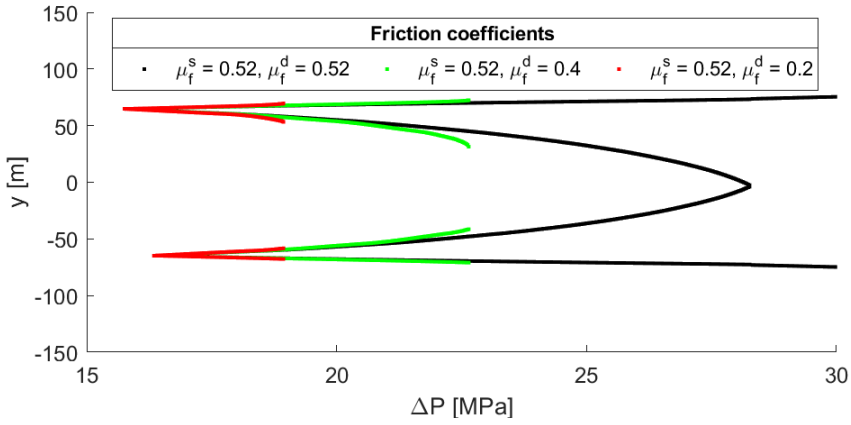

Figure 4.35.: Comparison of the slip patch growth for two different slip-weakening conditions in comparison to a constant friction setup. Other properties are as in Table 4.1.

Table 4.3.: Fault nucleation pressure in MPa, for various friction coefficients using the analytical method of Jansen and Meulenbroek [95] and the semi-analytical method. The grid for the semi-analytical method has 561×561 cells.

Case	analytical method	semi-analytical method
$\mu_f^s = 0.52, \mu_f^d = 0.52$	17.5	18.8
$\mu_f^s = 0.52, \mu_f^d = 0.40$	21.5	22.2
$\mu_f^s = 0.52, \mu_f^d = 0.20$	27.5	28.0

The system is initialized and depleted as explained in previous sections. Properties were the same as described in Table 4.1. The following assumptions were made:

- The friction coefficient is assumed to be constant, no linear slip weakening law is used.
- The static friction coefficient for the segments of the fault which are above the reservoir domain have the friction coefficient of the salt. A value of 0.64 is chosen based on the ranges for this parameter in Table B.1.
- The static friction coefficient for the reservoir segments of the fault, including the offset regions, is chosen as 0.52. This value falls in the ranges proposed by Hunfeld for the Groningen field [105].
- The friction coefficient for elements along the fault deeper than the reservoir and the offset are chosen based on the range for the Carboniferous layers of the Groningen field as 0.5 based on the ranges for this parameter in Table B.1.

The simulation results show that considering stratigraphy-influenced friction coefficients has no effect on the estimated slip profile and the nucleation pressure. This means the slip profile (and consequent nucleation pressure) remains the same if the friction coefficient for the reservoir (i.e. 0.6 in the current example) is used for the entire fault. This result can be found in Figure 4.35.

This finding is expected and can be explained via the analytical expressions used for the calculation of stress. The friction coefficient is used in the determination of the Coulomb stress profile. The analytically-determined Coulomb stress profile calculates incremental stresses as a result of depletion. Since only the reservoir segment is undergoing depletion, only the friction coefficient of this section influences the incremental stresses. The depletion-induced stress changes is not affected by the value of the friction coefficient considered for regions above the offset points where the reservoir ends.

Given this, another assumption is made, the top offset region (the region between h_1 and h_2 in Figure 2.4) is considered to be more strongly slip weakening than the other segments of the fault. This assumption is relevant to the Groningen field where studies have indicated a potentially stronger slip weakening friction behavior in the overlying salt layers [105]. The values used for this setup are shown in Table 4.4.

Table 4.4.: Friction properties considered for different frictional behaviors along a fault

Region	μ_f^s [-]	μ_f^d [-]	δ_c [m]
Top offset: Salt - Reservoir contact	0.6	0.3	0.02
Reservoir - Reservoir contact	0.52	0.4	0.02
Bottom offset: Carboniferous - Reservoir contact	0.52	0.4	0.02

The results are shown in Figure 4.36 for a 45 degree fault. This figure shows two series of plots. The red plots are for the case of similar frictional behavior all along the fault. For this case, the values for the reservoir-reservoir contact from Table 4.4 is assumed. The blue curve is a frictional behavior based on values defined in Table 4.4, where the salt-reservoir contact has a stronger slip weakening behavior. This shows the initial patches before nucleation and the merged patch following nucleation. When the the friction coefficient for the salt-reservoir offset contact is more strongly slip-weakening, the rupture profile is more than twice as large. This indicates that it is important to consider stratigraphy-dependent frictional behavior of faults in simulating fault re-activation.

4.2.3. SLIP RATE-DEPENDENT FRICTION COEFFICIENT

The friction coefficient can change with the rate of slip as outlined in Equation 2.29. This is modelled using the semi-analytical method with the following assumptions:

- The rate of depletion is selected based on the actual rate of depletion in the Groningen field. This is shown in Figure B.1. Given a 30 MPa depletion in about 60 years, a depletion rate of 0.5 MPa per year is calculated.

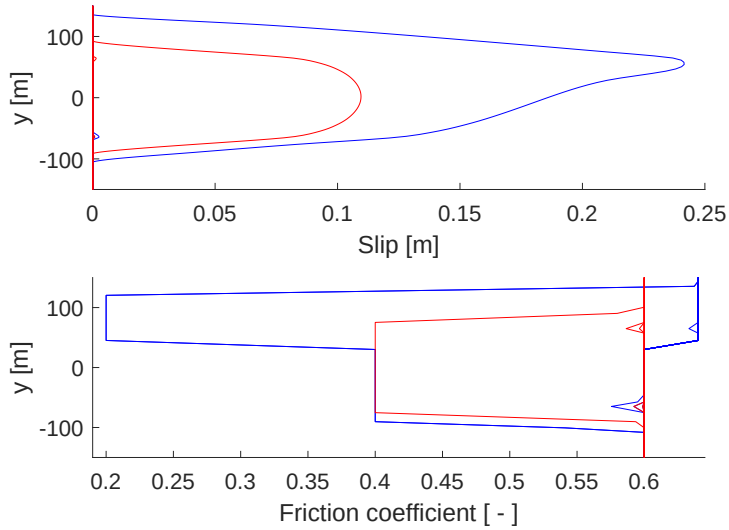

Figure 4.36.: Comparison of the slip patch profile (top) and corresponding friction coefficient (bottom) for a stratigraphy-dependent friction law (blue) and a stratigraphy-independent friction law (red). Other parameters are as shown in Table 4.1.

- The constants of the rate-dependent friction law (Equation 2.29) are extracted based on the ranges suggested for the Groningen field [105]. These values are reported in Table B.2.

Various test cases are studied by choosing values for the friction parameters within the ranges reported for the Groningen field. These ranges are available in Table B.2. The results show that the slip patch growth is observed to grow in a step-wise manner when considering slip rate-dependent friction.

One example is shown in Figure 4.37. The parameters of Equation 2.29 for this test case are $\mu_f^s = 0.52$, $V_0 = 1\mu$ m/s, $A = 0.01$ and $B = 0.0025$. Other properties are as in Table 4.1. This figure shows that the slip patch grows with oscillations. This is due to the oscillations observed in the friction coefficient as shown in Figure 4.38

The results for slip rate-dependent friction are not interpreted to hold substantial justifications for further investigation. Besides the oscillatory results, one of the concerns in this analyses is the large magnitude of the initial slip velocity. The values for V_0 reported based on lab experiments for the Groningen field are in the range of 0.1 to 10 micro meters per second [105]. This is equivalent to 3 to 300 meters per year. This does not seem to be a reasonable range for an initial fault slip velocity in the field scale.

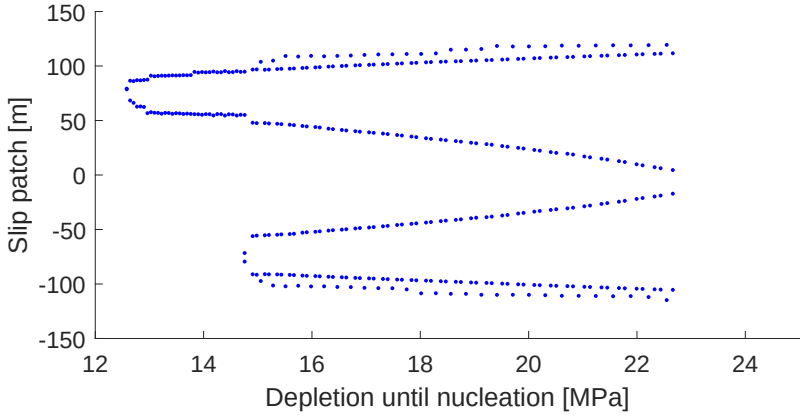

Figure 4.37.: The slip patch profile for the case with a slip rate-dependent friction coefficient showing step-wise growth of the slip patch.

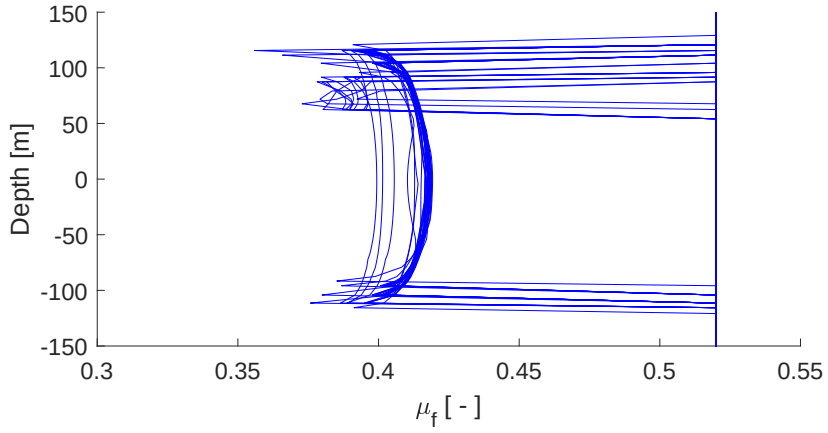

Figure 4.38.: The friction coefficients corresponding to the slip patch profiles of Figure 4.37. The friction coefficient depends on the rate of slip in this example.

4.2.4. MAGNITUDE OF THE SEISMIC MOMENT

The magnitude of the seismic moment (M_s) can be calculated using Equation 3.43. M_s depends on the sizes of the slip patches at nucleation pressure. For the case of the 70 degree fault of Table 4.1, a seismic moment of 84 GNm/m is calculated using the semi-analytical method. This is considering linear slip weakening friction with coefficients of the aforementioned table.

4.3. SENSITIVITY ANALYSES OF CRITICAL PARAMETERS INFLUENCING INDUCED SEISMICITY

The semi-analytical solution, implemented on the sEFVM mesh, is computationally more efficient than the sEFVM. Due to this higher efficiency, it is much faster and allows for a more refined mesh. While the sEFVM is itself computationally efficient given it's embedded treatment of faults, it involves solving for fully coupled fully implicit equations for all grid cells. This is demonstrated by the system of equations shown in Equation 3.26. The semi-analytical solver relies on the analytical solution and solves only for the grid cells which undergo pressure change, as opposed to all grid cells in the system.

In this section the computational efficiency of the semi-analytical method is leveraged to perform sensitivity analyses of some of the more influential parameters involved in induced seismicity in the Groningen field. Previous research on the topic has lead to the identification of some of these parameters [76, 77, 95, 102]. Where possible, the results have been quantitatively compared with previous findings.

The following parameters are investigated for their effect on the nucleation pressure and the magnitude of the seismic moment:

- Fault angle
- Fault throw (i.e. the offset)
- Friction coefficient
- Reservoir thickness

In the following sections, each sensitivity parameter is studied by running tens to hundreds of simulations. Given the extensive number of simulations, computational resources from the DelftBlue supercomputer were used to perform the calculations [125].

The domain size used in these simulations is the setup of Figure 2.4. However, this reservoir is elongated horizontally 5 times to obtain results that are more relevant to an infinite system. The mesh for the semi-analytical approach is 1000×2500. For other properties, values are taken from Table 4.1.

It should be noted that another parameter of interest in the study of fault reactivation is the effect of heterogeneity in geomechanical properties across layers. However, the semi-analytical method developed here relies on analytical expressions that were derived assuming homogeneity [95]. For this reason, all considered simulations assume homogeneity across layers and the values used for the geomechanical constants are as reported in Table 4.1.

4.3.1. FAULT ANGLE

Fault angles relevant to the Groningen field are in the range of 60 to 90 degrees with respect to horizontal [76, 77]. The sensitivity analysis here includes a range of 30 to 90 degrees. Other properties besides the fault angle are as in Table 4.1.

The results in Figure 4.39 show among the studied range of 30 to 90 degrees, only faults with angles in a range of 50 to 80 degrees nucleate when depletion is considered up to a maximum depletion of 35 MPa. For fault angles between 30 to 50 degrees and between 80 to 90 degrees, fault nucleation does not occur. That is why there are no data points for these angles in Figure 4.39. Furthermore, faults in the range of 55 to 70 degrees tend to nucleate earlier. Faults at an angle less than 55 degrees and higher than 70 degrees will require higher depletion pressures to reach nucleation.

A property present in both plots of Figure 4.39 is a degree of perturbations (non-smoothness) in the plots. These oscillatory perturbations arise from the varying accuracy of the numerical method for each case. The accuracy of the semi-analytical method depends on the mesh size. As the fault angle is changed for each data point, the reservoir is captured slightly differently in when modelled using the Cartesian mesh of the sEFVM. The depths pertaining to the offset points (at 75 m and 150 m) would not be exactly captured. These depths can be over or undershot by the Cartesian mesh. Furthermore, the accuracy of the captured nucleation pressure depends on the pressure stepping. These introduce the small kinks observed in the plots.

In a 2015 report by Van den Bogert on induced seismicity in the Groningen field [76], the effect of fault angle on the initiation of slip is studied. As previously noted, with infinite peaks in the Coulomb stress profile, there are always points that slip. In this sense, the onset of fault slip is not deemed to hold much value in the study of induced seismicity. However, the results reported by Van den Bogert (2015) are compared with the findings of this report for the effect of fault angle of fault nucleation. While onset of fault slip and fault nucleation are quite different, they are compared for the purpose of an evaluation.

The 2015 report report by Van den Bogert [76] considered fault angles between 60 to 90 degrees. Their simulations showed that the onset of fault slip occurs at a higher depletion pressure for vertical faults in comparison to faults with an angle of 65 degrees and less (with the horizontal). It is also reported that for cases without a throw, the faults with angles above 69 degrees do not slip at all in the depletion range up to 30 MPa [76]. Both findings are in agreement with the results of the semi-analytical method for fault nucleation. Figure 4.39 shows that the magnitude of the seismic moment is higher for faults with a lower angle. This indicates that if a fault with a shallower angle nucleates, a larger seismic event is expected.

In conclusion, faults with shallower dip angles are observed to nucleate at a lower reservoir depletion pressure and exhibit a greater seismic moment.

4.3.2. FAULT THROW

In this section, the fault throw is studied. The fault throw is kept constant at 75 m in all the results demonstrated so far in this report. In this section, ranges are considered considered for this property. The fault throw range is considered between 0 m (i.e. no offset, where the sides of the reservoir across the fault align as shown in Figure 2.3) and 225 m (i.e. the offset is equal to the entire thickness of the reservoir).

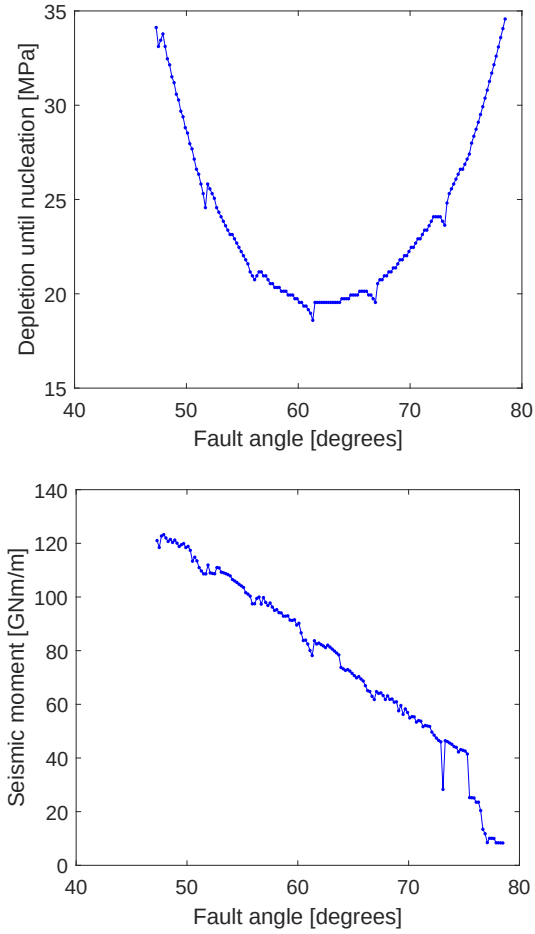

Figure 4.39.: Nucleation pressure (top) and the magnitude of the seismic moment (bottom) for various fault angles.

In order to demonstrate the effect of angles, the results are repeated for three different fault angles of 50, 70 (base case of Table 4.1) and 90 degrees. The results for the estimated nucleation pressure and magnitude of the seismic moment are shown in Figure 4.40. This figure shows that with increasing fault throw, the depletion needed to reach nucleation declines. This means it is easier for a fault to nucleate when the offset is larger. The effect is similar for all fault angles. This image also shows that the 90 degree fault may also nucleate in the considered depletion range if the offset is high enough (over 170 m). In Figure 4.39 it is seen that for a 75 m throw, the 70 degree fault has nucleation at the lowest depletion, followed by the 50 degree fault and lastly the 90 degree fault (which does not nucleate at all).

The same is observed for the plots in Figure 4.40 where the 70 degree faults nucleates at lower pressures followed by the 50 degree fault and lastly the 90 degree fault. This conclusion is valid over all considered fault throws.

The magnitude of the seismic moment for the corresponding angles and fault throws are plotted in Figure 4.40. This image reiterates the finding of Figure 4.39: that shallower fault angles create larger seismic events. Furthermore, it is observed that with increasing fault throw, M_s declines. This means that while faults with higher offsets will nucleate at lower depletion pressures, they are not expected to create larger seismic events. In other words, larger seismic events are expected where offset is smaller.

The above findings are in agreement with reports by Buijze (2020). Buijze reports that a larger offset promotes nucleation, but results in smaller slip patches [102].

In 2015, Van den Bogert studied the effect of fault throw on the onset of fault slip [76]. This study suggested the depletion required for reaching the onset of fault slip is lower for faults with a fault throw equal to reservoir thickness and vice versa for faults without a throw. The report states that faults with an offset equal to the reservoir thickness will be triggered to slip with the least depletion. Comparing these statements to the results of Figure 4.40 shows that they are in agreement if onset of fault slip is compared to the onset of fault nucleation. The argument that the two (onset of slip and fault nucleation) are different and that onset of fault slip holds little value in the study of induced seismicity is valid in this comparison.

A followup report to 2015 report was published in 2018 by van den Bogert [77]. This study reports on the onset of rupture, as well as the onset of slip as a function of reservoir offset. The parameters used in the report by Van den Bogert (2018) are different from those used in the current sensitivity analysis. Therefore the results could not be numerically compared. However, the results from the 2018 report qualitatively confirm the findings that faults in reservoirs with higher offsets will nucleate earlier. Both reports demonstrate an "s-shape" for the change in nucleation pressure for different fault offsets, as observed in Figure 4.40.

In a more recent study by Jansen and Meulenbroek (2022) on the effect of fault throw, it is shown that the nucleation pressure increases with an S-shape for increasing fault throw. However, there is a maximum in the seismic moment at a fault throw equivalent to 80% of the reservoir thickness in the studied example [95]. While the input parameters for both studies rely on the values from Table 4.2, the maximum value is not evident in the results obtained from the semi-analytical model, as illustrated in Figure 4.40. This difference is due to the effect of coupling between the slip patches. Jansen and Meulenbroek (2022) consider the coupling between slip patches [95] but this effect is neglected in the semi-analytical method developed in this study. The difference between the results highlights that the coupling between slip patches becomes increasingly important for larger fault throws. It is reported that the Uenishi and Rice (2003) expression for the nucleation length (i.e. Equation 2.33) is only valid for single slip patches in a single fault [96]. Hence, the accuracy of the semi-analytical method is expected to diminish as slip patches approach each other and further investigation is required to determine the applicability of the Uenishi and Rice criterion for multiple faults.

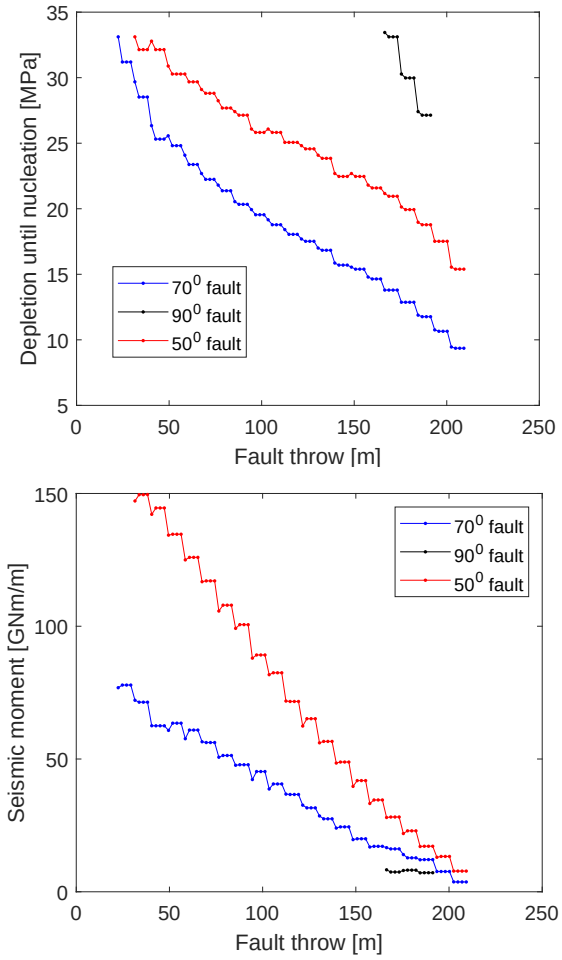

Figure 4.40.: Nucleation pressure (top) and the magnitude of the seismic moment (bottom) for various fault throws, at three different fault angles.

4.3.3. FRICTIONAL PROPERTIES

In the cases described in this chapter so far, the friction coefficient followed a linear slip weakening relationship with $\mu_f^s = 0.52$, $\mu_f^d = 0.4$ and $\delta = 0.02$ m. In this section, a sensitivity study is done on friction parameters. The sensitivity analysis is divided into three parts:

- A sensitivity analysis on the static friction coefficient, μ_f^s, with constant dynamic friction coefficient and a constant critical slip distance.
- A sensitivity analysis on the dynamic friction coefficient, μ_f^d, with constant static friction coefficient and a constant critical slip distance.

- A sensitivity analysis on the dynamic friction coefficient while assuming a constant slope for the linear slip weakening equation and a constant static friction coefficient.

Where not mentioned, other parameters, besides the friction coefficient are as in Table 4.1.

SENSITIVITY ANALYSIS ON THE STATIC FRICTION COEFFICIENT

The static friction coefficient is an important parameter in the Coulomb stress affecting the fault. In this section, a sensitivity analysis is done to evaluate the implications of the value of this variable.

For this purpose, simulations are run by considering a range for μ_f^s while keeping other parameters constant. This range is from 0.52, the initial value for μ_f^s from Table 4.1, up to a value of 0.7. This range is chosen based on literature. The value taken by Jansen and Meulenbroek (2022) for the friction coefficient is 0.52 [95]. This value is 0.55 in the report by Van den Bogert (2018) [77]. In the study by Hunfeld (2020) the value of 0.6 is reported for the static friction coefficient in the reservoir sand. The highest value of 0.66 was reported for the basal Zechstein [105]. Given these values, the 0.52 - 0.7 range was considered in this sensitivity analysis.

A linear slip weakening relationship is used for the simulations. The dynamic friction coefficient is constant and equal to 0.4. The critical distance is 0.02 m for all cases. A schematic for the considered friction regime is shown in Figure 4.41. In reality, simulations are performed with a stepping size of 0.001 chosen between 0.52 to 0.7 for the static friction coefficient.

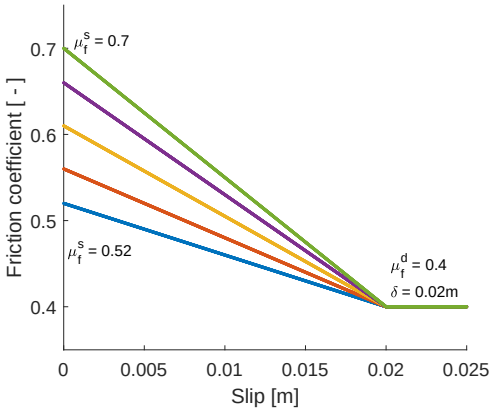

Figure 4.41.: The change of the static friction coefficient by maintaining dynamic friction coefficient and critical distance.

Figure 4.42 shows the results. Initially, three fault angles of 50, 70 and 90 degrees are considered as in previous sections.

For the case of the 90 degree fault, there is no nucleation for any static friction coefficient within the considered range of 0.52 to 0.7. This is in agreement with the results of Figure 4.39 where it is shown the 90 degree fault does not nucleate for the 0.52 static friction coefficient for the maximum depletion.

The results for the nucleation pressure in Figure 4.42 show that for higher static friction coefficients, a higher depletion is required for a fault to nucleate. Comparison between the 50 degree and 70 degree fault shows that the 70 degree fault will nucleate while the static friction coefficient changes in a wider range, while for the 50 degree fault there is a smaller range of static friction coefficients which allow for fault nucleation. The slope of the change is higher for the 50 degree fault than the 70 degree fault. This indicates that slight changes in the static friction coefficient will affect nucleation pressure more for the shallower angle 50 degree fault, than it would for the 70 degree fault.

The results for the magnitude of the seismic moment of Figure 4.42 show that when faults with a higher static friction coefficient nucleate, the magnitude of the seismic moment will be higher. By putting the results from both the nucleation pressure and magnitude of the seismic moment it can be argued that when the static friction coefficient is higher, it takes longer for a fault to nucleate. However, when the fault does nucleates, it can potentially cause a stronger seismic event.

Given that there is no nucleation for the 90 degree fault, the results for the constant friction coefficient is repeated at more fault angles to analyze the changes with respect to fault angles. Figure 4.43 shows the results. The following conclusions can be made based on this figure.

- As previously seen in Figure 4.42, the magnitude of the seismic moment and nucleation pressure increase with increasing static friction coefficient for all fault angles.
- The slope of this change is not the same for different fault angles. The results of this section reiterate that different fault angles result in a different initial pressure of nucleation. The faults with angles 60 to 65 will nucleate at lower depletion pressures. The effect of the static friction coefficient on the nucleation pressure is greater on the 60 degree fault.
- For a static friction coefficient of 0.6, the 70 degree fault nucleates before the 60 degree fault. This indicates that if the results of Figure 4.39 on nucleation pressure versus fault angle were repeated at a higher static friction coefficient, the curve will change.
- Although the considered range for the static friction coefficient is the same for all fault angles (i.e. from 0.52 to 0.7), the plots do not extend throughout to the higher end of the range for all plots. The reason is that nucleation does not occur for the higher static friction coefficients in these plots. For example, the plot for the 50 degree fault ends at a μ_f^s less than 0.55, indicating that the fault nucleation does not occur for any static friction coefficient larger than this value.

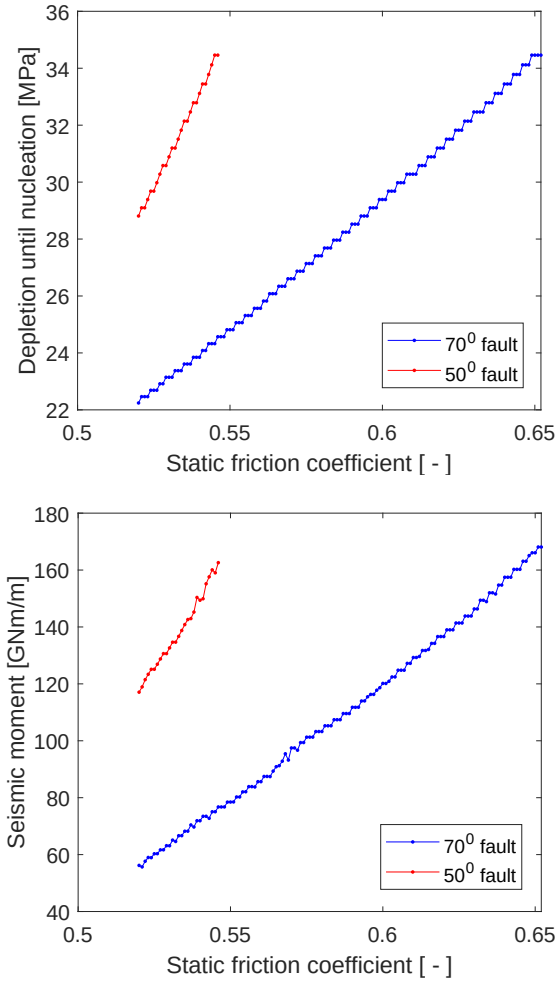

Figure 4.42.: Nucleation pressure (top) and the magnitude of the seismic moment (bottom) for various static friction coefficients.

In 2018, Van den Bogert studied the effect of the slope of the linear slip weakening law on nucleation. He finds where the slope is larger, a smaller amount of depletion is required for the fault to nucleate [77].

In Section 2.7.3 the analytical formulations used by Uenishi and Rice (2003) for the critical slip patch size were reviewed [96]. Their formulations are used in this study to determine the critical slip patch size. They suggest Equation 2.35 for determining the critical slip patch size. This equation determines the critical patch size, based on the slope of the linear slip weakening friction law.

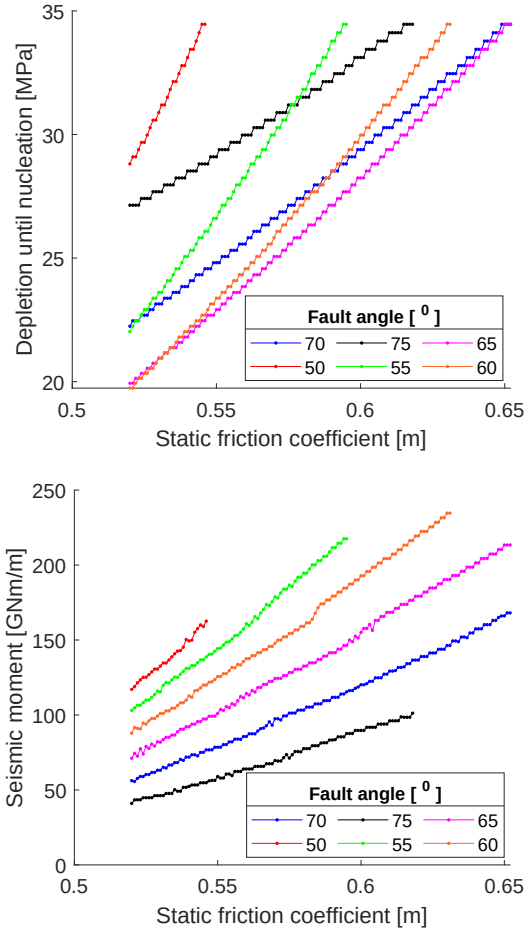

Figure 4.43.: Nucleation pressure (top) and the magnitude of the seismic moment (bottom) for various static friction coefficients at different fault angles.

The slope of the linear slip weakening law can be calculated according to Equation 2.6.1) and is defined as

$$\frac{d\mu_f}{ds} = -\frac{\mu_f^d - \mu_f^s}{\delta}. \tag{4.20}$$

According to Equation 4.20, when the slope of the linear friction weakening law is smaller, the critical length is smaller. Therefore, a fault will nucleate earlier at a smaller depletion pressure.

In the results of Figure 4.41, by altering the static friction coefficient and maintaining the dynamic friction coefficient, the slope of the friction coefficient plot is also changing.

The plots with the smaller static friction coefficients have a softer slope. It is observed that the nucleation pressure is smaller for faults with a softer slope. This agrees with the findings of Van den Bogert (2018) [77].

SENSITIVITY ANALYSIS ON THE DYNAMIC FRICTION COEFFICIENT

The dynamic friction coefficient affects the Coulomb stress profiles in the fault once slip occurs. This parameter has been studied for the evaluation of rupture propagation and reported to affect fault nucleation [102].

In this section, this coefficient is studied by assuming linear slip weakening relationship for friction with varying values for the dynamic friction coefficient.

The range considered for the dynamic friction coefficient is 0.3 to 0.5 with a stepping size of 0.001. The static friction coefficient is maintained at 0.52. The critical distance is also kept constant at 0.02 m. A schematic of the considered frictional curves for this section are shown in Figure 4.44.

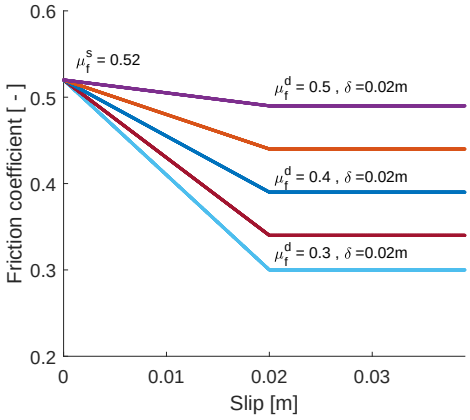

Figure 4.44.: The change of the dynamic friction coefficient by maintaining static friction coefficient and critical distance.

Figure 4.45 shows the results. The 90 degree fault does not slip even with the lowest dynamic friction coefficient of 0.3. That is why the results for this angle are not seen in the plot. Analyses of Figure 4.44 suggests the following points

- Fault nucleation can occur at lower depletion pressures when the dynamic friction coefficient is smaller. This is in accordance with what is expected, because a stronger slip-weakening tendency is anticipated to result in earlier nucleation.
- The nucleation pressure curve has a slight change in its slope at about $\mu_f^d = 0.4$ for the current configurations. This indicates that the sensitivity of the nucleation pressure to the dynamic friction coefficient can be related to the value of the dynamic friction coefficient.

Figure 4.44 suggests that the dynamic friction coefficient has a higher impact on nucleation, when it holds a higher value. In other words, When the dynamic friction coefficient is in the 0.45 to 0.4 range, the fault nucleation pressure drops faster as compared to when it is in the 0.4 to 0.35 range.

- The nucleation pressure for various angles agrees with the trend in Figure 4.39. In both Figure 4.39 and Figure 4.45, faults with angles in the 60 to 65 range will nucleate at lower pressures in comparison to faults positioned at shallower angles (55 and 50 degrees) and steeper angles (70 and 75 degrees).

- The magnitude of the seismic moment is smaller for larger dynamic friction coefficients, for all fault angles considered. This is expected because a larger dynamic friction coefficient indicates a weaker slip-weakening frictional behavior. This consequently results in smaller slip patches.

- Nucleation of a fault positioned at a shallower angle results in a larger seismic event. This agrees with the previous results in the sensitivity analysis on fault angles, as shown in Figure 4.39.

- The magnitude of the seismic moment is more sensitive to the dynamic friction coefficient for lower ranges of the dynamic friction coefficient. In other words, the seismic moment increases more rapidly with a drop in the dynamic friction coefficient in the 0.35 - 0.4 range, in comparison to the 0.4 - 0.45 range.

- Although all the simulations were run for a friction coefficient in a range of 0.3 to 0.5, the results do not extend all the way to the lower range of the friction coefficient (i.e. $\mu_f^d = 0.3$). The results for shallower fault angles (50, 55, 60 and 65 degrees) stop before reaching this limit. The reason for this is that the solution cannot be found for these configurations. The point, after which a solution does not exist, can be predicted beforehand for a known configuration. When the dynamic friction coefficient is smaller than a threshold, the analytical solution to the problem cannot be found. This is the case for the run-away rupture. Buijze (2020) reports on the sudden drop in the stresses resulting from a strong slip weakening regime as a contributing factor to run-away ruptures [102]. This is elaborated in Section 2.7.

Figure 4.45 is in agreement with an earlier report by Buijze (2020) [102]. She reports that a higher depletion is required to reach nucleation, when the dynamic friction coefficient has a larger value. This tendency is observed for all fault angles considered in the sensitivity analysis here.

Buijze (2020) also reported that the length of the rupture is larger for smaller values of the dynamic friction coefficient and largest rupture size correlates with the lowest dynamic friction coefficient [102]. The results for the magnitude of the seismic moment of this study suggest that larger events can be expected for smaller friction coefficients.

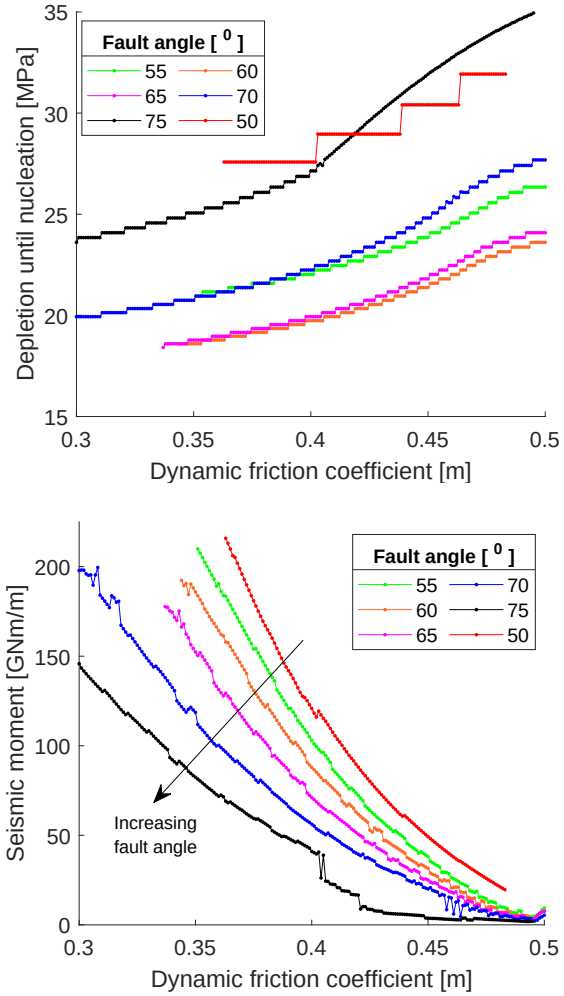

Figure 4.45.: Nucleation pressure (top) and the magnitude of the seismic moment (bottom) for various dynamic friction coefficients at different fault angles. The friction law used here is shown in Figure 4.44

CRITICAL LINEAR SLIP WEAKENING DISTANCE

The critical distance in the linear slip weakening equation also influences the frictional behavior of fault and therefore the stresses. In this section a sensitivity analysis is performed on this parameter while maintaining the static and friction coefficient and the slope of the linear slip weakening friction as those reported in Table 4.1.

According to Equation 4.20, the slope of the linear slip weakening equation for the default values of table 4.1 is -0.06 mm^{-1}. In order to perform a sensitivity analysis on friction by maintaining this slope, values for δ and μ_f^d are changed simultaneously. The schematic for the friction regimes of this section are shown in Figure 4.46. In the simulations, the dynamic friction coefficient is changed between 0.3 to 0.5. Correspondingly, to keep the slope of frictional weakening at 0.06 mm^{-1}, the critical distance (δ) is altered from 0.036 to 0.003. A stepping size of 0.001 is used. Similar ranges were considered in an earlier study on the Groningen field by Van den Bogert (2018) [77] In that study, the static friction coefficient is assumed to be 0.55 and the critical slip distance is altered between 0.005 m to 0.03 m while maintaining the slope of the slip-weakening law.

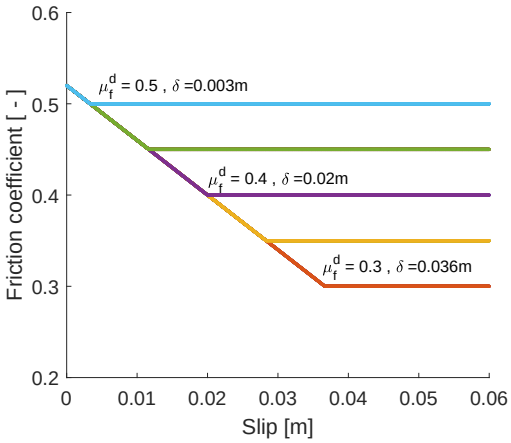

Figure 4.46.: The change of the friction coefficient by maintaining the slope for the slip-weakening law.

The results are repeated for different angles. The vertical (90 degree) fault does not nucleate in the considered range. Other results are shown in Figure 4.47.

The results from Figure 4.47 show the following:

- The results for the nucleation pressure show that for the smaller ranges of the dynamic friction coefficient, the nucleation pressure remains unchanged. This indicates that when the slope of the linear slip weakening law remains unchanged, the drop in the dynamic friction coefficient does not initially influence the nucleation pressure.
- For larger dynamic friction coefficients, the nucleation pressure increases with a reduction in the slip-weakening behavior of the fault. This is also observed earlier, in the study on the dynamic friction coefficient shown in Figure 4.45.
- The study of the nucleation pressure for various fault angles follows the trend that was earlier found for the effect of fault angle on nucleation in Figure 4.39.

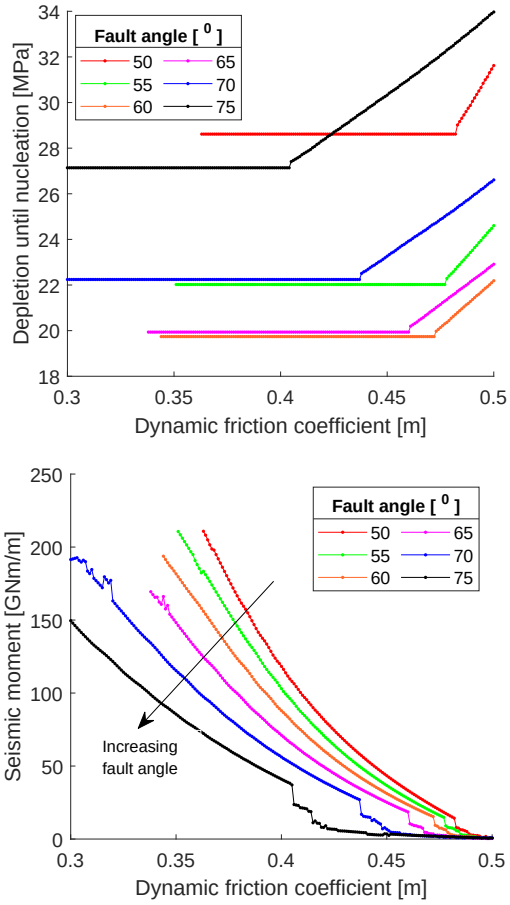

Figure 4.47.: Nucleation pressure (top) and the magnitude of the seismic moment (bottom) for various dynamic friction coefficients at different fault angles.

Accordingly, at the same dynamic friction coefficient, the 60 degree fault will nucleate at the smallest depletion pressure, this is followed by the 65 degree, 55 degree, 70 degree, 50 degree and lastly the 75 degree fault.

- The magnitude of the seismic moment decreases with increasing dynamic friction coefficient. For the ranges of friction coefficient where the nucleation pressure is constant, there is a drop in the magnitude of the seismic moment. This indicates that the slip patch size at nucleation differs for various cases. With a weaker slip-weakening regime, which corresponds to a higher dynamic friction coefficient, the slip patch is smaller and this results in a smaller seismic moment.

- The magnitude of the seismic moment drops to very small values for larger friction coefficients. A comparison with the nucleation pressure shows that for these higher dynamic friction coefficients, the depletion pressure required for nucleation is larger. This indicates that the slip patch has a smaller size and suggests a smaller magnitude of the seismic moment.

In the 2018 report by Van den Bogert [77], similar setups to those shown in Figure 4.46 have been studied. Van den Bogert found a reduction in the magnitude of the seismic moment for faults with a higher dynamic friction coefficient. He reported that the slope of this decrease is different based on the rupture mechanism, but the decrease is observed for all friction coefficients. With respect to the nucleation pressure, Van den Bogert (2018) [77] considered three dynamic friction coefficients between 0.25 to 0.5 while altering the critical slip distance to maintain the slope of the linear weakening friction law at 0.01 mm^{-1}. He showed that the onset of fault nucleation happens at 21.05 MPa of depletion for all cases with a dynamic friction coefficient of 0.47 or smaller. For the cases with dynamic friction coefficients of 0.48 and larger, the depletion required to reach fault nucleation increases significantly with the dynamic friction coefficient. For the larger dynamic friction coefficient of 0.5, the seismic rupture occurs at a pressure depletion of 27.4 MPa. The results of Figure 4.47 are in agreement with the findings of van den Bogert (2018) [77].

4.3.4. RESERVOIR THICKNESS

Reservoir thickness is one of the parameters which researchers have addressed in the study of induced seismicity in the Groningen field [77]. In this section a sensitivity study is done on the thickness of the reservoir.

In the first attempt, the reservoir thickness is analyzed while maintaining the value of the offset. For this purpose, the values of h_1 and h_2 of Figure 2.4 are changed by the same magnitude as shown in Table 4.5. All cases have an offset of 75 meters. The thickness is changed by 10 m, equivalent to 4.4% of the total reservoir thickness.

Table 4.5.: Considered cases for the study of the effect of reservoir thickness while maintaining the magnitude of the offset

Case	Change in thickness [m]	h_1 [m]	h_2 [m]
Base case	0	150	75
Thinner reservoir	-10	145	70
Thicker reservoir	+10	155	80

The results are shown in Figure 4.48. The results of this figure shows that with change in reservoir thickness, the nucleation pressure change is almost visually indiscernible. If the tail of the plot for higher fault angles (close to 80 degrees) is considered for comparison, it can be observed that the thicker reservoirs require a higher depletion to reach nucleation. However, the difference is in the order of fractions of an MPa.

In the 2015 report by Van den Bogert (2018), the reservoir thickness is changed while maintaining the normalized offset. In this study the reservoir thickness is changed between 170, 200 and 230 meters, equivalent to 15% change in the thickness from the base case. The normalized offset is defined as the actual offset distance divided by the total reservoir thickness. This definition is different from those considered in the current sensitivity analyses (with details provided in Table 4.5.

Van den Bogert (2018) concluded reservoir thickness in the case of a constant offset does not affect the onset of fault slip. However, for the onset of nucleation, they found that further depletion is required for the thinner reservoir to reach nucleation as compared to the thicker reservoir. The figures reported by Van den Bogert shows the magnitude of this effect to be less than a fraction of an MPa [77].

Figure 4.48 demonstrates the effect of reservoir thickness on the magnitude of the seismic moment. This figure shows that higher magnitudes of the seismic moment are expected for faults in the thicker sections of a depleting reservoir. It is also noticeable that the effect is greater for faults with shallower angles. Overall, the highest magnitude of a seismic event can be expected for faults with shallower angles and located in the region with largest thickness. The effect of thickness on the magnitude of the seismic moment can be explained with attention to the size of the slip patch. In the case of the thicker reservoir, the slip patches grow further to reach the point of nucleation. Larger slip patches contribute to a higher seismic moment once they reach nucleation according to Equation 3.43.

The analysis for the magnitude of the seismic moment is also reported by van den Bogert (2018) [77]. Van den Bogert (2018) defined the relationship between the magnitude of the seismic moment and reservoir thickness based on the rupture mechanisms. He defines the following rupture mechanisms:

- **Mechanism 1**: The two slip patches merge without instability in the slip patches.
- **Mechanism 2**: The two slip patches do not merge. The shallower slip patch becomes unstable. This happens if the two slip patches have a relatively larger distance and the instability of the upper slip patch does not result in the merging with the deeper patch.
- **Mechanism 3**: The two slip patches merge while the shallower slip patch is unstable. This is more likely if the patches have less distance in between them.

Van den Bogert (2018) report that the magnitude of the seismic moment increases with thickness, except for when mechanism 2 is effective. He further elaborates that the seismic moment does not depend on reservoir thickness for small normalized offsets. The study by Van den Bogert (2018) is done based on dynamic simulation of rupture while the semi-analytical method used here is based on quasi-static formulations. Moreover, here the coupling between patches, which becomes important a large fault throws (i.e. fault throw larger than 80% of the reservoir thickness) [95], has not been taken into account. Therefore it is not possible to compare the mechanisms reported by Van den Bogert (2018) to those effective here and a conclusion cannot be made regarding the comparison of the results.

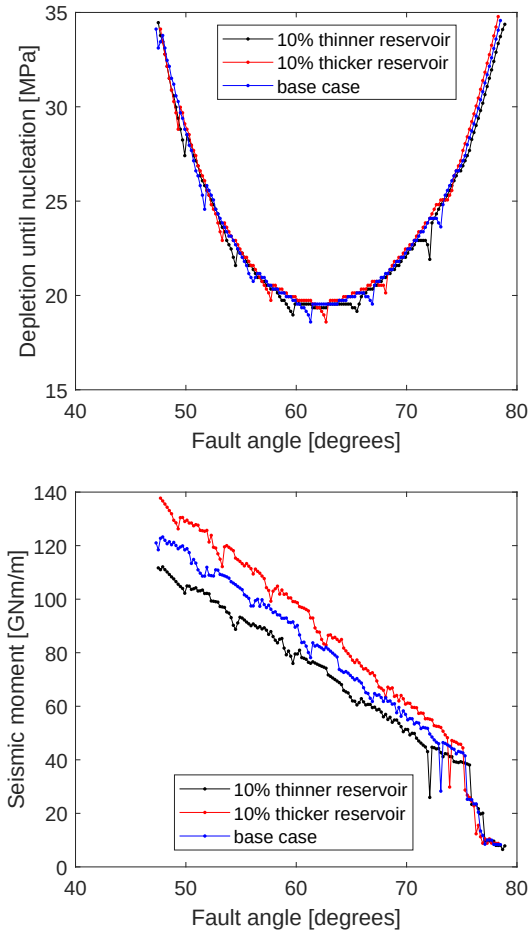

Figure 4.48.: Nucleation pressure and magnitude of the seismic moment for reservoirs with various thicknesses and the same fault throws.

The sensitivity study is taken a step further to study the effect of reservoir thickness while maintaining the normalized offset. The change considered in thickness in the report by Van den Bogert (2018) is about 15%. The same change is considered for the setups in this study. The considered values for the reservoir are shown in Table 4.6. With these values, the normalized offset remains at 33.3% with thickness altered by 15%.

Figure 4.49 shows the results for the setups of Table 4.6. A fault angle of 70 degrees is considered. The results are plotted against the normalized offset, instead of the fault angle (as in Figure 4.48). These figures show that the magnitude of the seismic moment and the nucleation pressure do not have meaningful differences for the various thicknesses. Both parameters remain unchanged.

Table 4.6.: Considered cases for the study of the effect of reservoir thickness while maintaining the normalized offset

Case	Change in thickness [%]	h_1 [m]	h_2 [m]
Base case	0	150	75
Thinner reservoir	-15	127.5	63.75
Thicker reservoir	+15	172.5	86.25

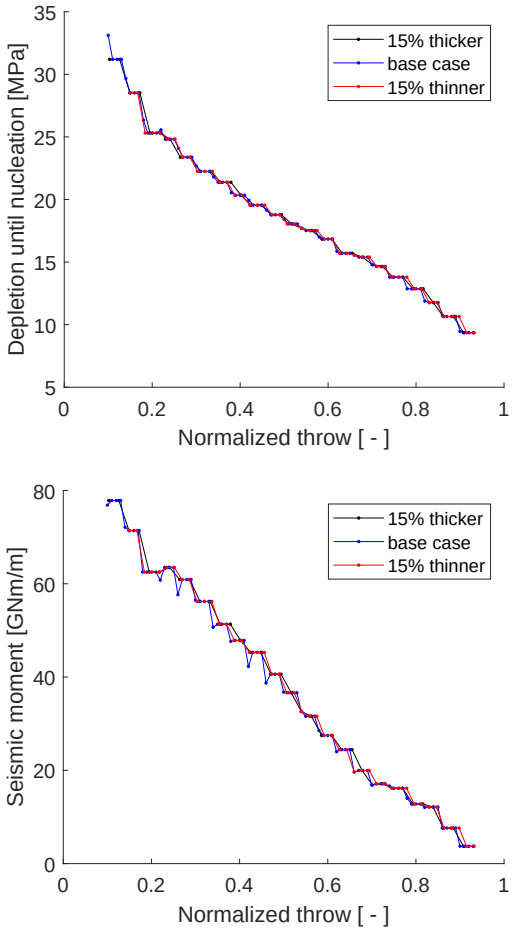

Figure 4.49.: Nucleation pressure (top) and the magnitude of the seismic moment (bottom) versus normalize throw for the test cases of Table 4.6. Fault angle is 70 degrees.

4.3.5. UNSTABLE INITIAL IN-SITU STRESSES

It is observed in many of the results of the sensitivity analysis that simulations do not continue over the entire range of the sensitivity parameter. This is seen for example, in Figure 4.45. In this figure, the nucleation pressures are not estimated for the lower range of the friction coefficient (i.e. 0.3) considered for all sensitivity study test cases. The plot for the 50 degree fault ends before reaching a dynamic friction coefficient of 0.37.

The possible reasons for this are explained earlier in Section 2.7. One reason is the existence of high initial in-situ stresses. When the initial in-situ stresses are high enough to result in a positive Coulomb stress, the system is unstable.

In this section, this is studied through simulations using the semi-analytical approach. The setup of Figure 2.4 is assumed. The initial stresses in the system are calculated for various fault angles and friction coefficients. The lowest friction coefficient, for which the system is initially stable is determined. All properties, besides the fault angle and the friction coefficient are taken as in Table 4.1. The governing friction law consists of only a static friction coefficient, i.e. no slip weakening is considered.

An angle range between 30 to 90 degrees with increments of 1 degree is considered. The friction coefficient is altered between 0.1 to 0.7. The slip threshold is calculated according to Equation 2.32 and compared with shear stresses calculated using Equation 2.15.

For each fault angle, the smallest friction coefficient before which slip occurs is taken as the limit for stability of in-situ stresses. The results are shown in Figure 4.50. This figure demonstrates that in the 30 to 90 degree range, faults with shallower angles and larger ones can maintain stability even with smaller friction coefficients. For the 50 to 60 degrees, instability occurs even at higher friction coefficients close to 0.35. The near vertical (i.e. $\theta \sim 90$ degrees), the fault does not slip even for the smallest friction coefficient considered.

The results of Figure 4.50 can be used to justify the lack of results for the lower range of the friction coefficient in Figure 4.45 where the total friction coefficient drops to values close to, but not exactly approaching 0.3, for the considered fault angles.

4.4. HYBRID METHOD FOR QUASI-STATIC SIMULATION OF RUPTURE IN MULTI-FAULT POROELASTIC SYSTEMS

The semi-analytical method is used in the previous chapter to find the onset of fault nucleation and to determine a magnitude for the seismic moment of the resulting earthquake. However, no results could be extracted from the semi-analytical model for post-nucleation. The semi-analytical method has the limitation that it can only be used for simulation of fault slip and stresses up to the nucleation point. If there are many faults involved, the simulation would only progress until the first fault nucleates.

Furthermore, fault to fault interactions are not honored in the semi-analytical approach. When a fault nucleates, it can create a large rupture.

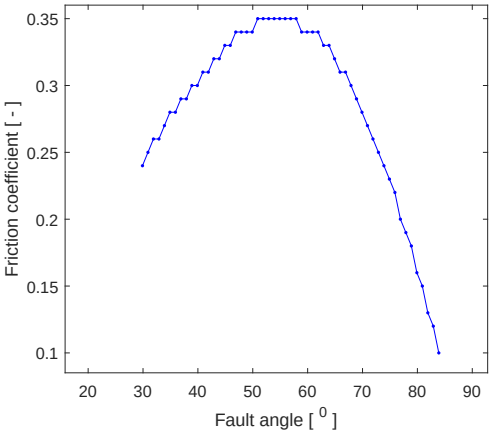

Figure 4.50.: The minimum friction coefficient to ensure stability for various fault angles for the setup of Figure 2.4. Other data is as shown in Table 4.1.

This large rupture can affect the stress field. In the semi-analytical method, the neighboring faults do not observe this effect.

Given that fault to fault interaction is not observed in the semi-analytical solution, the sensitivity analysis of the previous section is performed by considering a single fault in the reservoir. The presence of others faults would not have affected the results for the studied fault.

The hybrid method is developed to address the above-mentioned issues. This method makes assumptions regarding the post-nucleation frictional behavior of an activated fault and simulates the system after the seismic event. Furthermore, the fault to fault interactions would be honored as the hybrid method adjusts the stress fields numerically following the nucleation of a fault assuming quasi-static behavior.

In this section, the results of the hybrid approach are presented. The results are shown for the case of considering two faults and later extended to a more realistic test case relevant for the Groningen field.

When there is one fault in the system, the results of the method are the same as the semi-analytical approach prior to fault nucleation. The reason is that the hybrid method uses the numerical stress calculations only after a fault nucleates. Furthermore, once a fault nucleates, it will alter the stress field of the system. The effect of the rupture of a fault influences other faults in the system.

It is also important to mention that there are dynamic effects during rupturing (stress waves traveling through the rock) which would require a full dynamic simulation to capture them correctly [102]. The hybrid method proposed here is a simplified approach based on a quasi-static post-slip rupture configuration governed by the dynamic friction coefficient.

4.4.1. POST-NUCLEATION BEHAVIOR OF A SINGLE FAULT

In this section, a single fault is modelled. The purpose of this is to demonstrate the post-nucleation rupture profiles.

The post-nucleated rupture profiles are calculated by assuming a dynamic friction coefficient for the fault at the post-nucleation depletion pressure. For this reason, the rupture profiles are expected to be large.

As mentioned earlier, the post-seismic rupture-induced stress effects are not incorporated for the fault itself. This is the case here, the influence of the rupture on the stress in the matrix cells neighbouring the fault, is not assumed to affect the propagation of the rupture. The growth of the rupture is instigated by stresses resulting from depletion and initial in-situ conditions that were outlined in Section 2.5.2.

A 70 degree fault in a reservoir with an offset as shown in Figure 2.4 is considered. A linear slip weakening friction law is assumed for the fault. The values used for this setup are as shown in Table 4.1. The system is initialized as described in Section 2.5.2, and depleted as explained in Section 2.5.3. A 300×300 mesh is used for the matrix. There are 69 elements along the fault. The mesh is coarser than the semi-analytical method. The reason is that the numerical calculation of stresses over the entire mesh makes the hybrid method slower than the semi-analytical method. In order to keep run-times in an optimum range this coarser mesh is chosen in this section.

Figure 4.51 shows the slip patch before nucleation for depletion pressures up to 24.1 MPa, and the rupture profile following nucleation and on-wards. The fault nucleates at a depletion pressure of 25.5 MPa. This figure shows that following nucleation, a single large patch forms. With increasing depletion past nucleation, the size of the slip patch grows steadily. In previous results where a slip weakening friction law was used, for example Figure 4.35, the post-nucleation rupture could not be simulated. The simulations would stop at the point of nucleation.

Figure 4.51 also shows the Coulomb stress profiles corresponding to the same depletion pressures of the plotted slip profiles. In the hybrid method, the post-nucleation stresses are calculated numerically using the sEFVM. It is seen in this figure that due to the embedded nature of the sEFVM, the stress profiles have a small kink close to y=150ms. Such oscillations do exists in this figure and other results using the sEFVM, but they are minor in magnitude and do not create large deviations in the stress profiles considered in this study. If a finer mesh is selected, these deviations will diminish and the curves will be smoother. Stronger smoothing of the profiles is possible.

4.4.2. RUPTURE-INDUCED STRESS PERTURBATIONS IN MULTI-FAULT SYSTEMS

In this section the one fault setup is extended to multiple faults. When another fault is present in the system, the nucleation and consequent rupture of one fault will affect the other fault via the rupture-induced perturbations in the stress field. This effect is investigated in two-fault systems to study the magnitude of this effect.

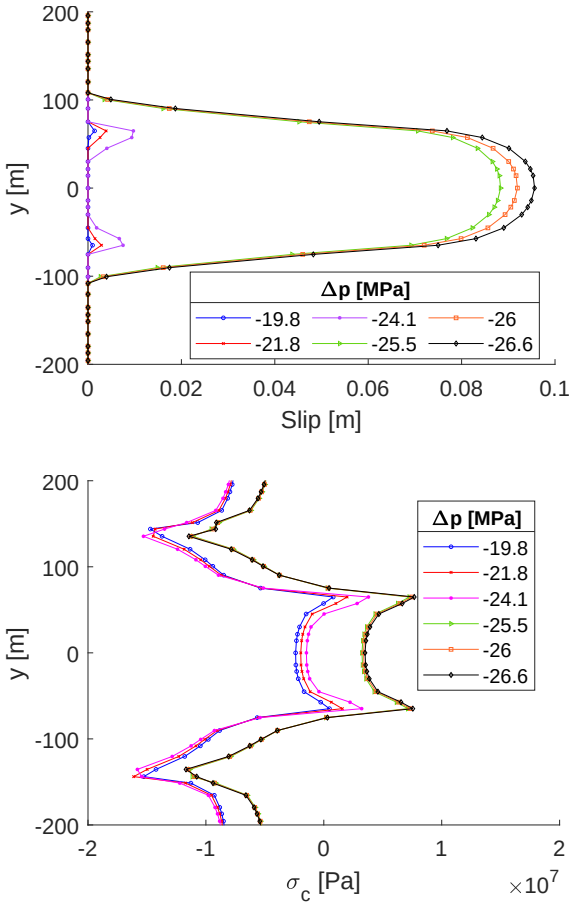

Figure 4.51.: The aseismic slip patch and the post-seismic rupture development under quasi-static assumptions for a 70 degree fault (top) and the corresponding Coulomb stress profile (bottom)

.

In the hybrid method developed here, the Uenishi and Rice (2003) criterion of Equation 2.33 is used to determine the nucleation pressure in the faults. However, this criterion was developed for a single slip patch in a single fault [96] and is not necessarily valid for multi-fault system. This indicates that although the effect of rupture of a fault on other faults is simulated, the criterion for obtaining the nucleation pressure is not expected to be accurate. The validity of this criterion for such cases requires further research. In the first example, two faults are considered

with different angles. A 70 degree fault similar to the previous sections (with details outlined in Table 4.1) and a 75 degree fault. The reservoir geometry and other properties besides the fault angle are similar.

Figure 4.52 shows a schematic of the setup. Despite the change in the reservoir geometry, reservoir thickness, offsets and other properties are kept similar to values in Table 4.1.

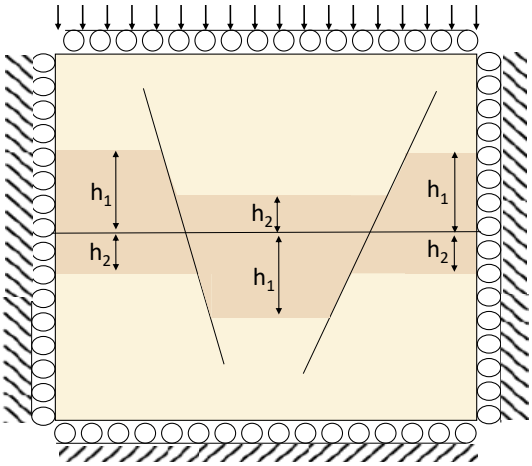

Figure 4.52.: Setup for faulted system with an offset

The exact locations of the faults are as shown in Table 4.7.

Table 4.7.: Location of 70 degree and 75 degree fault with x and y in the range between 0 m to 4500 m.

Fault	x_1 to x_2 [m]	y_1 to y_2 [m]
70° fault	1739.7 - 1860.3	2475 - 2025
75° fault	2618.1 - 2781.9	2025 - 2475

From the results of the sensitivity analyses on fault angles (shown in Figure 4.39), the 70 degree fault will nucleate at a lower depletion pressure than the 75 degree fault. The nucleation pressure of the 75 degree fault can therefore be influenced by the post-nucleation rupture of the 70 degree fault. In this section, this influence is studied to see how the rupture of the 70 degree fault can postpone or advance the nucleation of the 75 degree fault.

Simulations for the considered geometry results show that the 70 degree fault nucleates at 24.1 MPa. The 75 degree fault nucleates at 31.2 MPa. This indicates that with increasing depletion, the 70 degree fault will enter seismic rupture phase. To study the effect of this rupture on the 75 degree fault, two cases are simulated:

- **Case 1**: The seismic rupture of the 70 degree fault will perturb the stress field via changes in the stresses in the surrounding matrix. This effect is incorporated when calculating the stresses affecting the 75 degree fault.

- **Case 2**: The seismic rupture of the 70 degree fault does not influence the local stress field. In this case the faults are invisible to each other.

The results for both cases show that the calculated nucleation pressure does not change. To observe if there are other minor influences, the slip patch profile for the 75 degree fault is analyzed for case 1 and 2. This is shown in Figure 4.53. This figure shows that the slip profile of the 75 degree fault is affected but the magnitude of the effect is very small. At the nucleation pressure of the 75 degree fault, the maximum slip for Case 1 is 70.42 mm and for Case 2 it is 69.98 mm. This effect is too small to influence the calculated nucleation pressure.

The plots of Figure 4.53 are not as smooth as previous results. This is because, based on the extension considered for the fault (described in Table 4.7) and the mesh over the entire domain (300×300), there are 39 and 41 fault nodes on the 75 and 70 degree faults, respectively. Also only a small section of the fault slips, therefore only a few nodes are involved. These result in coarser images.

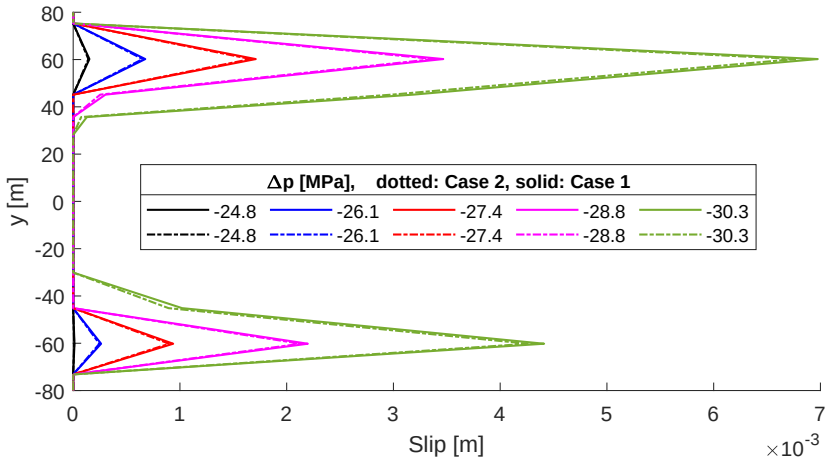

Figure 4.53.: Slip profiles for the 75 degree fault after nucleation of the 70 degree fault for faults with the locations defined in Table 4.7.

To analyze the magnitude of the effect better, the location of the faults are changed. It is expected that the distance between the faults influences the results. For the setup of Table 4.7, the distance between the faults at the center line (i.e. y = 2250 m) is 900 m. This is reduced to 500 m. The fault new locations are given in Table 4.8

The results for the nucleation pressure show that for both cases, the nucleation pressure for the 70 degree fault is 27.9 MPa. This is different from the previous situation where the faults were farther apart. The reason behind the change is assumed to be the change in the geometry of the depleting reservoir. The offset in the reservoir at the location of the 75 degree fault is now closer to the 70 degree fault.

Table 4.8.: Locations for the 70 degree and 75 degree faults with 500 m of distance at center line.

Fault	x_1 to x_2 [m]	y_1 to y_2 [m]
70° fault	1939.7 - 2060.3	2475 - 2025
75° fault	2418.1 - 2581.9	2025 - 2475

This affects the 70 degree fault. The nucleation pressure for the 75 degree fault changes for cases 1 and 2 but not largely. The 75 degree fault nucleates at 31.11 MPa for case 1 and at 31.14 MPa for case 2. Figure 4.54 shows that prior to the rupture of the 70 degree fault (i.e. at depletion pressure of 27.9 MPa) the slip patches are identical for cases 1 and 2. After seismic rupture of the 70 degree fault, there is a minor influence on the 75 degree fault.

Another observation in Figure 4.54 is that the lower slip patch is larger than the top patch. This is different from the simulations considered so far. Furthermore, the value of the slip is larger than in the case of the fault that were 900 m apart. These effects are due to the geometry of the reservoir shown in Figure 4.52. It is seen in this figure that the deeper offset points are closer in distance than the shallower offset points. This results in a larger effect of the deeper slip patches one each other when the rupture induced stress perturbations are taken into account. This results in the deeper slip patches demonstrating larger sizes.

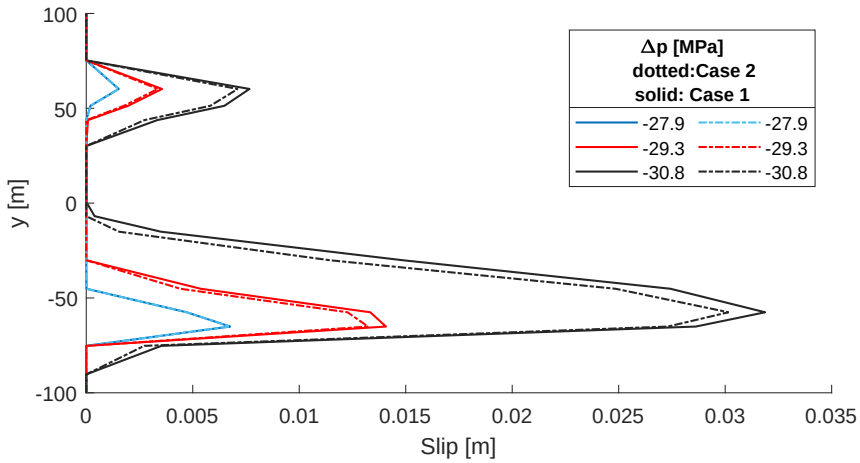

Figure 4.54.: Slip profiles for the 75 degree fault after nucleation of the 70 degree fault for faults with the locations defined in Table 4.8.

The results are repeated with 250 m of distance between the fault at center line (i.e. y = 2250 m). The coordinate for the faults are shown in Table 4.9.

The results show that the nucleation pressure for the 70 degree fault is 27.9 MPa and for the 75 degree fault it is 32.3 MPa for case 1 and 32.6 MPa for case 2. The slip patch profiles for the 75 degree fault are shown in Figure 4.55.

Table 4.9.: Locations for the 70 degree and 75 degree faults with 250 m of distance at center line

Fault	x_1 to x_2 [m]	y_1 to y_2 [m]
70° fault	2109.8 - 2190.2	2475 - 2025
75° fault	2295.4 - 2404.6	2025 - 2475

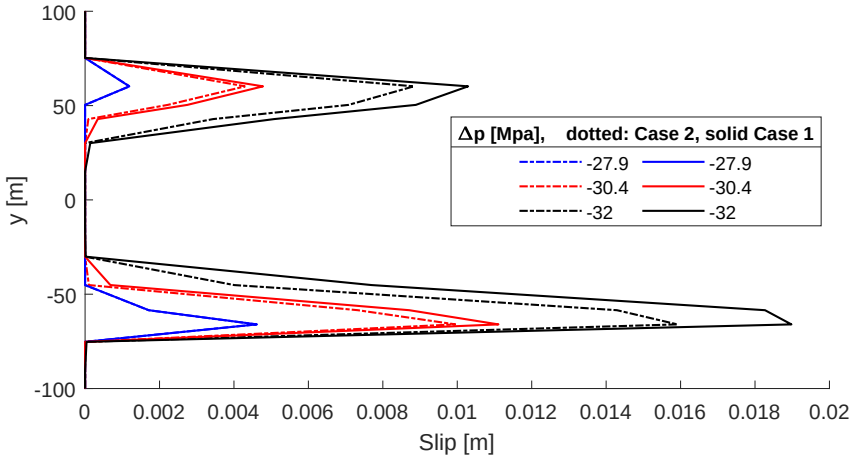

Figure 4.55.: Slip profiles for the 75 degree fault after nucleation of the 70 degree fault for faults with the locations defined in Table 4.9.

4.4.3. SIMULATION OF A REALISTIC TEST CASE RELEVANT TO THE GRONINGEN FIELD

A test case relevant to the Groningen field is used in this section to showcase the applicability of the hybrid model for the simulation of relevant field test cases.

This test case was extracted from a geomechanical model created for the Groningen field. Details of this model are given in Appendix C. The 2D map is taken as shown in Figure C.8.

MATLAB is used to read and re-scale Figure C.8 image based on the selected mesh-size [119]. The mesh size in this example is 361×361.

The analytical method that is the basis of the hybrid scheme is not capable of considering the effect of heterogeneity in the geomechanical constants. For this reason, geomechanical constants are considered as shown in Table 4.1.

This simplifies the model created for this study. The initial intention of creating detailed geomechanical models of the Groningen field is for numerical simulations using the sEFVM. Given the accuracy limits of the sEFVM, this method could not be used to its full potential. However, we use it's relevant geometry to demonstrate a more realistic application of the hybrid method.

The geometry of the system is adjusted. This adjustment is to ensure that fault locations are placed at the offset locations. Furthermore, there can be minor changes in thickness along the reservoir layer which can affect the calculations. Given that a change in reservoir thickness across a fault is geologically highly unlikely, this is also adjusted. This is in agreement with what is expected in geological formations of depositional origins. It such settings, it is expected that the thickness does not change across a fault [126].

The model is simulated assuming initialization and boundary conditions similar to what was described in Section 2.5.2 and Section 2.5.3.

All faults are assumed to follow a linear slip-weakening regime. The static friction coefficient is 0.6 and the dynamic friction coefficient is 0.4. The critical slip distance is 0.02 m.

The pressure distribution was defined such that the center-line of the reservoir has a pressure of 35 MPa. This is shown in Figure 4.56. This image also focuses on a series of 10 faults for which an analysis will be made here.

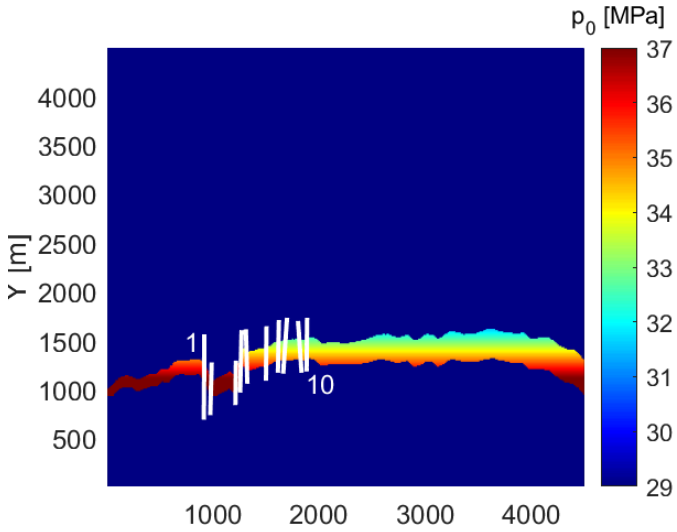

Figure 4.56.: Initial pressure distribution of the reservoir and location of the faults. The reservoir is the only poroelastic region inside the elastic domain.

Depletion is simulated down to full depletion where the center line pressure declines by 35 MPa. This results in reactivation of some of the faults. The results indicate that faults number 1, 3, 4 and 6 nucleate.

Figure 4.57 shows the rupture-induced perturbations in the von Mises stress field.

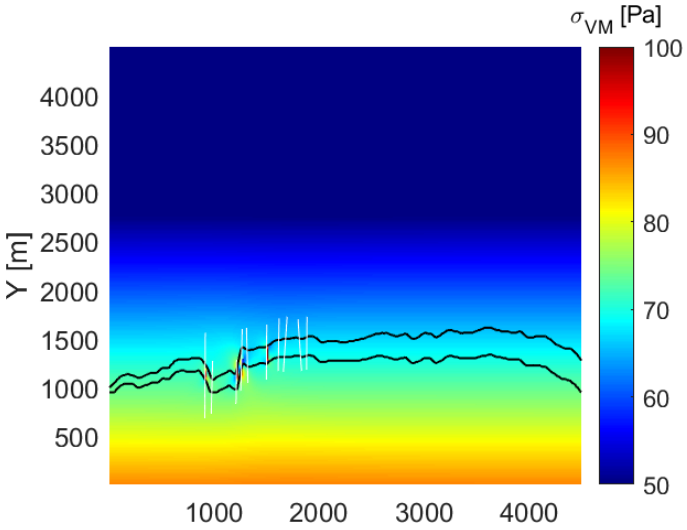

Figure 4.57.: Perturbations in the local stress field as a result of fault rupture. Faults are shown in faded color to allow for better demonstration of their locations and the changes to the stress map.

Using the hybrid method with the effect of rupture perturbations, faults 1, 3, 4 and 6 nucleate at depletion of 32.4 MPa, 26.6 MPa, 25.8 MPa and 30.8 MPa. In the case without the effect of perturbations, fault 4 nucleates first at 25.5 MPa, followed by fault 3 at 26.0 MPa, fault 6 at 30.2 MPa. This demonstrates the slight effect from rupture of a fault on nucleation of neighboring faults given the limitations of the quasi-static approach and the use of the Uenishi and Rice (2003) stability criterion [96].

Figures 4.58 through 4.62 show the slip profiles for faults 1 to 10 from the setup shown in Figure 4.56. These figures show situations where the fault does not slip at all, the fault does slip but it does not reach nucleation, and the fault reaches nucleation and the rupture continues to propagate.

Figure 4.63 shows the change in the displacement field following fault rupture. This plot is created by calculating the difference between the post-depleted deformation state and the final deformation field after 35MPa depletion.

Figure 4.63 shows that there are minor change in matrix displacements. This is in the order of nanometers. This displacement occurs near faults which nucleate. These were faults 1, 3, 4 and 6.

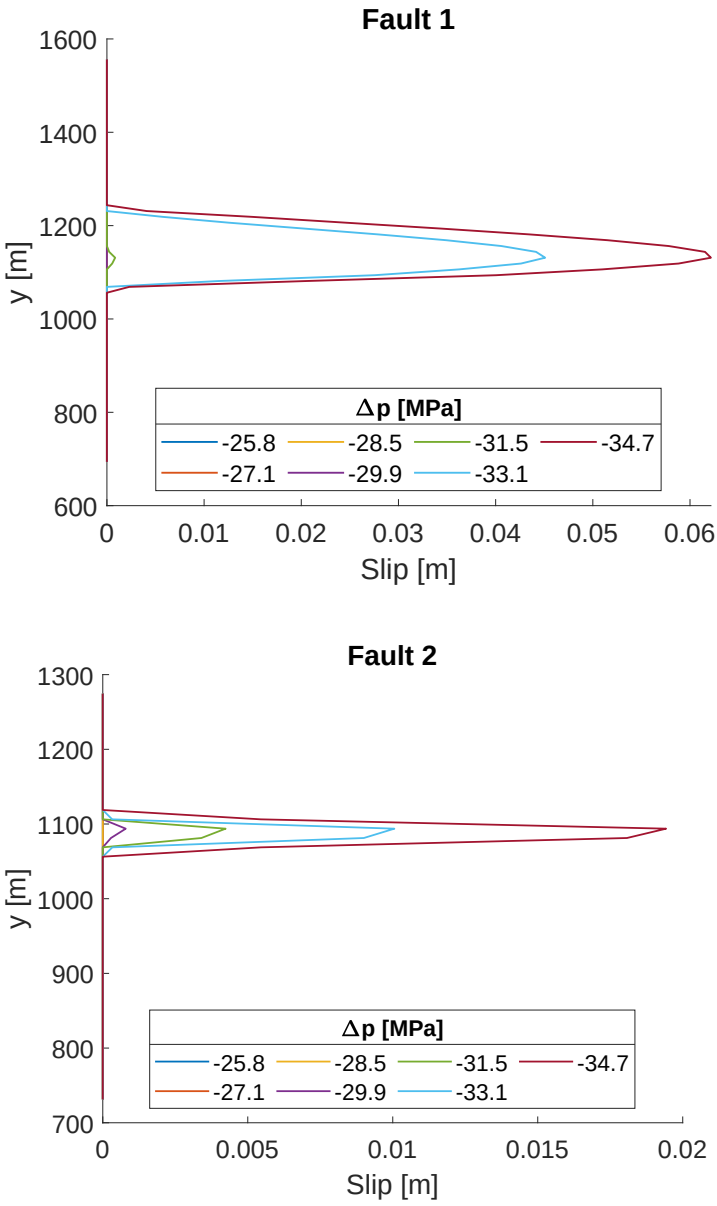

Figure 4.58.: Slip patches corresponding to faults 1 (top) and 2 (bottom) from the setup of Figure 4.56. Fault 1 nucleates at a depletion pressure of 32.4 MPa. Fault 2 does not nucleate. For this fault, the slip patch begins to grow at the shallower offset point.

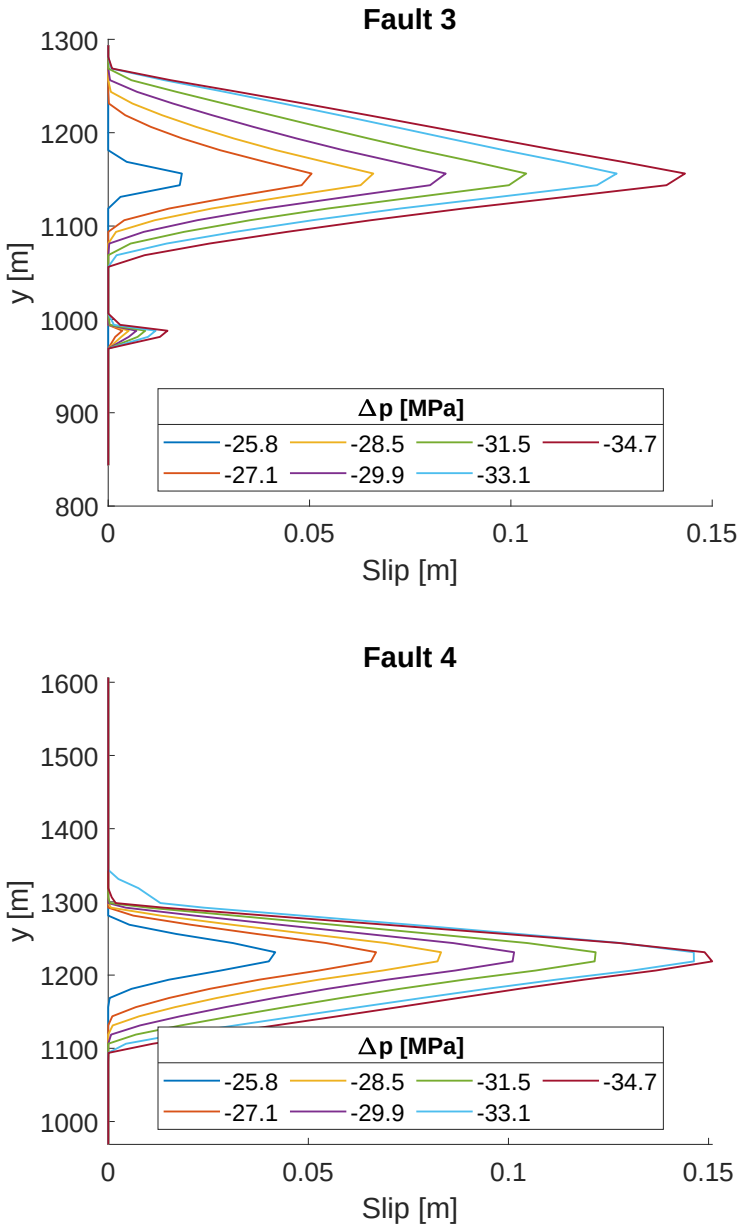

Figure 4.59.: Slip patches corresponding to faults 3 (top) and 4 (bottom) from the setup of Figure 4.56. Fault 3 nucleates at a depletion pressure of 26.6 MPa. The two slip patches show there are two peaks. In between the peaks there is nonzero slip values with very small magnitudes. Fault 4 nucleates at a depletion pressure of 25.8 MPa and a single larger slip profile grows after this pressure.

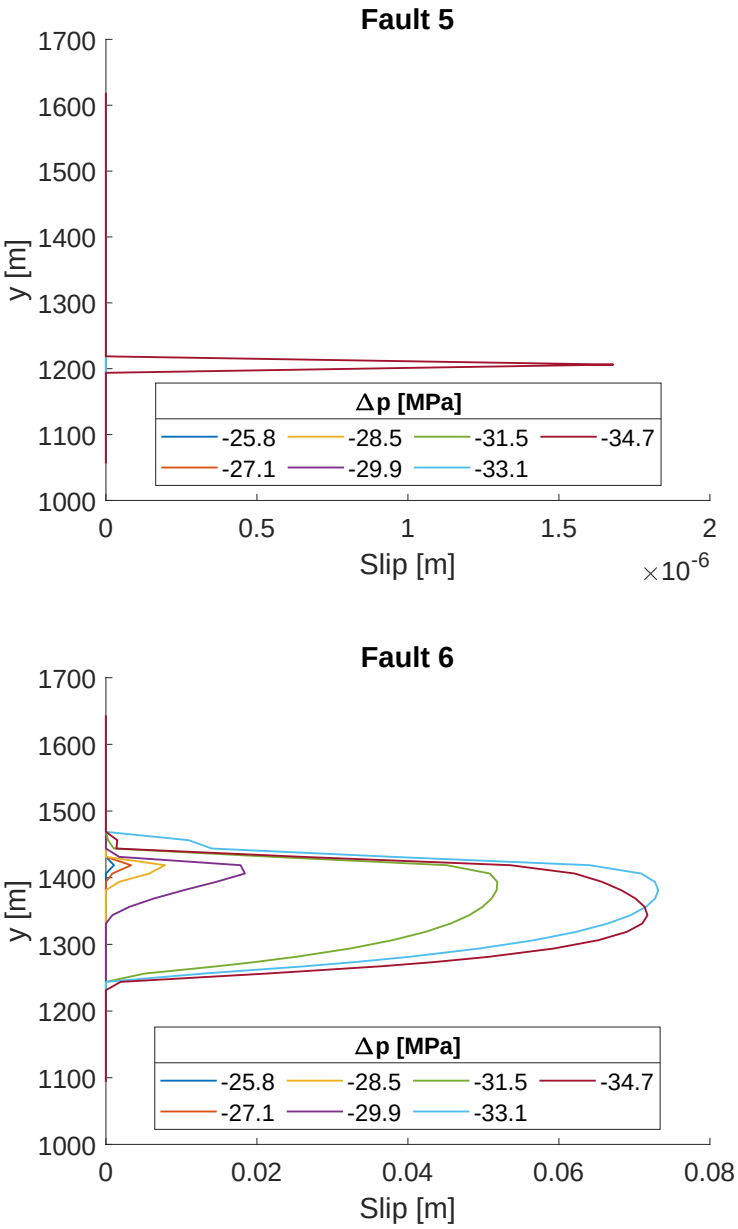

Figure 4.60.: Slip patches corresponding to faults 5 (top) and 6 (bottom) from the setup of Figure 4.56. There is a small slip patch forming in the deeper offset location of fault 5 which does not reach nucleation. The slip patch for fault 6 begins to form in the shallower offset point. This fault nucleates at a depletion pressure of 30.8 MPa. Following nucleation a single large rupture profile forms and grows.

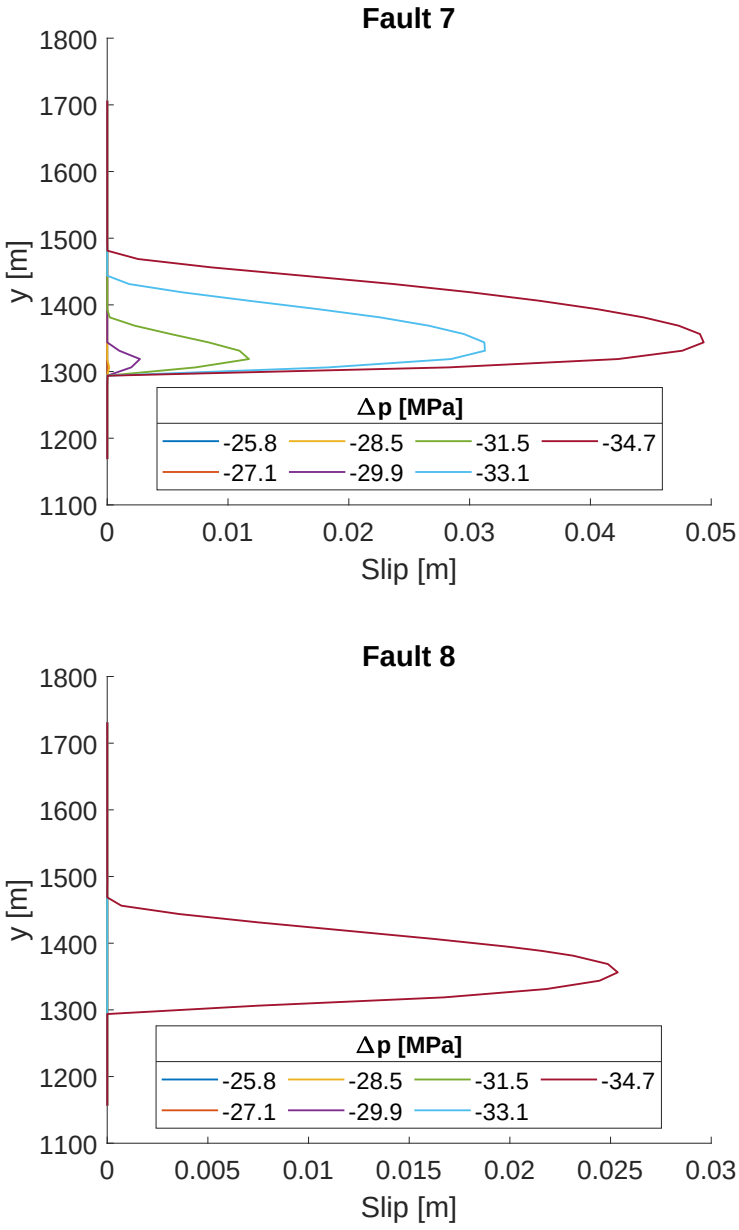

Figure 4.61.: Slip patches corresponding to faults 7 (top) and 8 (bottom) from the setup of Figure 4.56. Both faults slip but neither nucleates.

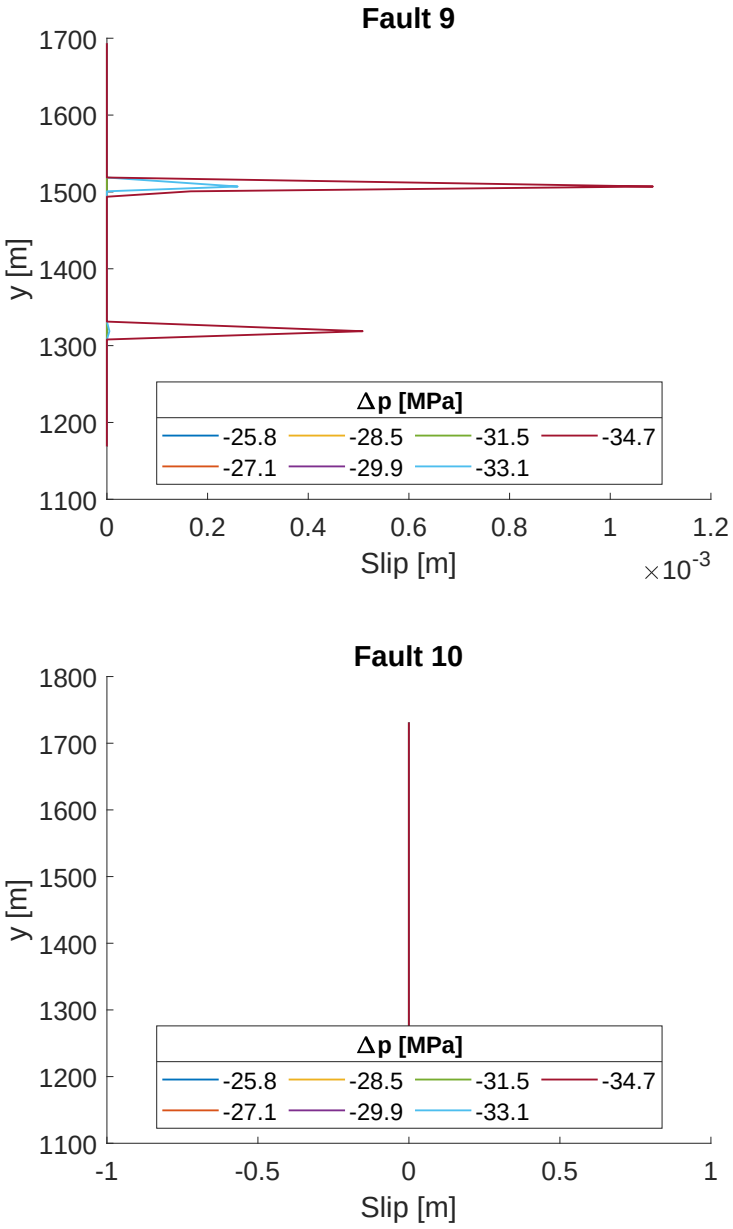

Figure 4.62.: Slip patches corresponding to faults 9 (top) and 10 (bottom) from the setup of Figure 4.56. Fault 9 does slip but does not reach nucleation. Fault 10 is stationary throughout the depletion with zero slip.

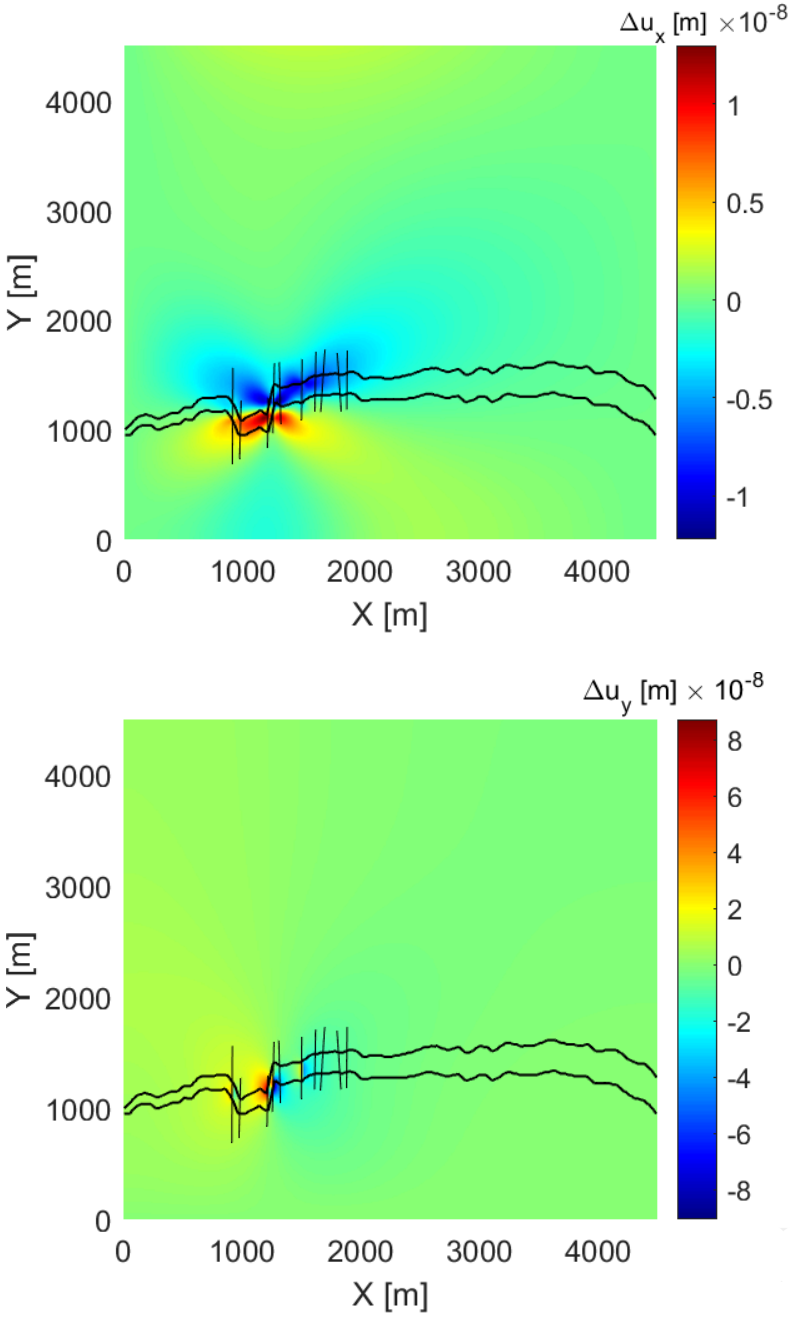

Figure 4.63.: Perturbations in the horizontal displacement field (top) and vertical displacement field (bottom) due to fault rupture for the setup of Figure 4.56. This figure shows change in the matrix displacement field in the order of a nanometers due to fault nucleation and subsequent rupture.

5

CONCLUSIONS AND RECOMMENDATIONS

5.1. CONCLUDING REMARKS

Induced seismicity refers to earthquakes that are triggered or induced by human activities, for example fluid injection or extraction related to oil and gas activities. The importance of understanding induced seismicity lies in its potential impact on safety, infrastructure, and the environment.

The Groningen gas field is the largest gas field in Europe that has been producing for a remarkable period spanning over 6 decades. With increased depletion in the Groningen field, the number and intensity of earthquakes in the region increased. Studies showed that these seismic events are correlated with gas production. Eventually, the seismic events lead to production cuts and plans for full field shut-down as per 1 October 2024.

The current research, inspired by the challenges of induced seismicity in the Groningen gas field, attempts to develop computational methods for large-scale simulation of fault reactivation in heterogeneous, heavily-faulted poroelastic media.

In the expansive domain of geomechanics, numerous computational methods exist to simulate such complex geological settings. However, our attention in this research is particularly directed towards finding appropriate simulation techniques suited for simulation of fault reactivation in faulted poroelastic media. This deliberate focus guided our method selection, ensuring that the computational approach chosen aligns well with the unique characteristics and challenges presented by the heterogeneous, heavily-faulted poroelastic reservoir under investigation.

In the first attempt, a finite-volume based embedded numerical method is chosen. This selection is based on the following lines of reason:

- The finite volume method is used for discretising the equations for flow and mechanics. The choice of finite volume is to calculate the mass and stresses to be locally conservative.

- The domain of interest is a heavily faulted media. This gave weight to the idea of using a computational method which relies on embedded meshing for the faults. In the embedded method used here, a staggered grid is considered for pressure and displacement. The mesh for the matrix does not conform to the faults. The faults are gridded independently with one additional degree of freedom per fault element inside each matrix grid block.

- The scale of the simulation is field-scale. This motivates the use of a method that is computationally efficient. Bi-linear basis functions are chosen for the finite volume approach. These bi-linear functions are relatively easily integrated and differentiated analytically over the control volumes. This eliminates the need for numerical differentiation and integration in the implementation of the method.

The sEFVM is developed based on the framework suggested by Deb and Jenny (2017) for the XFVM [65]. The name "enhanced" is used in this study instead of "extended", i.e. sEFVM instead of XFVM. This does not suggest that the sEFVM is an entirely new method and only aims to differentiate between the finite volume method and the extended finite element method, i.e. XFEM [63]. Some variations in implementation between the XFVM and sEFVM exist and these are outlined in this chapter.

In EFVM, fault displacement (i.e. the slip) is included in the finite-volume basis functions with the use of a modified form of the Heaviside function. The EFVM method is tested for order of accuracy and compared with known cases with analytical solutions (Terzaghi and Mandel [101]) and an available simulator for fractured and deformable porous media (Porepy) [118], and another finite-volume based numerical simulator (collocated FVM [112, 121]). It is observed that the slip and stress profiles have oscillations for certain test cases. These oscillations would be problematic for situations where faults are closer to the threshold for slip. To assist with this, a post-processing smoothing step is added. Furthermore, it is observed that slip should be found in a sequentially implicit order. This would mean to estimate which nodes slip according to the stresses on the fault, find the slip and check to ensure the estimate is correct. The final development is called the Smoothed Enhanced Finite Volume Method or sEFVM. sEFVM is a fully coupled fully implicit solver which shows high promise for modeling deformation, pressure and slip in heterogeneous faulted poroelastic media. This method is quite fast and relatively efficient to implement [99].

However, sEFVM has limited accuracy in the simulation of slip profiles in problems with a discontinuous stress profiles. These are common for the cases of faulted, depleted reservoirs with offsets. One of such test cases is modelled. In the setup, a fault cuts across a depleting reservoir with an offset. Analytical solutions for calculating the stresses and the slip along the fault undergoing depletion exist [80, 95]. These analytical solution show that the shear stress profile is discontinuous with infinite peaks corresponding to the reservoir offset points. The infinite peaks are not captured closely by sEFVM and this poses a challenge when estimating the slip profile [112].

Given the precision of the analytical method in capturing the discontinuities, a semi-analytical method is developed next. The available analytical expressions are extended to be solved over the sEFVM computational domain. This allows for accurate estimation of stress and slip over the faults. The semi-analytical approach relies on simplification of the heterogeneities, but it could capture the growth of the slip patch profiles with depletion in the field. The results are used to find the onset of nucleation for seismic slip and seismic moments for the considered configurations relevant to the Groningen gas field.

The semi-analytical method is much faster than sEFVM because in sEFVM, large systems of equation are being solved in a fully coupled fully implicit manner. This is a computationally expensive step. Another reason is that the semi-analytical solver does not solve for unknowns in the entire mesh, it finds depletion-induced stresses affecting the fault and the consequent slip profile based on the cells undergoing depletion and cells along the fault. Note that this makes it somewhat like a boundary element method (BEM).

Given the superior computational efficiency and precision of the semi-analytical method, it is used to perform a sensitivity analyses on the most influential parameters in the study of induced seismicity in the Groningen field. These parameters are identified from literature as the fault angle, fault throw, frictional properties and reservoir thickness. The goal of this evaluation is to demonstrate the applicability of the semi-analytical method to a wide range of systems. Another intention is to provide further insight into the simulated behaviors under various configurations of the system. The findings of the sensitivity analyses are analyzed and where possible, compared with other reports. Previous studies by van den Bogert [76, 77], Buijze [102] and Buijze et. al. [72, 78, 106] collectively provided invaluable insights into the identification of critical sensitivity parameters and their anticipated impact on induced seismicity. The findings of these studies were compared with the results obtained from the sensitivity analysis performed using the semi-analytical method. A brief summary of the results of the sensitivity analyses is as follows:

- The effect of fault angle on induced seismicity is studied for a wide range of fault dip angles between 30 to 90 degrees. This analysis shows that the shallowest and steepest fault angles which are reactivated, nucleate latest and at higher depletion pressures. The mid-range fault angles between 55 to 75 degrees more readily nucleate at lower depletion pressures. This study shows that the magnitude of the seismic moment is higher for shallower fault angles.
- The study of fault throw shows a decrease in the magnitude of the seismic moment with increasing offset. However, faults with higher offsets nucleate at lower depletion pressures.
- The frictional behavior of the faults is also studied. The static friction coefficient is altered while maintaining the dynamic friction coefficient and critical slip distance values. The results show the magnitude of the seismic moment increases with increasing friction coefficient for all fault angles. Faults with higher static friction coefficients nucleate later, at higher depletion pressures.

- Stronger slip-weakening friction laws are studied by considering a range for the dynamic friction coefficient while maintaining the static friction coefficient and the critical slip distance. It is shown that nucleation occurs at smaller depletion pressure when dynamic friction coefficient is smaller. The corresponding magnitude of the seismic moment is larger for smaller dynamic friction coefficients.
- In another set of simulations, the slope of the linear slip weakening relationship is maintained while changing the dynamic friction coefficient and the critical slip distance. These simulations show a decrease in the magnitude of the seismic moment with increase in the dynamic friction coefficient. The change in the nucleation pressure is unaffected by the friction coefficient at first but later shows an increase with increasing dynamic friction coefficient.
- Reservoir thickness does not affect the nucleation pressure. Reservoir thickness has a weak effect on the magnitude of the seismic moment. Thicker reservoirs have slightly higher magnitude of the seismic moment.
- The sensitivity analyses unfold cases where a run-away rupture can occur. This is studied by simulating a range for the static friction coefficient and fault angles while observing the initial in-situ stresses. This analysis provides a minimum range for the friction coefficient, after-which instability occurs.

An important element of the semi-analytical and hybrid approaches is the use of the Uenishi and Rice (2003) stability criterion [96] for the nucleation length, and the associated nucleation pressure, of a fault. This criterion is only valid for one fault with a single slip patch. It was observed in the results of the sensitivity analysis, that for the case of faults with offsets larger than a threshold (80% for the base case parameters), the results of the semi-analytical method become unreliable. Furthermore, the use of this criterion was considered for multi-fault setups. This is also expected to include errors as validity of the Uenishi and Rice (2003) for multi-fault systems is uncertain.

The semi-analytical method could is used to simulate fault slip before fault nucleation. In a multi-fault setup, means the simulation only continues until the first instance of nucleation is observed. This inhibits the use of the semi-analytical method for more practical test cases. This motivates the extension of the semi-analytical model to the hybrid method.

The hybrid method is an extension of the semi-analytical method and sEFVM. The hybrid method assumes the nucleated fault has a friction coefficient equivalent to the dynamic friction coefficient. Following nucleation, the nucleated fault slips according to this lower friction coefficient. This can result in large slip patches for the nucleated fault. This large slip patch can potentially alter the stress field far enough to affect other faults. In the hybrid method, these post-seismic stress perturbations are incorporated numerically using sEFVM. These perturbations and their effect on the fault slip and nucleation are analyzed.

It should be noted that also the hybrid model uses the Uenishi and Rice (2003) for the determination of the nucleation length [96].

However, this criteria is only valid for a single slip patch in a single fault. Further research is required to overcome this limitation.

A realistic model for the Groningen gas field is developed based on the seismic velocity model of the Groningen field. A 2D snippet from this model is used to evaluate the applicability of the hybrid method. This example demonstrates its applicability to multi-fault systems.

5.2. SUGGESTIONS FOR THE FUTURE

The following suggestions are made for the continuation of this work:

- An assumption of the semi-analytical and hybrid methods developed in this study is the lack of interaction between the slip patches of a single fault. In reality, the slip patches do influence each other [98]. Numerical simulators already incorporate this effect given the coupling of the stresses in the system. Ignoring the effect of fault patches on each other will result in less accurate predictions when the patches have grown closer. A further development to this work could be the incorporation of slip patch interactions in the underlying analytical expressions embedded in the semi-analytical and hybrid methods. This would then also require a modification of the Uenishi and Rice (2003) stability criterion [96] to make it suitable for multiple patches and multiple faults.

- Another assumption of the semi-analytical and hybrid method was homogeneous geomechanical properties (e.g. Lame constants) throughout the entire system. This is because the underlying analytical expressions were developed based on this simplifying assumption [95]. In future work, analytical expressions which can address the effect of heterogeneity in geomechanical properties can be used to replace the current analytical formulations to allow for more flexibility in introducing layer-dependent heterogeneity in the system.

- The results of the hybrid method showed that the rupture of a fault can influence the nucleation pressure of a neighbouring fault. However, this effect was not thoroughly studied. The magnitude of this effect can be different for various fault angles, distances, orientations etc. The results also demonstrate that the geometry of the reservoir itself (which follows the trend of the faults in terms of the offsets they can have) is an important parameter. A study can be performed to better understand when the effect of a rupture of a fault can be concerning to nearby faults and how large this influence is in the study of induced seismicity.

A

CONVERSION EQUATIONS FOR GEOMECHANICAL CONSTANTS

Geomechanical properties of rock are one of the most important properties that repeatedly appear in equations all throughout this study. These properties are defined with constants. Many geomechanical properties are related to each other. The conversions relevant in this study are shown here. These conversions were reported by [101, 127].

$$G = \varrho_s V_s^2 \tag{A.1a}$$

$$\lambda = \varrho_s V_p^2 - 2G \tag{A.1b}$$

$$K = \lambda + \frac{2G}{3} \tag{A.1c}$$

$$E = \frac{9K\lambda}{3K + G} \tag{A.1d}$$

$$\nu = \frac{\lambda}{2(\lambda + G)} \tag{A.1e}$$

$$K_\upsilon = 2G\frac{1-\nu}{1-2\nu} \tag{A.1f}$$

where ϱ_s is the seismic density, V_s is the seismic s-wave velocity, V_p is the seismic p-wave velocity, G is the shear modulus (also known as the second Lame parameter), λ is the first Lame parameter, K is the bulk modulus, E is Young's modulus, ν is the Poisson ratio and K_υ is the uni-axial vertical stiffness factor.

B

THE GRONINGEN FIELD DATA

This section presents essential data from the Groningen field relevant to the study. It explores the basic geology of the field, detailing the different layers that comprise the overburden, underburden, and the reservoir. The section also includes an overview of the field's pressure history and its future projections. A concise summary regarding the characteristics of faults in the Groningen field is provided. The discussion further addresses the behavior of these faults in terms of friction across the various geological layers.

B.0.1. GENERAL GEOLOGY

The gas producing formation in the Groningen field is the Rotliegend Slochteren sandstone. This formation has a thickness between 150 m to 200 m. The reservoir is overlain by the Basal Zechstein anhydrite-carbonate caprock, which has a thickness of about 50 m. Between the caprock and the Rotliegend reservoir, there is an impermeable overlying layer of claystone called the Ten Boer. The thickness of this layer is between 0 m to 50 m. Above the caprock lies a huge Zechstein salt layer with a thickness between 600 m to 1000 m. Below the reservoir is the source rock which is made of Upper carboniferous shale, silt-stone and coal layers.

The reservoir lies at depths in the range of 2 km to 4 km [7]. The reservoir quality of Rotliegend sediments from the Groningen field has been measured on thousands of core plugs. Porosity typically ranges from 10% to 24% and permeability from 1 mD to 1000 mD, but lower and higher values have also been measured. Early mapping of the field in the 1960s is based on a 2D grid of seismic, and is clearly influenced by the data quality achievable then. In the Groningen field, it is not straightforward to obtain good data quality below the salt of the Zechstein Formation. Since the late 1980s the field has been fully covered by 3D data with several cycles of reprocessing that have improved the quality of the data considerably. The the Groningen field is affected by many normal (extensional) faults. The main fault trend affecting the field is NNW–SSE. Other fault trends run E–W and N–S. The highest density of faults is in the southern sector of the field [9].

B.0.2. RESERVOIR PRESSURE

Large parts of the Groningen reservoir are in good pressure communication. This indicates that most faults are not barriers to gas flow. However, at one point it was observed that the pressure measurements in the southwest of the field were lagging which show signs of compartmentalization in that region of the field. Initial reservoir pressures in the field is around of 34.6 MPa at a reference depth of 2875 m. This pressure was hydrostatic and virtually constant across the field [7].

The Groningen field is produced primarily under gas expansion drive but extensive aquifers interconnect with the field, potentially offering modest pressure support. Additionally, minor pressure support arises due to volume reduction resulting from compaction. In the initial decade of production, the majority of gas extraction originated from clusters situated in the south of the field resulting in the most significant pressure reduction in that region. During the 1970s, production from the northern sectors mitigated these imbalances. Since 2014, production limits are imposed on select northern clusters, consequently exacerbating the pressure imbalance [7].

A history and forecast for the pressure of the Groningen gas field is shown in Figure B.1 [128]. This image shows a minimum and maximum range predicted for the pressure beginning from 1960 when production started to 2080. This prediction is calculated based on reservoir simulation models that are calibrated with the regularly measured pressures in the production wells and the amount of gas, condensate and water produced over time. There are two curves in this figure: the minimum corresponds to the south of the field and the maximum pressures to the north of the field. According to this image, pressure in the Groningen field will eventually stabilize following the closure of the field to production.

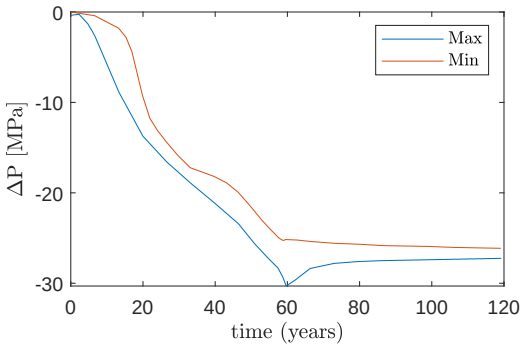

Figure B.1.: Reproduced plot of the Groningen gas field pressure history and forecast based on data from [128]. Time is counted in years from the beginning of production in 1960 to year 2080.

B.0.3. FAULTS IN THE GRONINGEN FIELD

Figure B.2 illustrates an areal map of the Groningen field, highlighting the complex network of faults within the region.

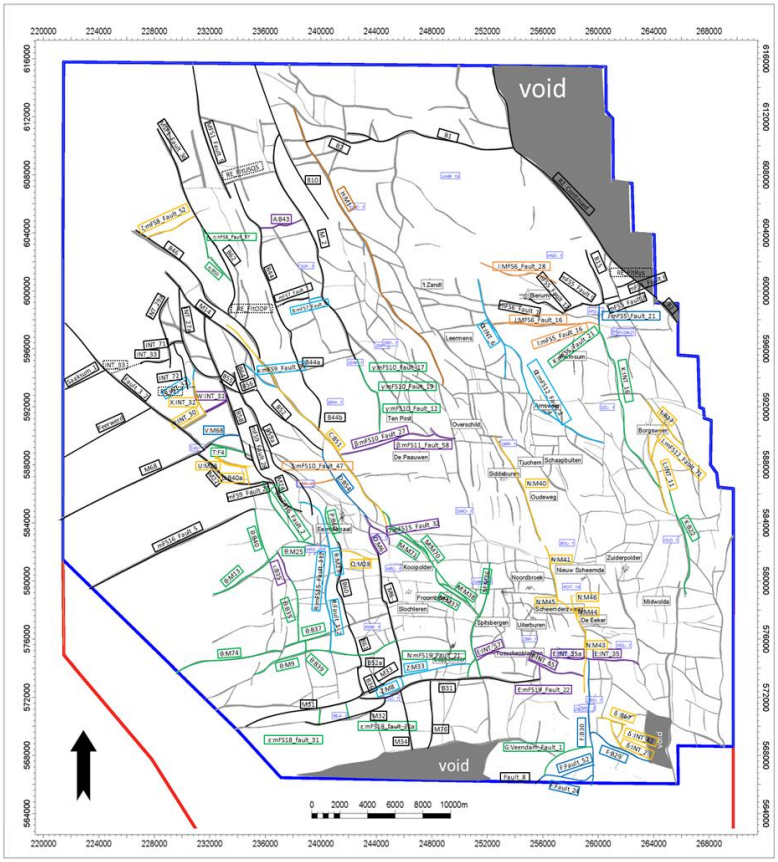

Figure B.2.: Areal view of the Groningen field demonstrating the intricate map of faults across the field [129].

Properties of these faults, such as transmissibility and slip resistance, can exhibit variations both across the field and along a fault itself. For example, friction coefficient differs per geological layer in the Groningen field. The static friction coefficients measured in the lab for different geological layer in the Groningen field are shown in Table B.1. The values of Table B.1 were measured assuming an effective normal stress of 40 MPa, pore fluid pressure of 15 MPa, reservoir temperature of 100 Celsius and sliding velocities in the range of $0.1 - 10\mu$ m/s

One of the friction models introduced in this study is the slip rate-dependent friction model described in Section 2.6.2. Th slip rate-dependent friction model (Equation 2.29 has two empirical constants (i.e. A and B) that are found with lab testing. Values for these constants are reported in literature for the Groningen field [105]. Table B.2 shows the parameters for the slip rate-dependent friction model for various geological layers in the Groningen field.

Table B.1.: Friction coefficients of the Groningen field formations as reported by [105].

formation	*minimum*	*mean*	*maximum*
Basal Zechstein	0.63	-	0.66
Ten Boer claystone	0.35	0.37	0.38
Slochteren sandstone	0.59	0.6	0.62
Carboniferous	0.49		0.5

Table B.2.: Ranges for the coefficients of Equation 2.29 for various formations in the Groningen field. The ranges for V_0 is 0.1-10 $\mu m/s$ in these measurements. These values were deported by [105].

formation	A[-]	B [-]	δ [mm]
Basal Zechstein	0.0021 – 0.0131	-0.0018 – 0.0047	0.0001 – 2.0848
Ten Boer claystone	0.0003 – 0.0037	– 0.0034 – 0.0010	0.0001 – 0.0338
Slochteren sandstone	0.0055 – 0.0311	0.0031 – 0.0282	0.0022 – 0.1749
Carboniferous	0.0021 – 0.0131	-0.0018 – 0.0047	0.0001 – 2.0848

The lab study by [105] on the slip rate-dependent friction model for the Groningen field faults showed that most formations in the Groningen field have velocity-strengthening behavior besides the Basal Zechstein. The Slochteren sandstone, Ten Boer clay-stone and Carboniferous shale formations show velocity strengthening behavior.

The behavior of the Basal Zechstein is different from other formations. Where salinity is low, this layer demonstrates both velocity weakening and strengthening behavior. For highly saline tests it shows velocity strengthening behavior. Another factor in friction of the Basal Zechstein is the range of the slip velocity which affects the friction behavior. Overall, the Basal Zechstein caprock has highest frictional strength and weakening. This means that the layers at the reservoir top (Basal Zechstein) which are made up of anhydrite-carbonate are most likely to have accelerating slip. This translates to most risk for induced seismicity.

The conclusions of [105] indicate that the faults which cut through Basal Zechstein (near the top of the reservoir) have the highest potential for slip. This is because 50:50 composition of these two materials in the gouge has velocity weakening behavior. However, they also report that earthquakes are reported to be centered all across the reservoir, not necessarily to the top.

C

A REALISTIC GEOMECHANICAL MODEL FOR THE GRONINGEN FIELD

An interesting application of the computation methods developed in this study is simulation of fault reactivation in more realistic models of the Groningen field. This requires a realistic geomechanical model for the field.

A field-scale geomechanical model for the Groningen field was not publicly available. In this section a brief overview is provided on how a representative geomechanical model was developed for the Groningen field.

NAM has publicly shared a geological model for the Groningen field. This model includes three dimensional horizon data for the reservoir and surrounding formations, a fault map, well data and seismic data [130]. This model can be accessed using Petrel® software [131]. This software was used to analyze the model. Figure C.1 shows a 2D image from the Rotliegend reservoir horizon (between 3000 to 4000 sub-sea meters) in the Groningen field.

Figure C.1 shows a vertical side-view of the model from the west side of the field. This figure shows the depths of the horizons included in the model.

As seen in Figure C.2, the model covers the reservoir layers and some of the overburden and underburden. Thus the shallower surface layers, and the deeper depths of the underburden are not included in this shared reservoir model. However, an encouraging aspect of the model is that it contains a map of faults in the Groningen field. This is shown in Figure C.3.

The geological model is found limited with respect to the requirements for the geomechanical intended in this study due to the following reasons

- The data in the geological model does not include geomechanical properties for the layers. For example, the values for the Lame parameters are required for the estimation of deformation but are missing.
- The formation horizons included in the model are limited to the reservoir formation and some of the neighbouring layers. Therefore, shallower and deeper depths are entirely missing in the model.

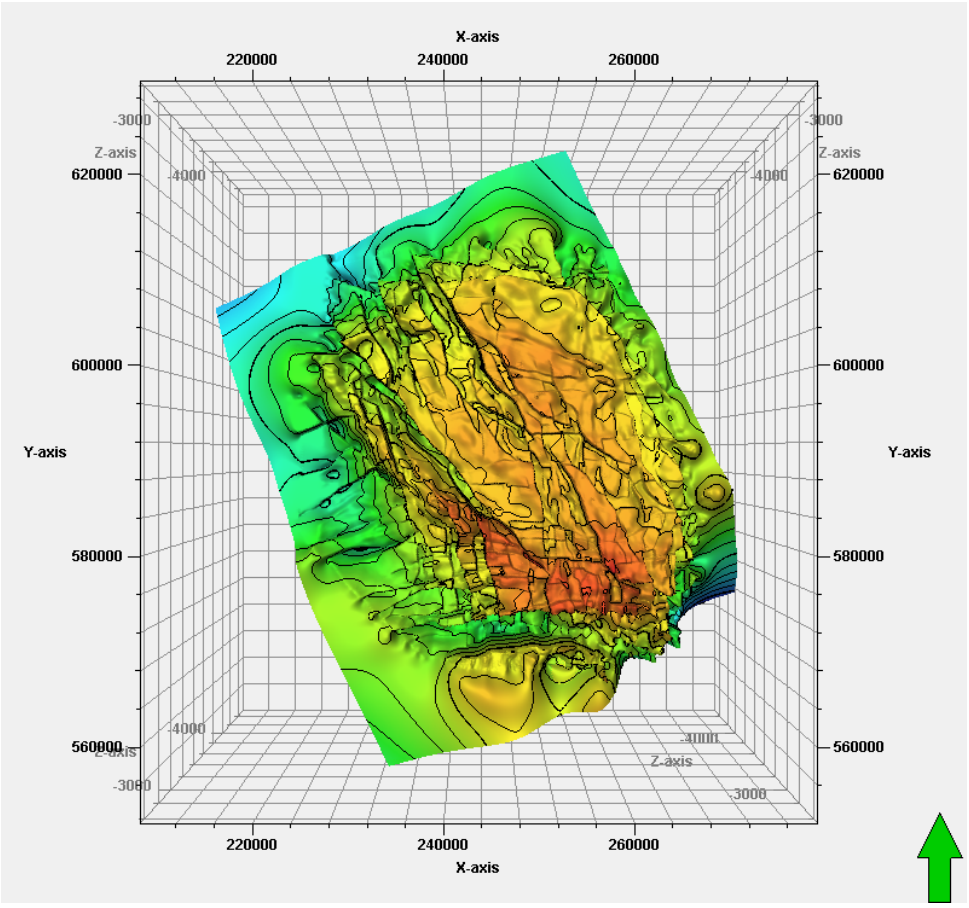

Figure C.1.: Top view image from the Rotliegend horizon in the Groningen reservoir. This image is extracted from the field's shared model [130].

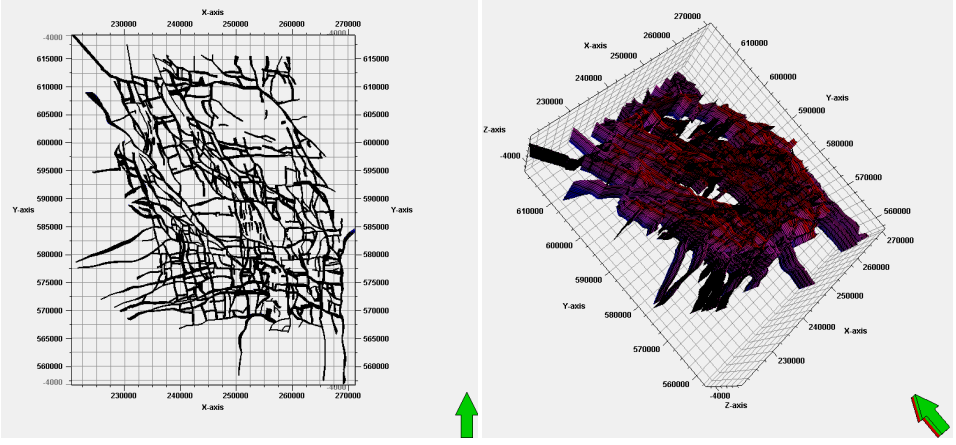

Figure C.3.: Fault map for the Groningen reservoir model: a horizontal cross section (top) and in 3D (bottom). This image is extracted from the fault model shared in [130].

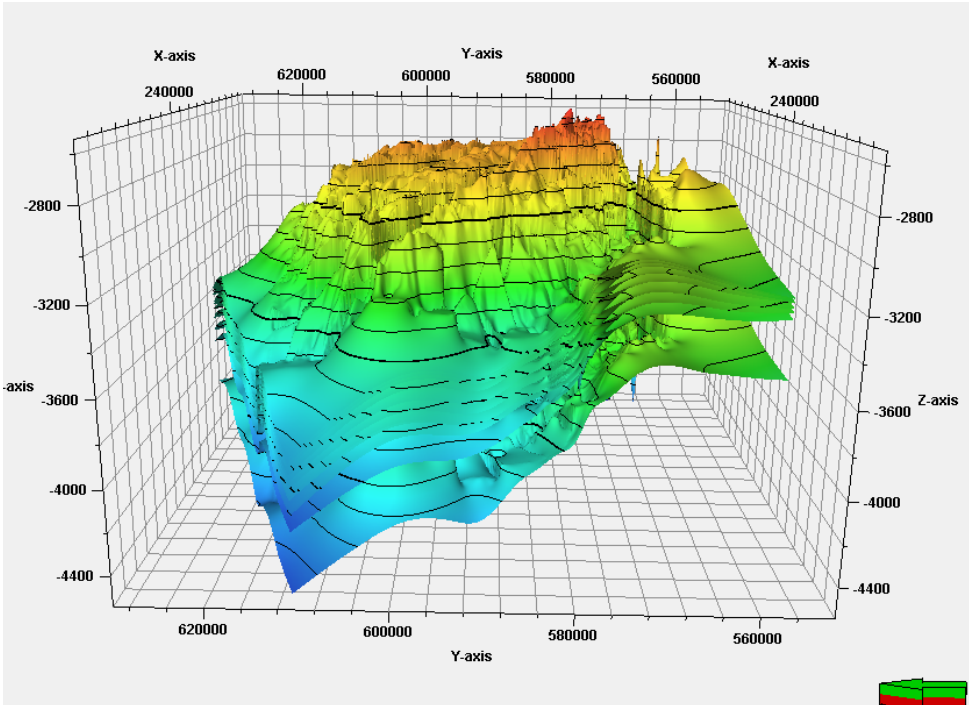

Figure C.2.: A vertical side-view image from the horizons in the Groningen reservoir model. This image is extracted from the field's shared model [130].

Recognizing the limits of the existing geological model, a representative geomechanical model is created for the Groningen field. For this purpose, a seismic velocity model for the Groningen field is used [132]. This velocity model contains the following information:

- Horizon depths for formations in the Groningen field. This data comes in the format of sub-sea depths versus location (identified with geographical coordinates).
- The horizon data covers depths from surface elevation, down to a sub-sea depth of 4500 m.
- This data separates the upper north sea and the lower north sea. This is followed by a chalk formation. The data for Rijnland, Jurassic and Triassic formations is summarized into one. It is mentioned that this is because the sonic logs for these formations showed little variability. This is followed by a Zechstein Halite layer, a Zechstein Anhydrite layer, followed by another Zechstein Halite and Zechstein Anhydrite layers. The Rotliegend reservoir is next. The last formation after Rotliegend is the Carboniferous.
- The p-wave, s-wave and density model is provided for each formation.

The models can assign a constant value to a layer, or a function. These functions can depend on depth and/or other geomechanical parameters [132].

The geomechanical model used in this study was created according to the following procedure.

Algorithm 7: Algorithm for generating a realistic geomechanical model for the Groningen field

Result: $[\lambda, G, \nu, E]$ and fault placement

1 The horizon depth data for the 11 horizons were imported into Petrel® software [131]. This data contain x-y coordinates and depths ;
2 The data points were interpolated to create surfaces for the horizons. ;
3 The system was gridded with a 3D mesh with respect to the defined horizons and the lateral extents of the data ;
4 The p-wave, s-wave and density was allocated to each formation based on the Groningen velocity model described in [132]. For some formations, a constant value is assigned to the entire formation for the p-wave, s-wave and density. For others, functions are considered. These functions can depend on depth, have multipliers, they can be a function of another seismic property or require addition of location-dependent constants. ;
5 Other geomechanical properties such as the first and second Lame parameters, the Poisson ratio, Young's modulus, etc. were obtained based on the p-wave, s-wave and density models by conversions listed in Appendix A;
6 Faults are extracted from the original geological petrel model of the Groningen field [130] and loaded over the geomechanical model created here;

Figure C.4 shows the loaded data points for only one horizon: the Rotliegend horizon. The top and bottom surfaces show surface elevation and a depth of 4500 m sub-sea. Given the density of the data, it may resemble a surface at some points. However, this data is point based and requires interpolation for estimation of a surface.

The interpolated surface for Rotliegend horizon is shown in Figure C.5. This process is repeated for all the other horizons. The algorithm used here to make surfaces is based on the closest neighbour method. In this method, the value for a cell is assigned based on the value of the data point closest to it.

The surfaces created for all horizons are used to create a 3D mesh. The mesh is shown in Figure C.6. This mesh has $127 \times 117 \times 100$ grid cells in the x-y-z directions totalling 148.6 million cells.

Next, the models for seismic velocities and density are assigned to each layer. Each layer is defined between two horizons and the cell values are determined based on the models reported in [132]. The results for one property, the density, is shown in Figure C.7. Similar curves are obtained for the s-wave and p-wave velocities. They are then used to find other geomechanical properties based on conversion formulae.

Following the creation of a geomechanical model, the fault map from the original geological model is loaded. Figure C.8 shows a 2D cross section of the first Lame parameter (i.e. λ) with the faults.

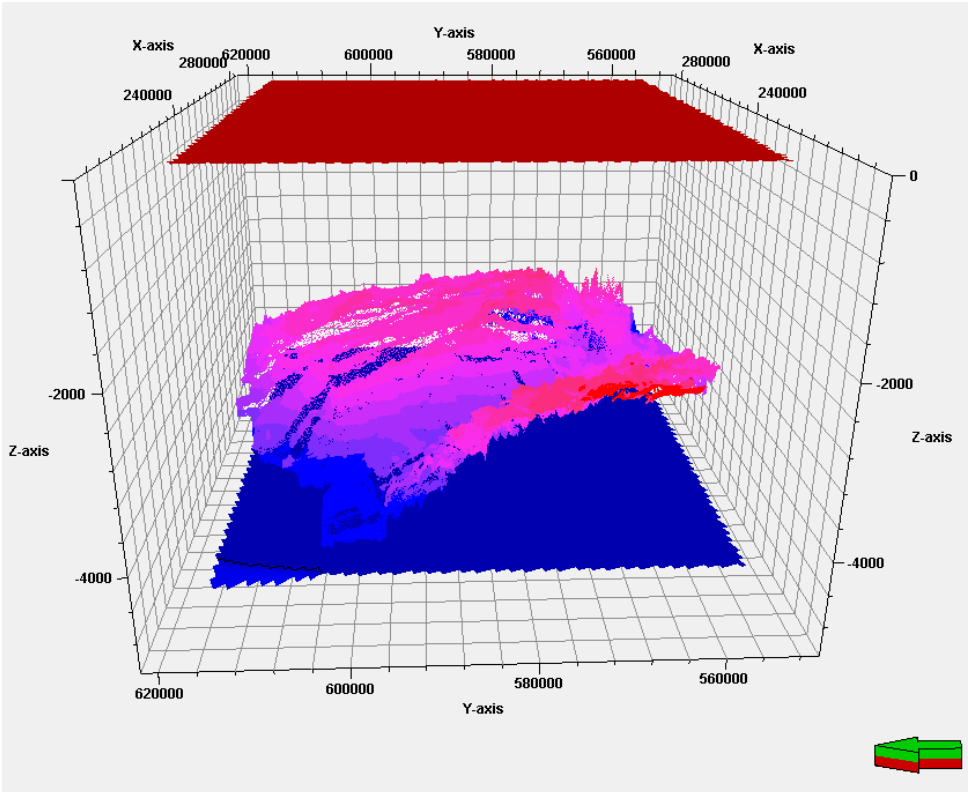

Figure C.4.: Plot of point data for the Rotliegend horizon based on horizon data from [132].

The cross section is created by running a 180 azimuth angle intersection plane passing through Slochteren-4 well. Other 2D maps could easily be extracted by changing this origin and angle. In this figure, the Rotliegend reservoir can be seen with a darker shade of blue in the −3000 m to −3500 m depth range. The reservoir is overlaid by a thinner layer of salt shown in red.

One of the issues in the developed model is the miss-match between the fault model and the geometry of the layers. The extension of the faults above and below the reservoir layer also seem unrealistic. Large extension of a majority of the faults above the Basal Zechstein layer is not expected but observed in Figure C.8. The importance of improved study of fault maps in the Groningen field has been outlined in earlier research. In 2017, Kortekaas and Jaarsma used an ant-tracking method for improved fault definition in the Groningen field based on seismic data [124].

In the current study, the fault location was adjusted manually to better honor the geometry of the layers. The fault top was confined to the salt layer above the reservoir. The fault was allowed to run deeper into the underlying carboniferous layer. These adjustments are implemented on the 2D map of Figure C.8. The results are shown in Figure C.9.

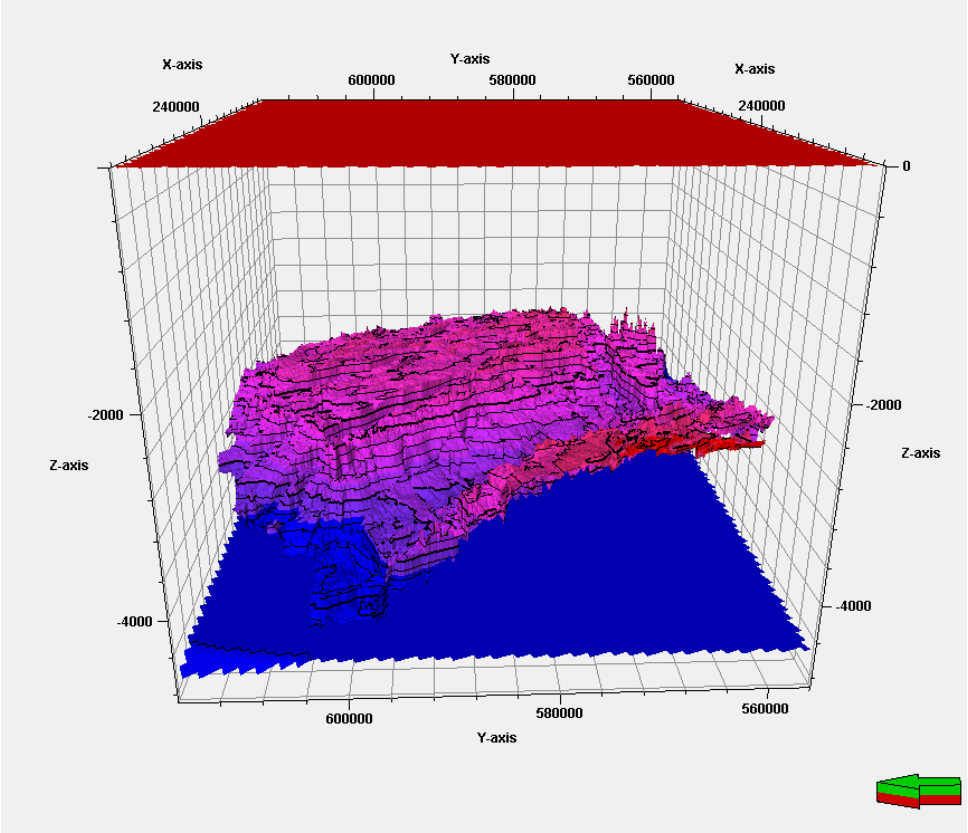

Figure C.5.: An interpolated surface for the Rotliegend horizon based on the data points of Figure C.4.

This figure is obtained by digitizing Figure C.8, making the correct adjustments with respect to faults and scaling it down to the desired mesh resolution for the simulation of fault slip.

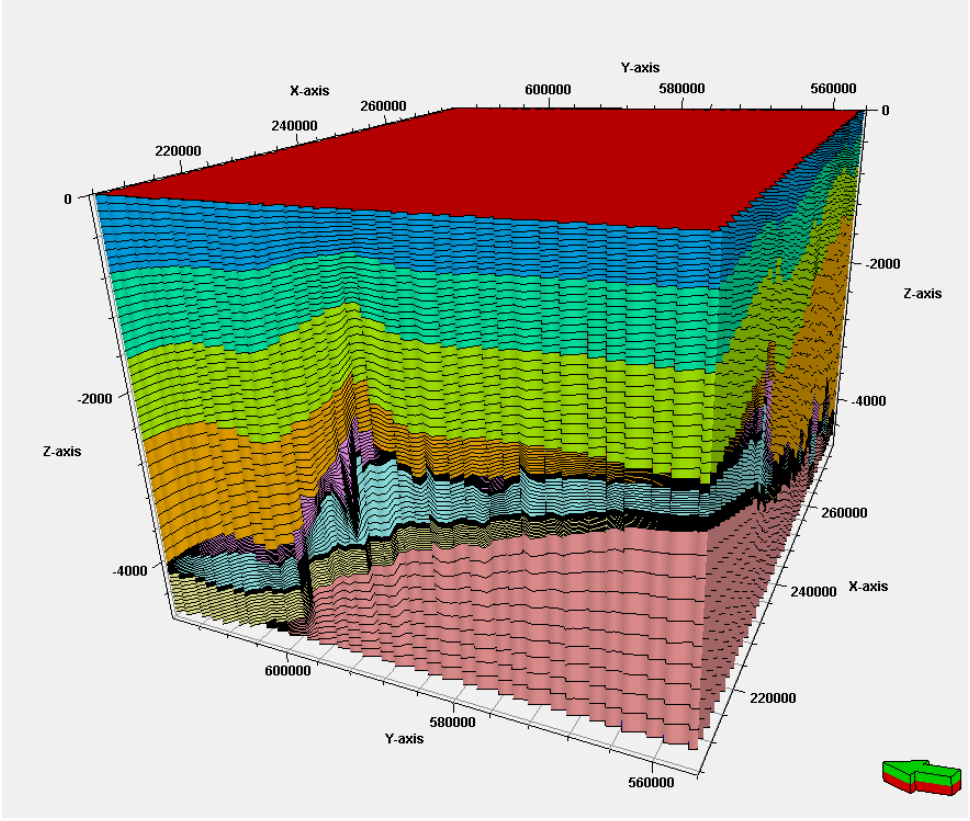

Figure C.6.: The 3D mesh created for the Groningen field model based on horizon surfaces similar to Figure C.4

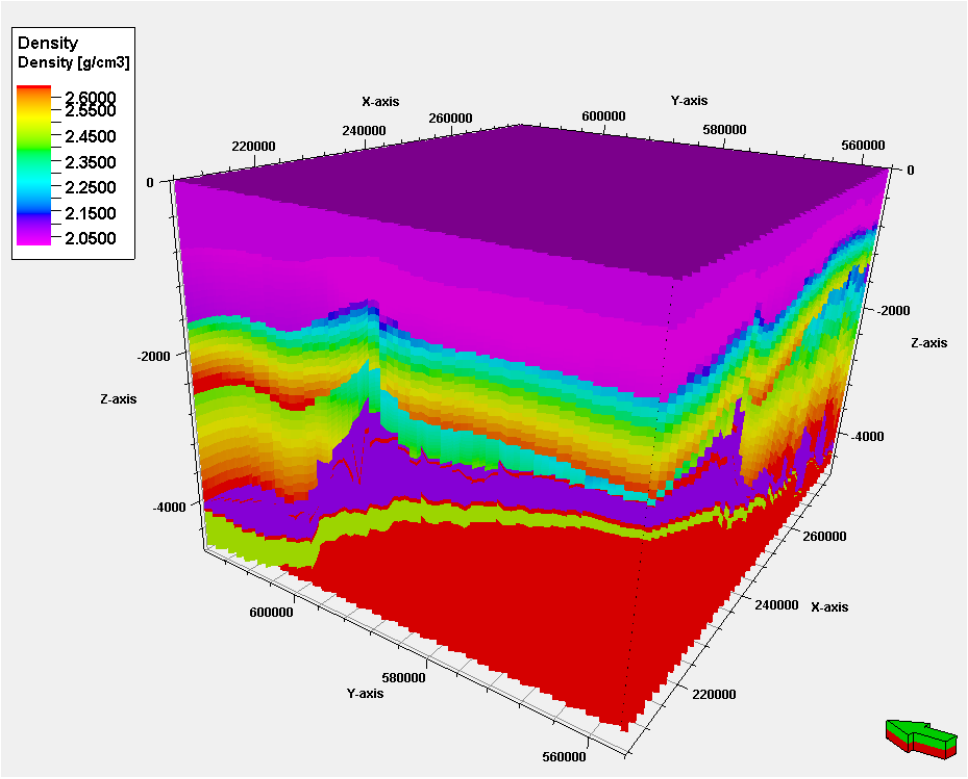

Figure C.7.: The 3D mesh created for the Groningen field model based on horizon surfaces

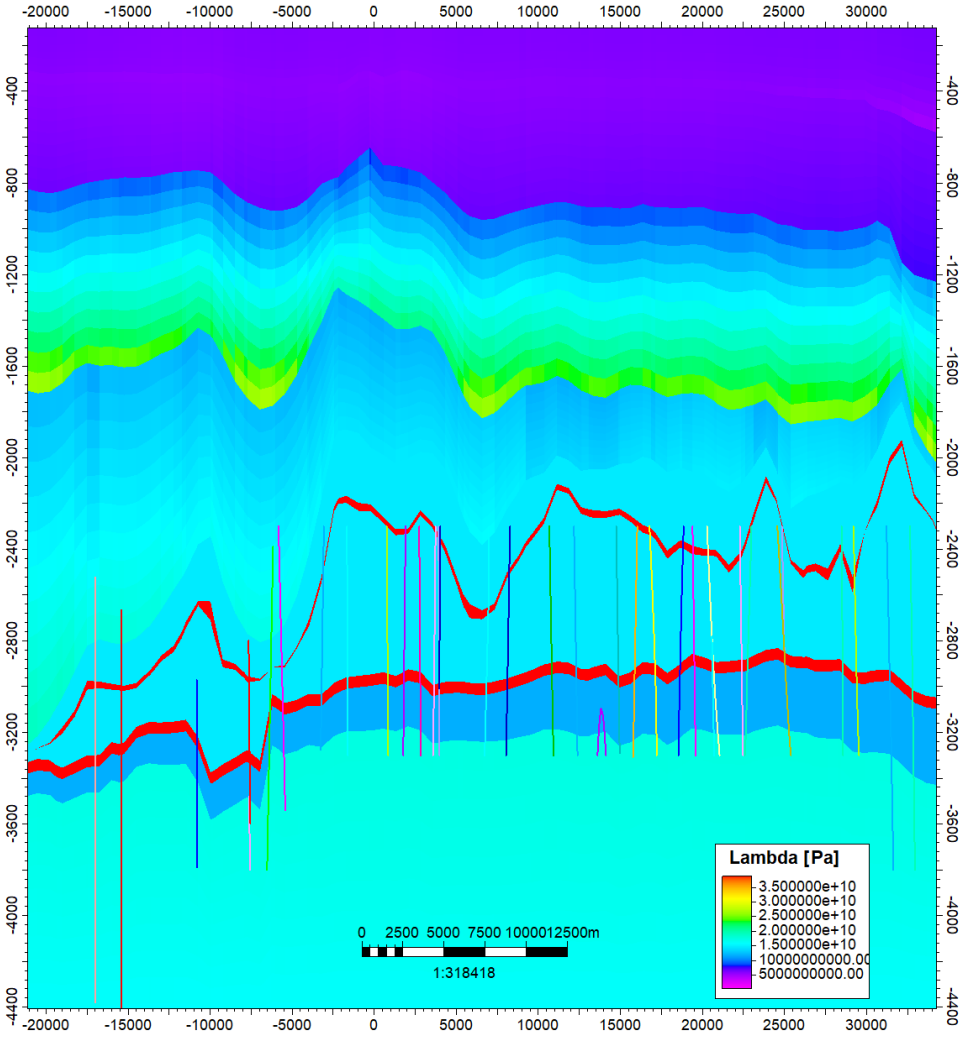

Figure C.8.: A cross-section showing a 2D map of the first Lame parameter for various layers and the location of the faults along the layers.

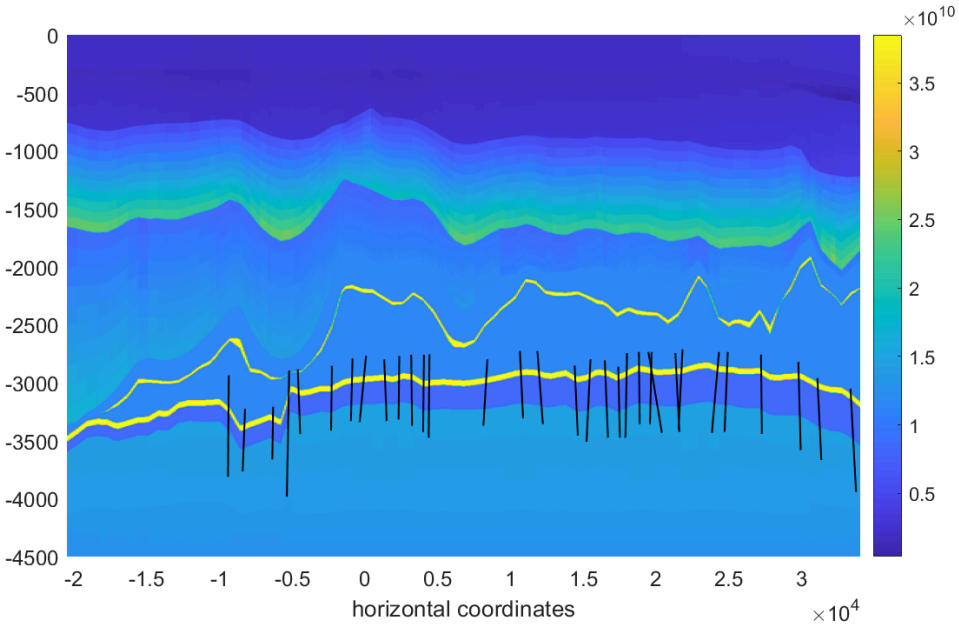

Figure C.9.: 2D cross section for the First Lame parameter after fault adjustments.

REFERENCES

[1] R. Van Eijs, F. Mulders, M. Nepveu, C. Kenter, and B. Scheffers. "Correlation between hydrocarbon reservoir properties and induced seismicity in the Netherlands". In: *Engineering Geology* 84.3-4 (2006), pp. 99–111.

[2] J. J. Bommer, H. Crowley, and R. Pinho. "A risk-mitigation approach to the management of induced seismicity". In: *Journal of Seismology* 19 (2015), pp. 623–646.

[3] K. Stroebe, B. Kanis, J. Richardson, F. Oldersma, J. Broer, F. Greven, and T. Postmes. "Chronic disaster impact: the long-term psychological and physical health consequences of housing damage due to induced earthquakes". In: *BMJ open* 11.5 (2021), e040710.

[4] S. Mugnano, F. Carnelli, and S. Zizzari. "The recovery strategy of second homeowners and tourists after a disaster: insights from the 2016 central Italy earthquakes". In: *Earthquake risk perception, communication and mitigation strategies across Europe, Il Sileno Edizioni, Geographies of the Anthropocene book series, Rende* 2.2 (2019), pp. 267–284.

[5] R. T. Porter, A. Striolo, H. Mahgerefteh, and J. Faure Walker. "Addressing the risks of induced seismicity in subsurface energy operations". In: *Wiley Interdisciplinary Reviews: Energy and Environment* 8.2 (2019), e324.

[6] J. De Waal, A. Muntendam-Bos, and J. Roest. "From checking deterministic predictions to probabilities, scenarios and control loops for regulatory supervision". In: *Netherlands Journal of Geosciences* 96.5 (2017), s17–s25.

[7] NAM. *NAM, ambient aware and participating in society*. URL: https://www.nam.nl/english-information.html. (accessed: 30.10.2020).

[8] B. Vogelaar, S. Osinga, D. Kraaijpoel, M. Pluymaekers, J. Breunese, and W. van Driel. "Publieke Seismische Dreigings-en Risicoanalyse Groningen gasveld 2021". In: (2021).

[9] J. De Jager and C. Visser. "Geology of the Groningen field–an overview". In: *Netherlands Journal of Geosciences* 96.5 (2017), s3–s15.

[10] F. Holz, H. Brauers, P. M. Richter, and T. Roobeek. "Shaking Dutch grounds won't shatter the European gas market". In: *Energy Economics* 64 (2017), pp. 520–529.

[11] M. Mulder and P. Perey. "Gas production and earthquakes in Groningen; reflection on economic and social consequences". In: *Centre for Energy Economics Research (CEER), Policy Papers* 3 (2018).

[12] K. van Thienen-Visser and J. Breunese. "Induced seismicity of the Groningen gas field: History and recent developments". In: *The Leading Edge* 34.6 (2015), pp. 664–671.

[13] A. Muntendam-Bos and N. Grobbe. “Data-driven spatiotemporal assessment of the event-size distribution of the Groningen extraction-induced seismicity catalogue”. In: *Scientific Reports* 12.1 (2022), p. 10119.

[14] C. Vlek. “Reflections and Some Questions about Assessing the Maximum Possible Earthquake in the Long-Exploited Groningen Gas Field”. In: *Seismological Research Letters* 94.5 (2023), pp. 2469–2478.

[15] M. D. Zoback. *Reservoir geomechanics*. Cambridge University Press, 2010.

[16] P. J. Phillips and M. F. Wheeler. “A coupling of mixed and continuous Galerkin finite element methods for poroelasticity I: the continuous in time case”. In: *Computational Geosciences* 11.2 (2007), p. 131.

[17] Z. P. Bažant, M. Salviato, V. T. Chau, H. Viswanathan, and A. Zubelewicz. “Why fracking works”. In: *Journal of Applied Mechanics* 81.10 (2014).

[18] R. A. Morton, J. C. Bernier, and J. A. Barras. “Evidence of regional subsidence and associated interior wetland loss induced by hydrocarbon production, Gulf Coast region, USA”. In: *Environmental Geology* 50.2 (2006), p. 261.

[19] M. Grant. *Geothermal reservoir engineering*. Elsevier, 2013.

[20] K. S. Lackner. “A guide to CO2 sequestration”. In: *Science* 300.5626 (2003), pp. 1677–1678.

[21] S. Bauer, C. Beyer, F. Dethlefsen, P. Dietrich, R. Duttmann, M. Ebert, V. Feeser, U. Görke, R. Köber, O. Kolditz, *et al.* “Impacts of the use of the geological subsurface for energy storage: an investigation concept”. In: *Environmental earth sciences* 70.8 (2013), pp. 3935–3943.

[22] F. Zhang, P. Zhao, M. Niu, and J. Maddy. “The survey of key technologies in hydrogen energy storage”. In: *International Journal of Hydrogen Energy* 41.33 (2016), pp. 14535–14552.

[23] N. R. Council *et al. Induced seismicity potential in energy technologies*. National Academies Press, 2013.

[24] K. Park. “Stabilization of partitioned solution procedure for pore fluid-soil interaction analysis”. In: *International Journal for Numerical Methods in Engineering* 19.11 (1983), pp. 1669–1673.

[25] O. Zienkiewicz, D. Paul, and A. Chan. “Unconditionally stable staggered solution procedure for soil-pore fluid interaction problems”. In: *International Journal for Numerical Methods in Engineering* 26.5 (1988), pp. 1039–1055.

[26] J. Kim, H. A. Tchelepi, and R. Juanes. “Stability and convergence of sequential methods for coupled flow and geomechanics: Fixed-stress and fixed-strain splits”. In: *Computer Methods in Applied Mechanics and Engineering* 200.13-16 (2011), pp. 1591–1606.

[27] R. W. Lewis, R. W. Lewis, and B. Schrefler. *The finite element method in the static and dynamic deformation and consolidation of porous media*. John Wiley & Sons, 1998.

[28] O. Zienkiewicz and I. Cormeau. “Visco-plasticity—plasticity and creep in elastic solids—a unified numerical solution approach”. In: *International Journal for Numerical Methods in Engineering* 8.4 (1974), pp. 821–845.

[29] K. R. Kumar and H. Hajibeygi. “Multiscale simulation of inelastic creep deformation for geological rocks”. In: *Journal of Computational Physics* 440 (2021), p. 110439.

[30] S. Salimzadeh, A. Paluszny, H. M. Nick, and R. W. Zimmerman. “A three-dimensional coupled thermo-hydro-mechanical model for deformable fractured geothermal systems”. In: *Geothermics* 71 (2018), pp. 212–224.

[31] J. W. Both, K. Kumar, J. M. Nordbotten, and F. A. Radu. “The gradient flow structures of thermo-poro-visco-elastic processes in porous media”. In: *arXiv preprint arXiv:1907.03134* (2019).

[32] J. Byerlee. “Friction of rocks”. In: *Rock friction and earthquake prediction*. Springer, 1978, pp. 615–626.

[33] Y. Ida. “Cohesive force across the tip of a longitudinal-shear crack and Griffith’s specific surface energy”. In: *Journal of Geophysical Research* 77.20 (1972), pp. 3796–3805.

[34] C. H. Scholz. “Earthquakes and friction laws”. In: *Nature* 391.6662 (1998), pp. 37–42.

[35] J. H. Dieterich. “Modeling of rock friction: 1. Experimental results and constitutive equations”. In: *Journal of Geophysical Research: Solid Earth* 84.B5 (1979), pp. 2161–2168.

[36] A. Ruina. “Slip instability and state variable friction laws”. In: *Journal of Geophysical Research: Solid Earth* 88.B12 (1983), pp. 10359–10370.

[37] R. P. Pijnenburg and C. J. Spiers. “Microphysics of Inelastic Deformation in Reservoir Sandstones from the Seismogenic Center of the Groningen Gas Field”. In: *Rock Mechanics and Rock Engineering* 53.12 (2020), pp. 5301–5328.

[38] A. Niemeijer and C. Spiers. “Velocity dependence of strength and healing behaviour in simulated phyllosilicate-bearing fault gouge”. In: *Tectonophysics* 427.1-4 (2006), pp. 231–253.

[39] A. Niemeijer and C. Spiers. “A microphysical model for strong velocity weakening in phyllosilicate-bearing fault gouges”. In: *Journal of Geophysical Research: Solid Earth* 112.B10 (2007).

[40] J. Chen and C. J. Spiers. “Rate and state frictional and healing behavior of carbonate fault gouge explained using microphysical model”. In: *Journal of Geophysical Research: Solid Earth* 121.12 (2016), pp. 8642–8665.

[41] Z. Reches. “Dynamic Frictional Slip Along Rock Faults”. In: *Journal of Tribology* 142.12 (2020).

[42] M. Van den Ende, J. Chen, J.-P. Ampuero, and A. Niemeijer. “A comparison between rate-and-state friction and microphysical models, based on numerical simulations of fault slip”. In: *Tectonophysics* 733 (2018), pp. 273–295.

C

[43] B. Baliga, T. Pham, and S. Patankar. “Solution of some two-dimensional incompressible fluid flow and heat transfer problems, using a control volume finite-element method”. In: *Numerical Heat Transfer* 6.3 (1983), pp. 263–282.

[44] F. Gaspar, F. Lisbona, and P. Vabishchevich. “Staggered grid discretizations for the quasi-static Biot’s consolidation problem”. In: *Applied numerical mathematics* 56.6 (2006), pp. 888–898.

[45] F. Gaspar, F. Lisbona, and P. Vabishchevich. “A finite difference analysis of Biot’s consolidation model”. In: *Applied numerical mathematics* 44.4 (2003), pp. 487–506.

[46] M. Vinokur. “An analysis of finite-difference and finite-volume formulations of conservation laws”. In: *Journal of computational physics* 81.1 (1989), pp. 1–52.

[47] J. Peiró and S. Sherwin. “Finite difference, finite element and finite volume methods for partial differential equations”. In: *Handbook of materials modeling*. Springer, 2005, pp. 2415–2446.

[48] E. Stein. “History of the finite element method–mathematics meets mechanics–part I: Engineering developments”. In: *The History of Theoretical, Material and Computational Mechanics-Mathematics Meets Mechanics and Engineering*. Springer, 2014, pp. 399–442.

[49] T. J. R. Hughes. *The Finite Element Method: Linear Static and Dynamic Finite Element Analysis*. Dover Publications, 2000.

[50] W. S. Venturini. *Boundary element method in geomechanics*. Vol. 4. Springer Science & Business Media, 2012.

[51] T. B. Thompson and B. J. Meade. “Boundary element methods for earthquake modeling with realistic 3D geometries”. In: (2019).

[52] Y. Liu, S. Mukherjee, N. Nishimura, M. Schanz, W. Ye, A. Sutradhar, E. Pan, N. A. Dumont, A. Frangi, and A. Saez. “Recent advances and emerging applications of the boundary element method”. In: *Applied Mechanics Reviews* 64.3 (2011), p. 030802.

[53] M. Rashid. “The arbitrary local mesh replacement method: an alternative to remeshing for crack propagation analysis”. In: *Computer Methods in Applied Mechanics and Engineering* 154.1-2 (1998), pp. 133–150.

[54] S. Bosma, H. Hajibeygi, M. Tene, and H. A. Tchelepi. “Multiscale finite volume method for discrete fracture modeling on unstructured grids (MS-DFM)”. In: *Journal of Computational Physics* 351 (2017), pp. 145–164.

[55] L. Li and D. Voskov. “A novel hybrid model for multiphase flow in complex multiscale fractured systems”. In: *Journal of Petroleum Science and Engineering* 203 (2021), p. 108657.

[56] T. T. Garipov, M. Karimi-Fard, and H. A. Tchelepi. “Discrete fracture model for coupled flow and geomechanics”. In: *Computat. Geosci.* 20.1 (2016), pp. 149–160. DOI: 10.1007/s10596-015-9554-z.

[57] L. Li, S. H. Lee, *et al.* "Efficient field-scale simulation of black oil in a naturally fractured reservoir through discrete fracture networks and homogenized media". In: *SPE Reservoir Evaluation & Engineering* 11.04 (2008), pp. 750–758.

[58] R. Löhner, J. R. Cebral, F. E. Camelli, S. Appanaboyina, J. D. Baum, E. L. Mestreau, and O. A. Soto. "Adaptive embedded and immersed unstructured grid techniques". In: *Computer Methods in Applied Mechanics and Engineering* 197.25-28 (2008), pp. 2173–2197.

[59] H. Hajibeygi, D. Karvounis, and P. Jenny. "A hierarchical fracture model for the iterative multiscale finite volume method". In: *Journal of Computational Physics* 230.24 (2011), pp. 8729–8743.

[60] M. HosseiniMehr, M. Cusini, C. Vuik, and H. Hajibeygi. "Algebraic dynamic multilevel method for embedded discrete fracture model (F-ADM)". In: *Journal of Computational Physics* 373 (2018), pp. 324–345.

[61] T. Belytschko, N. Moës, S. Usui, and C. Parimi. "Arbitrary discontinuities in finite elements". In: *International Journal for Numerical Methods in Engineering* 50.4 (2001), pp. 993–1013.

[62] A. Fumagalli and A. Scotti. "An efficient XFEM approximation of Darcy flows in arbitrarily fractured porous media". In: *Oil & Gas Science and Technology–Revue d'IFP Energies nouvelles* 69.4 (2014), pp. 555–564.

[63] F. Xu, H. Hajibeygi, and L. J. Sluys. "Multiscale extended finite element method for deformable fractured porous media". In: *Journal of Computational Physics* 436 (2021), p. 110287.

[64] R. Deb and P. Jenny. "Finite volume–based modeling of flow-induced shear failure along fracture manifolds". In: *International Journal for Numerical and Analytical Methods in Geomechanics* 41.18 (2017), pp. 1922–1942.

[65] R. Deb and P. Jenny. "Modeling of shear failure in fractured reservoirs with a porous matrix". In: *Computational Geosciences* 21.5-6 (2017), pp. 1119–1134.

[66] I. Sokolova, M. G. Bastisya, and H. Hajibeygi. "Multiscale finite volume method for finite-volume-based simulation of poroelasticity". In: *Journal of Computational Physics* 379 (2019), pp. 309–324.

[67] B. Flemisch, I. Berre, W. Boon, A. Fumagalli, N. Schwenck, A. Scotti, I. Stefansson, and A. Tatomir. "Benchmarks for single-phase flow in fractured porous media". In: *Advances in Water Resources* 111 (2018), pp. 239–258.

[68] T. Li, D. Han, F. Yang, B. Yu, D. Sun, and J. Wei. "A comparative study on simulating flow-induced fracture deformation in subsurface media by means of extended FEM and FVM". In: *Oil & Gas Science and Technology–Revue d'IFP Energies nouvelles* 75 (2020), p. 41.

[69] P. Segall, J.-R. Grasso, and A. Mossop. "Poroelastic stressing and induced seismicity near the Lacq gas field, southwestern France". In: *Journal of Geophysical Research: Solid Earth* 99.B8 (1994), pp. 15423–15438.

C

[70] T. T. Garipov, P. Tomin, R. Rin, D. V. Voskov, and H. A. Tchelepi. “Unified thermo-compositional-mechanical framework for reservoir simulation”. In: *Computational Geosciences* 22.4 (2018), pp. 1039–1057.

[71] M. Ţene, S. B. Bosma, M. S. Al Kobaisi, and H. Hajibeygi. “Projection-based embedded discrete fracture model (pEDFM)”. In: *Advances in Water Resources* 105 (2017), pp. 205–216.

[72] L. Buijze, P. A. van den Bogert, B. B. Wassing, B. Orlic, and J. ten Veen. “Fault reactivation mechanisms and dynamic rupture modelling of depletion-induced seismic events in a Rotliegend gas reservoir”. In: *Netherlands Journal of Geosciences* 96.5 (2017), s131–s148.

[73] J. Roest and W. Kuilman. “Geomechanical analysis of small earthquakes at the Eleveld gas reservoir”. In: *SPE/ISRM Rock Mechanics in Petroleum Engineering*. SPE. 1994, SPE–28097.

[74] F. Mulders. “Modelling of stress development and fault slip in and around a producing gas reservoir”. PhD thesis. Civil Engineering and Geosciences, Delft University of Technology, 2003.

[75] J. Van Wees, L. Buijze, K. Van Thienen-Visser, M. Nepveu, B. Wassing, B. Orlic, and P. Fokker. “Geomechanics response and induced seismicity during gas field depletion in the Netherlands”. In: *Geothermics* 52 (2014), pp. 206–219.

[76] P. Van den Bogert. “Impact of various modelling options on the onset of fault slip and fault slip response using 2-dimensional finite-element modelling”. In: *Report No. SR.15.11455* 15 (2015).

[77] P. Van den Bogert. “Depletion-induced fault slip and seismic rupture - 2D Geomechanical models for the Groningen field”. In: *Report No. SR.18.01927* (2018).

[78] L. Buijze, B. Orlic, B. Wassing, and G.-J. Schreppers. “Dynamic rupture modeling of injection-induced seismicity: influence of pressure diffusion below porous aquifers”. In: *ARMA US Rock Mechanics/Geomechanics Symposium*. ARMA. 2015, ARMA–2015.

[79] J. Du and J. E. Olson. “A poroelastic reservoir model for predicting subsidence and mapping subsurface pressure fronts”. In: *Journal of Petroleum Science and Engineering* 30.3-4 (2001), pp. 181–197.

[80] J. Jansen, P. Singhal, and F. Vossepoel. “Insights from closed-form expressions for injection-and production-induced stresses in displaced faults”. In: *Journal of Geophysical Research: Solid Earth* 124.7 (2019), pp. 7193–7212.

[81] P. Cornelissen and J.-D. Jansen. “Steady-state flow through a subsurface reservoir with a displaced fault and its poro-elastic effects on fault stresses”. In: *Transport in Porous Media* (2023), pp. 1–26.

[82] P. M. Anderson, J. P. Hirth, and J. Lothe. *Theory of dislocations*. Cambridge University Press, 2017.

[83] J. D. Eshelby. “A Discussion on the measurement and interpretation of changes of strain in the Earth-Dislocation theory for geophysical applications”. In: *Philosophical Transactions of the Royal Society of London. Series A, Mathematical and Physical Sciences* 274.1239 (1973), pp. 331–338.

[84] J. Hirth. “A brief history of dislocation theory”. In: *Metallurgical Transactions A* 16 (1985), pp. 2085–2090.

[85] J. Geertsma. “Problems of rock mechanics in petroleum production engineering”. In: *ISRM Congress*. ISRM. 1966, ISRM–1CONGRESS.

[86] J. Geertsma. “Land subsidence above compacting oil and gas reservoirs”. In: *Journal of petroleum technology* 25.06 (1973), pp. 734–744.

[87] J. D. Eshelby. “The determination of the elastic field of an ellipsoidal inclusion, and related problems”. In: *Proceedings of the royal society of London. Series A. Mathematical and physical sciences* 241.1226 (1957), pp. 376–396.

[88] P. Segall. “Stress and subsidence resulting from subsurface fluid withdrawal in the epicentral region of the 1983 Coalinga earthquake”. In: *Journal of Geophysical Research: Solid Earth* 90.B8 (1985), pp. 6801–6816.

[89] P. Segall. “Earthquakes triggered by fluid extraction”. In: *Geology* 17.10 (1989), pp. 942–946.

[90] W. E. Pratt and D. W. Johnson. “Local subsidence of the Goose Creek oil field”. In: *The Journal of Geology* 34.7, Part 1 (1926), pp. 577–590.

[91] P. Segall. “Induced stresses due to fluid extraction from axisymmetric reservoirs”. In: *pure and applied geophysics* 139 (1992), pp. 535–560.

[92] J. Walsh. “Subsidence above a planar reservoir”. In: *Journal of Geophysical Research: Solid Earth* 107.B9 (2002), ETG–6.

[93] J. Rudnicki. “Eshelby transformations, pore pressure and fluid mass changes, and subsidence”. In: *Poromechanics II*. CRC Press, 2020, pp. 307–312.

[94] H. Soltanzadeh and C. D. Hawkes. “Semi-analytical models for stress change and fault reactivation induced by reservoir production and injection”. In: *Journal of Petroleum Science and Engineering* 60.2 (2008), pp. 71–85.

[95] J.-D. Jansen and B. Meulenbroek. “Induced aseismic slip and the onset of seismicity in displaced faults”. In: *Netherlands Journal of Geosciences* 101 (2022), e13.

[96] K. Uenishi and J. R. Rice. “Universal nucleation length for slip-weakening rupture instability under nonuniform fault loading”. In: *Journal of Geophysical Research: Solid Earth* 108.B1 (2003).

[97] R. Bürgmann, D. D. Pollard, and S. J. Martel. “Slip distributions on faults: effects of stress gradients, inelastic deformation, heterogeneous host-rock stiffness, and fault interaction”. In: *Journal of Structural Geology* 16.12 (1994), pp. 1675–1690.

[98] D. D. Oglesby, S. M. Day, and D. R. O’Connell. “Dynamic and static interaction of two thrust faults: A case study with general implications”. In: *Journal of Geophysical Research: Solid Earth* 108.B10 (2003).

[99] S. Shokrollahzadeh Behbahani, H. Hajibeygi, D. Voskov, and J. D. Jansen. “Smoothed embedded finite-volume method (sEFVM) for modeling contact mechanics in deformable faulted and fractured porous media”. In: *Journal of Computational Physics* 459 (2022), p. 111143.

[100] M. W. McClure and R. N. Horne. “Investigation of injection-induced seismicity using a coupled fluid flow and rate/state friction model”. In: *Geophysics* 76.6 (2011), WC181–WC198.

[101] H. F. Wang. *Theory of linear poroelasticity with applications to geomechanics and hydrogeology*. Vol. 2. Princeton University Press, 2000.

[102] A. J. L. Buijze. “Numerical and experimental simulation of fault reactivation and earthquake rupture applied to induced seismicity in the Groningen gas field”. PhD thesis. Utrecht University, 2020.

[103] G. Mesri and T. Hayat. “The coefficient of earth pressure at rest”. In: *Canadian Geotechnical Journal* 30.4 (1993), pp. 647–666.

[104] L. Wang, G. Kwiatek, E. Rybacki, A. Bonnelye, M. Bohnhoff, and G. Dresen. “Laboratory study on fluid-induced fault slip behavior: The role of fluid pressurization rate”. In: *Geophysical Research Letters* 47.6 (2020), e2019GL086627.

[105] L. B. Hunfeld. “Frictional properties of simulated fault gouges from the Groningen gas field and implications for induced seismicity.” PhD thesis. Utrecht University, 2020.

[106] L. Buijze, P. Van den Bogert, B. Wassing, and B. Orlic. “Nucleation and arrest of dynamic rupture induced by reservoir depletion”. In: *Journal of Geophysical Research: Solid Earth* 124.4 (2019), pp. 3620–3645.

[107] T. Barth, R. Herbin, and M. Ohlberger. “Finite volume methods: foundation and analysis”. In: *Encyclopedia of Computational Mechanics Second Edition* (2018), pp. 1–60.

[108] J. C. Simo, J. Oliver, and F. Armero. “An analysis of strong discontinuities induced by strain-softening in rate-independent inelastic solids”. In: *Computational mechanics* 12.5 (1993), pp. 277–296.

[109] H. Hajibeygi and P. Jenny. “Multiscale finite-volume method for parabolic problems arising from compressible multiphase flow in porous media”. In: *Journal of Computational Physics* 228.14 (2009), pp. 5129–5147.

[110] A. L. Stork, J. P. Verdon, and J.-M. Kendall. “The robustness of seismic moment and magnitudes estimated using spectral analysis”. In: *Geophysical Prospecting* 62.4-Vertical Seismic Profiling and Microseismicity Frontiers (2014), pp. 862–878.

[111] B. R. Julian, A. D. Miller, and G. Foulger. “Non-double-couple earthquakes 1. Theory”. In: *Reviews of Geophysics* 36.4 (1998), pp. 525–549.

[112] A. Novikov, S. Shokrollahzadeh Behbahani, D. Voskov, H. Hajibeygi, and J. Jansen. “Benchmarking Analytical and Numerical Simulation of Induced Fault Slip”. In: *ARMA US Rock Mechanics/Geomechanics Symposium*. ARMA. 2023, ARMA–2023.

[113] D. Baú, M. Ferronato, G. Gambolati, and P. Teatini. “Land subsidence spreading factor of the Northern Adriatic gas fields, Italy”. In: *International Journal of Geomechanics* 1.4 (2001), pp. 459–475.

[114] N. Castelletto, H. Hajibeygi, and H. A. Tchelepi. “Multiscale finite-element method for linear elastic geomechanics”. In: *Journal of Computational Physics* 331 (2017), pp. 337–356.

[115] B. H. Russell, K. Hedlin, F. J. Hilterman, and L. R. Lines. “Fluid-property discrimination with AVO: A Biot-Gassmann perspective”. In: *Geophysics* V.1 (2003), pp. 29–39.

[116] D. Bau, G. Gambolati, and P. Teatini. “Residual land subsidence over depleted gas fields in the Northern Adriatic basin”. In: *Environmental & Engineering Geoscience* V.4 (1999), pp. 389–405.

[117] A.-V. Phan, J. Napier, L. Gray, and T. Kaplan. “Symmetric-Galerkin BEM simulation of fracture with frictional contact”. In: *International journal for numerical methods in engineering* 57.6 (2003), pp. 835–851.

[118] E. Keilegavlen, R. Berge, A. Fumagalli, M. Starnoni, I. Stefansson, J. Varela, and I. Berre. “Porepy: An open-source software for simulation of multiphysics processes in fractured porous media”. In: *Computational Geosciences* 25.1 (2021), pp. 243–265.

[119] T. M. Inc. *MATLAB version: 9.14.0.2306882 (R2023a) Update 4*. Natick, Massachusetts, United States, 2023. URL: https://www.mathworks.com.

[120] R. M. Jones. *Deformation theory of plasticity*. Bull Ridge Corporation, 2009.

[121] A. Novikov, D. Voskov, M. Khait, H. Hajibeygi, and J. Jansen. “A scalable collocated finite volume scheme for simulation of induced fault slip”. In: *Journal of Computational Physics* 469 (2022), p. 111598. URL: https://doi.org/10.1016/j.jcp.2022.111598.

[122] D. Voskov, I. Saifullin, M. Wapperom, X. Tian, A. Palha, L. Orozco, and A. Novikov. *open Delft Advanced Research Terra Simulator (open-DARTS)*. Version 0.0.0. June 2023. DOI: 10.5281/zenodo.8046983. URL: https://doi.org/10.5281/zenodo.8046983.

[123] J. H. Dieterich. “Earthquake nucleation on faults with rate-and state-dependent strength”. In: *Tectonophysics* 211.1-4 (1992), pp. 115–134.

[124] M. Kortekaas and B. Jaarsma. “Improved definition of faults in the Groningen field using seismic attributes”. In: *Netherlands Journal of Geosciences* 96.5 (2017), s71–s85.

[125] D. H. P. C. C. (DHPC). *DelftBlue Supercomputer (Phase 1)*. https://www.tudelft.nl/dhpc/ark:/44463/DelftBluePhase1. 2022.

[126] L. F. Athy. “Density, porosity, and compaction of sedimentary rocks”. In: *Aapg Bulletin* 14.1 (1930), pp. 1–24.

[127] H. B. Motra and H. H. Stutz. “Geomechanical rock properties using pressure and temperature dependence of elastic P-and S-wave velocities”. In: *Geotechnical and Geological Engineering* 36 (2018), pp. 3751–3766.

C

[128] *Bodemdaling door aardgaswinning in Groningen, Friesland en het noorden van Drenthe*. Tech. rep. NAM, Dec. 2020.

[129] *Technical Addendum to the Winningsplan Groningen 2016 - Production, Subsidence, Induced Earthquakes and Seismic Hazard and Risk Assessment in the Groningen Field*. Tech. rep. NAM, Mar. 2016.

[130] NAM. *Petrel geological model of the Groningen gas field, the Netherlands*. 2020. URL: https://doi.org/10.24416/UU01-1QH0MW (visited on 10/24/2023).

[131] *Petrel*. Version 2021.1. Houston, TX, USA: Schlumberger.

[132] R. Romijn. "Groningen velocity model 2017—Groningen full elastic velocity model September 2017". In: *Technical Rept.* (2017).

CURRICULUM VITÆ

Sara SHOKROLLAHZADEH BEHBAHANI

15-11-1990 Born in Ahvaz, Iran.

EDUCATION

2009-2013 BSc in Reservoir Engineering
Petroleum University of Technology
Ahvaz, Iran.

2013-2015 MSc in Reservoir Engineering
Amirkabir University of Technology
Tehran, Iran.

2019-2023 PhD. Geomechanics theme, CiTG faculty
Delft University of Technology
Delft, the Netherlands.

Thesis: Embedded Analytical-Numerical Simulation of Fault Reactivation in Heterogeneous Subsurface Formations.

Promotor 1: Dr. H. Hajibeygi
Promotor 2: Dr. D. V. Voskov
Promotor 3: Prof. dr. ir. J. D. Jansen

WORK EXPERIENCE

2015-2019 Reservoir Engineer
National Iranian Oil Company

List of Publications

2. S. Shokrollahzadeh Behbahani, H. Hajibeygi, D. Voskov, and J. D. Jansen. "Smoothed embedded finite-volume method (sEFVM) for modeling contact mechanics in deformable faulted and fractured porous media". In: *Journal of Computational Physics* 459 (2022), p. 111143

1. A. Novikov, S. Shokrollahzadeh Behbahani, D. Voskov, H. Hajibeygi, and J. Jansen. "Benchmarking Analytical and Numerical Simulation of Induced Fault Slip". In: *ARMA US Rock Mechanics/Geomechanics Symposium*. ARMA. 2023, ARMA–2023